Development of Collagen Functionalized Thermally Responsive Poly(N-isopropylacrylamide) Electrospun Nanofibers Scaffold Potentially as a 3D Cell Culture Platform for Rat Amniotic Fluid Stem Cells

By

YONG HSIN NAM ERNEST

A dissertation submitted in partial fulfilment of the requirements for the degree of Doctor of Philosophy in Mechanical Engineering

Faculty of Science and Engineering
The University of Nottingham Malaysia

ABSTRACT

2D surfaces such as tissue culture polystyrene dish used in conventional cell culture have limited surface area for cell growth. During harvest, mechanical scraping or trypsin are used to remove confluent cells from their growing surface, which can be harmful to cells and reduce cell yield. Therefore, there is a need for an improved cell growth surface with increased surface area and an alternative non-invasive cell harvesting mechanism. To this end, a potential three-dimensional (3D) cell culture platform was developed with nanofibers of poly(N-isopropylacrylamide) (PNIPAm) as the main structural framework, fabricated via the electrospinning technique. Collagen type I extracted from fish scales of Tilapia fish was used to functionalize PNIPAm nanofibers scaffold via dip-coating to improve cell-scaffold interaction. The developed electrospun PNIPAm nanofibers scaffold exhibits a morphology that highly mimics the native extracellular matrix (ECM) in terms of fiber diameter, measuring 436.35 ± 187.04 nm. Pore size and porosity were computed as 1.24 ± 1.27 nm and 63.6 %, respectively. Collagen functionalized PNIPAm nanofibers scaffolds show significant improvement in cell viability of rat amniotic fluid stem cells (R3-AFSC) with increasing collagen content, with 50, 70 and 180 % cell viability on neat electrospun PNIPAm, PNIPAm dip-coated in 0.1 and 0.5 % (w/w) collagen solution, respectively. On the other hand, increased collagen content reduces the capability of PNIPAm nanofibers scaffold to spontaneously release R3-AFSC upon cooling from cell culture conditions (37 °C and 5 % CO_2) to 25 °C (room temperature), with 51, 48 and 43 % of R3-AFSC released from neat electrospun PNIPAm, PNIPAm dip-coated in 0.1 and 0.5 % (w/w) collagen solution, respectively.

DEDICATION

This thesis is dedicated to my late grandmother,

Mdm. Chai Siew Lan.

ACKNOWLEDGMENTS

My deepest gratitude goes to my parents for their unconditional love, support, and faith. We may be apart, but your presence has never left.

Last but not least, I would like to extend my appreciation to a person I met along the way, who has purposefully supported me through times of crises and made moments of celebration worthwhile.

DECLARATION

I declare that this thesis was composed solely by myself and has not been submitted, in whole or in part, in any previous application for a degree.

PUBLICATION LIST

Journal Publications

1. **Yong E.,** Tshai K.Y., Lim S.S. (2021) Aqueous stability of cross-linked thermal responsive tissue engineering scaffold produced by electrospinning technique. Key Engineering Materials, 897 (39-44).

2. **Yong E.,** Tshai K.Y., Lim S.S., Kong I., (2020) Poly(N-isopropylacrylamide) microgel synthesised by emulsion polymerization. Diffusion and Defect Data Pt. B: Solid State Phenomena, 307 (345-350).

3. Tshai K.Y., Chin M.H., Lim S.S., Loh S.H.S., **Yong E.,** Nuge T., (2020) Fish scale collagen functionalized thermo-responsive nanofibers. Key Engineering Materials, 846 (189-194).

Conference Proceedings

1. **Yong E.,** Lim S.S., Tshai K.Y., (2019) The effect of agitation rate on the free radical polymerization of N-isopropylacrylamide. 4th International Conference on the Science and Engineering of Materials. **Kuala Lumpur.**

2. **Yong E.,** Lim S.S., Tshai K.Y., (2022) Investigation into the morphology and aqueous stability of electrospun PNIPAm nanofibrous scaffold cross-linked with OPEPOSS. Advanced Materials Characterization Techniques 2022. **India.**

TABLE OF CONTENTS

LIST OF FIGURES

LIST OF TABLES

ABBREVIATIONS

A100	PNIPAm synthesised at 100 rpm
A200	PNIPAm synthesised at 200 rpm
A50	PNIPAm synthesised at 50 rpm
AA	Acetic acid
AIBN	Azobisisobutyronitrile
Am	Acrylamide
APS	Ammonium persulfate
ATRP	Atom transfer radical polymerization
BDDGE	1,4-butanediol diglycidyl ether
BIS	N, N'-methylenebisacrylamide
CA	Citric acid
CMC	Critical micelle concentration
CS	Chondroitin sulfate
CTAB	Centrimonium bromide
DAAM	Diacetone acrylamide
ddH$_2$O	Deionized water
DHT	Dehydrothermal
DMF	N, N-dimethylformamide
DMSO	Dimethyl sulfoxide
ECM	Extracellular matrix
EDC	1-ethyl-3-(3-dimethylaminopropyl)carbodiimide hydrochloride

EDTA	Ethylenediaminetetraacetic acid
EMI	2-ethyl-4-methylimidazole
ESM	Embryonic stem cell working medium
EtOH	Ethanol
FA	Formic acid
FACIT	Fibril-associated collagen with interrupted triple helix
FBS	Fetal bovine serum
FP	Fiber forming structural protein
GMEM	Glasgow's minimum essential media
GNR	Gold nanorod
GTA	Glutaraldehyde
HBSS	Hank's balance salt solution
HFIP	Hexafluoroisopropanol
HMDI	Hexamethylene diisocyanate
Ir 184	Irgacure 184
KPS	Potassium persulfate
LCST	Lower critical solution temperature
LIF3010	Leukemia inhibitory factor (rat)
MA	Methacrylic acid
MeOH	Methanol
NCPAE	2-chloro-n-(2-hydroxyethyl propenamide)
NHS	N-hydroxysuccinimide

NIPAm	N-isopropylacrylamide
NIR	Near infrared
NMA	N-methylol acrylamide
OPEPOSS	Octaglycidyl polyhedral oligomeric silsesquioxane
PBS	Phosphate buffered saline
PCL	Poly-ε-caprolactone
PEO	Polyethylene oxide
PHBA	Poly(3-hydroxybutyric acid)
PLA	Polylactic acid
PLCL	Poly(L-lactide-co-caprolactone)
PLGA	Poly(D,L-lactide-co-glycolide)
PLLA	Poly(l-lactic acid)
PMMA	Poly(methyl methacrylate)
PNIPAm	Poly(N-isopropylacrylamide)
POC	Poly(1,8-octanediol citrate)
PPS	Potassium peroxodisulfate
PPy	polypyrrole
PVP	polyvinylpyrrolidone
RAFT	Reverse addition-fragmentation chain transfer
RGD	Arg-Gly-Asp tripeptide
SDBS	Sodium dodecyl benzenesulfonate
SDS	Sodium dodecyl sulfate

SDS-PAGE	Sodium dodecyl sulfate-polyacrylamide gel electrophoresis
SHP	Sodium hypophosphite
TCPS	Tissue culture polystyrene dish
TEMED	Tetramethylethylenediamine
TES	Tissue engineering scaffold
TFE	2, 2, 2-trifluoroethanol
TFS	Tilapia fish scale
THF	Tetrahydrofuran
tris-HCl	Tris-hydrochloride

Chapter 1

INTRODUCTION

1.1 Background

In conventional cell culture, the two dimensional (2D) planar culture utilizing tissue culture polystyrene dish (TCPS) provides limited surface area for cell attachment, proliferation, and differentiation. In addition, common techniques used for cell harvesting by mechanical scraping or trypsin cleaving the cell membrane protein to separate confluent cells from their growing surface can be harmful to cells and reduce cell yield [1], [2]. Naturally occurring polymer such as collagen, makes up the major component of the ECM [3]. Providing a collagen rich environment to mimic the ECM in a cell culturing medium promotes cell adhesion via binding of specific amino acid sequences. However, on its own, collagen lacks the mechanical properties of native tissues at physiological mass fractions to support cell growth. To resolve these matters, collagen could be incorporated with 3D PNIPAm nanofibrous scaffolds which exhibit ultrahigh surface area to volume ratio for cell attachment and growth. The development of smart polymeric materials that are sensitive to external stimuli e.g., temperature, pH or light, offers great prospect to the fields of tissue engineering, biomedicine and drug delivery. The well-established thermo-responsive polymer, PNIPAm, undergoes a

sharp and reversible phase transition between hydrophilicity and hydrophobicity across its lower critical solution temperature (LCST) at approximately 32 °C, which holds great potential for enhancing attachment of anchorage-dependent cells in its hydrophobic phase (above 32 °C) [1], [4], [5]. On the other hand, the use of PNIPAm could facilitate a non-invasive cell harvesting mechanism through spontaneous release of cells in its hydrophilic phase (below 32 °C) [1], [6]. Commercially sourced collagens, particularly those derived from cows and pigs, pose religion concerns on their use. To add to that, mammalian collagen poses the risk of disease transmission such as bovine spongiform encephalopathy (BSE). The use of marine collagen such as those derived from fish wastes could alleviate these issues while wastes are converted into value added products. In the present research, PNIPAm was synthesized via radical polymerization. Nanofibers of PNIPAm was obtained from the electrospinning technique, yielding non-woven membranes of nanofibrous PNIPAm scaffolds. At the same time, collagen (type I) was extracted from tilapia fish scales. The purified collagen was incorporated with PNIPAm nanofibrous scaffolds via dip-coating, as a functionalization method to improve the bioactivity of PNIPAm scaffolds. Finally, the cell viability and spontaneous cell release mechanism of PNIPAm nanofibrous scaffolds functionalized with collagen was evaluated using stem cells isolated from rats.

2

1.2 Problem Statement

Commercially available PNIPAm mostly come at a high cost and options for different molecular weights is limited, which can limit its use. Synthesis methods of PNIPAm based polymers via radical polymerization have been widely reported, which could serve as an alternative method to obtain PNIPAm. However, these available synthesis methodologies largely yield PNIPAm hydrogels, which are essentially cross-linked PNIPAm achieved in the presence of the bifunctional cross-linker N, N'-methylenebisacrylamide (BIS) during the polymerization process[7]–[9]. Cross-linked PNIPAm exhibits relatively poor electrospinnability and the underlying mechanism behind this phenomenon is not well understood. To this end, BIS could be excluded from the synthesis of PNIPAm to limit cross-linking, but how effective is the radical polymerization process in producing cross-linker free PNIPAm? In other words, the effectiveness of radical polymerization in producing cross-linker free PNIPAm is not well understood, particularly in terms of the preservation of its characteristic thermal responsiveness, and its batch-to-batch reproducibility. Furthermore, commercially available, uncross-linked PNIPAm were commonly reported in the electrospinning of PNIPAm[10]–[12], where the comparison between the electrospinnability of cross-linked and uncross-linked PNIPAm has not been explored in terms of its final fiber morphology. In addition,

collagen has also been used to functionalize various polymers such as poly(D, L-lactide-co-glycolide) (PLGA)[13], poly-ε-caprolactone (PCL)[14] and poly(l-lactic acid) (PLLA)[15] to improve their biocompatibility. However, collagen has yet to be functionalized on electrospun PNIPAm nanofibers. Finally, cell culture on collagen functionalized PNIPAm nanofibrous scaffolds has not yet been reported in literature, which leaves out a potentially viable cell culture platform capable of cultivating improved yield of cells, furnished with a spontaneous cell release mechanism.

1.3 Research Significance

In this work, the synthesis of PNIPAm via radical polymerization in the absence of cross-linkers is explored. This helps in developing further understanding towards specific polymerization parameters such as agitation rate and its effect on the resulting polymer, while informs an alternative method to reproducibly obtain PNIPAm with preserved thermal responsiveness, which could expand its use in more diversified applications. Additionally, the compared electrospinnability between cross-linked and uncross-linked PNIPAm (with similar viscosities) helps in describing the underlying mechanism of the relatively poor electrospinnability of cross-linked PNIPAm. The proposed mechanism is crucial to ensure successful fabrication of polymer nanofibers via electrospinning, which is not only limited to PNIPAm but also for the electrospinning of other

polymers. Finally, the development of collagen functionalized PNIPAm nanofibrous scaffold was explored as a potentially more superior method from culturing cells on conventional 2D cell culture platforms, which could significantly improve cell yield, reduce culture space and cost.

1.4 Research Objectives

The research objectives to this research are as follow:

(i)   To synthesize and characterize PNIPAm.

(ii)   To extract collagen from fish scales using the dilute acid extraction method.

(iii)   To prepare and evaluate PNIPAm and collagen electrospun nanofibers.

(iv)   To investigate the cell viability and spontaneous cell release of electrospun nanofibers.

1.5 Thesis Overview

Chapter one describes the background, significance, specific challenges and novelty of this research work. Chapter two provides the literature review on the radical polymerization mechanism, synthesis of PNIPAm based polymers, background on collagen and its processing via electrospinning. Chapter three presents the methodologies used in this research. Chapter four gives a thorough

discussion on the findings within this research work, highlighting the properties of synthesized PNIPAm, optimisation of synthesized PNIPAm electrospinning in obtaining PNIPAm nanofibers, extraction and characterization of fish scale derived collagen, incorporation of fish scale collagen to PNIPAm nanofibrous scaffold and cell viability of R3-AFSC on collagen functionalized PNIPAm nanofibers scaffold. Chapter five consists of the conclusion and the recommendation for future work.

Chapter 2

LITERATURE REVIEW

2.1 Requirements of Tissue Engineering Scaffolds

The interdisciplinary field of tissue engineering is defined by the development of biological substitutes to restore, maintain or improve tissue functions[16]. Consequent deterioration and damage of tissues caused by diseases and injuries compel the need for surgical treatment, conventionally in the form of tissue autoplasty or transplant. These methods however have significant drawbacks related to perceptible afflictions such as pain and discomfort, among other general downside of being costly, anatomical constraints, probable immune response due to tissue rejection, donor-patient disease introduction, infection, and hematoma. Instead of replacing, tissue engineering aims to regenerate tissues both in vitro and in vivo, largely by exploiting 3D porous constructs called scaffolds[17]. Figure 2.1 shows the concept of tissue engineering.
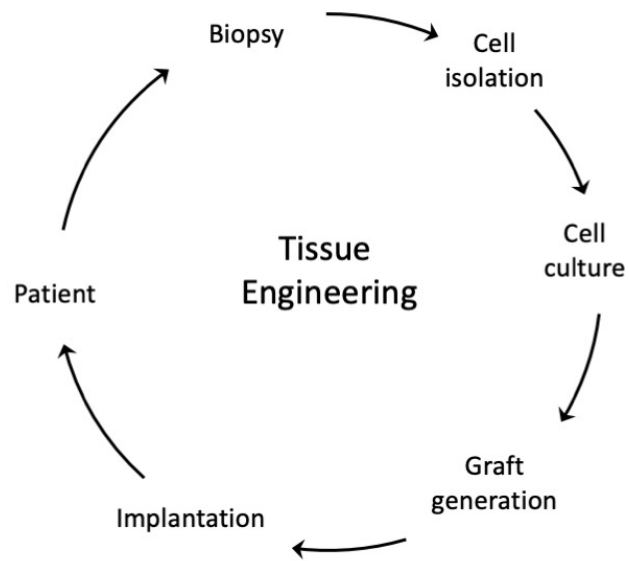
Figure 2.1: Tissue engineering concept.

Three main factors are generally observed in tissue engineering, customarily dubbed the tissue engineering triads; scaffold, cells and regulatory signals. These factors conceptualize the motivation in producing a viable tissue engineering scaffold (TES) to provide anchorage to subjected cells that form particular tissues, while facilitated to express the desired tissue phenotype by regulatory signals such as growth factors, among other biological cues[18], [19]. Irrespective of tissue type, several key criteria should be considered in designing viable TESs:

A) Biocompatibility and biodegradability

Biocompatible TESs should support cell activity such as adhesion, proliferation, infiltration from its surface to its core and producing new ECM, while must not trigger significant immune response that

could potentially result in serious inflammation and host body rejection[17], [20]. Mostly, TESs are meant as interim support for tissue regeneration until cells can produce their own ECM. This necessitates the need for TESs to be biodegradable and capable of controlled degradation which involves severance of chemical bonds through hydrolysis or enzyme action[20], [21]. Ideally, degradation rate should be congruent with rate of cell growth, while by-products of biodegradation should be biocompatible and non-immunogenic to not cause negative side effects[17]. However, immunogenicity, long-term safety of by-products, infection risk, and transmission of disease remain as great challenges in tissue engineering[21]. As for long term support, biologically stable constructs are used and are non-biodegradable through their lifetime[20].

B) Porosity, pore interconnectivity and mean pore size

Desired TESs should possess high porosity with interconnected pores, to provide high effective surface area for cell penetration, ingrowth, distribution and facilitate nutrient dispersal to cells and ECM produced by cells within the construct[17][20]. Additionally, interconnected pores provide vascularization for removal of waste products from TESs such as cell metabolite and by products of its own degradation. Core degradation of TESs arising from lack of waste removal is attributed to the lack of vascularization[22][23]. Cells adhere to TESs by interacting with ligands present on the material surface such as

the tripeptide, arginylglycylaspartic acid (RGD) motif, native on TESs made of ECM materials. The mean pore size directly affects the specific surface area within for cells to interact with, in turn regulating the density of these ligands. Ideally these ligands should be distributed at minimum density sufficient for effective binding of critical number of cells. Accordingly, the mean pore size should not be too large to accommodate maximum number of cells, while not too small that would inhibit migration of cells, nutrients and wastes[17][24]. Hence, there exist a suitable range of pore sizes in TESs for specific cell lines[25][26]. For instance, pore sizes between 100 to 400 µm have been reported suitable for bone ingrowth in bone regeneration[27]. Additionally, adjusting pore size, porosity or both have reportedly improved cell proliferation, where enhanced cell proliferation was observed with human foreskin fibroblast on TES made of silk fibroin with pore sizes ranging from 100 to 150 µm and 200 to 250 µm with porosities of 91 % and 86 %, respectively[28], [29]. Preferential chondrocyte proliferation and preserved phenotype was demonstrated with pore sizes from 250 to 500 µm. In contrast, reduction in pore sizes to 50 to 200 µm prompted dedifferentiation of chondrocytes[30]. Furthermore, study on preosteoblasts on collagen-glycosaminoglycan scaffold claimed that larger pores facilitating cell infiltration predominates the benefits of increased surface area for cell adhesion imparted by smaller pores[31].

C) Mechanical properties

To facilitate normal cell function and ease of handling, mechanical properties of TESs are of great importance. Highly porous TES promotes cell infiltration and vascularization necessary to facilitate circulation of nutrients and metabolites, albeit in the expanse of diminished mechanical properties as a consequence of increased voids within the bulk. Insufficient mechanical integrity would defeat the purpose of scaffolding to allow new tissue regeneration, while exaggerated mechanical properties would cost the reduction in porosity[16], [17]. Therefore, tuning mechanical properties to mimic the native ECM can greatly benefit the viability of TES. For instance in bone regeneration, it is necessary to design scaffolds with adequate structural integrity to withstand physiological loadings, while decrease in bone density occurs with excessive mechanical integrity due to stress shielding[31][32].

D) Mass production and cost effectiveness

In provision for TESs toward regular clinical and commercial use, it is necessary to scale up lab production into well controlled, reproducible, and cost-effective batch fabrication. The ability to mass produce complex TESs is essential to meet the need for continuous supply and ideally hold high availability[16], [17].

2.2 Thermo-responsive PNIPAm Synthesis

Radical polymerization is a chain growth polymerization that remains as the most widely used polymerization technique of vinyl monomers (monomers containing C=C bonds), such as N-isopropylacrylamide (NIPAm). Several advantages describing its versatility include the inexpensive operation, simplicity and chemical inactivity with the greenest solvent, water, which is often used as the reaction medium. The presence of ambient oxygen within the reaction medium generally causes inhibition in polymerization but can be easily purged out with an inert gas or by allowing a small period of induction time sacrificing a minor portion of the initiator[33],[34].

2.2.1 Mechanism

The radical polymerization mechanism follows three main sequences, namely initiation, propagation, and termination. In the initiation step, initiator molecules decompose to yield primary radicals under influence of various stimulation (e.g., thermal, ultraviolet (UV), redox) specific to the initiator type, a single initiator molecule (e.g., potassium persulfate (KPS)) decomposes to produce two primary radicals (Figure 2.2). Primary radicals produced proceed to disrupt the C=C bond of the unsaturated monomer (e.g., NIPAm) forming monomeric radicals, summing up the initiation step (Figure 2.3).

Primary radicals attack C=C bonds because there exist a loosely held electron pair in its pi bond.
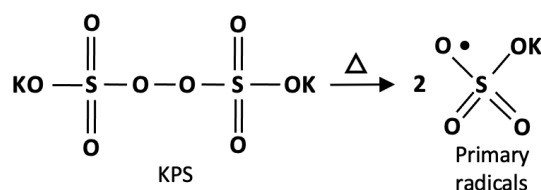
Figure 2.2: Decomposition of a KPS (initiator) molecule forming two primary radicals.
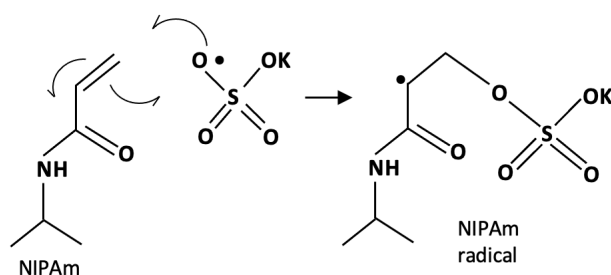
Figure 2.3: NIPAm monomer initiated by a persulfate radical generated from decomposition of KPS.

During the subsequent chain propagation step, monomeric radicals go on to initiate adjacent unsaturated monomers resulting in dimeric radicals and so on forming long chain oligomeric radicals (Figure 2.4). During polymerization, C=C bonds are generally converted into C-C bonds. Given that the bond strength of the C=C bond is higher than the C-C bond, a negative enthalpy change takes place which makes polymerization an exothermic reaction.
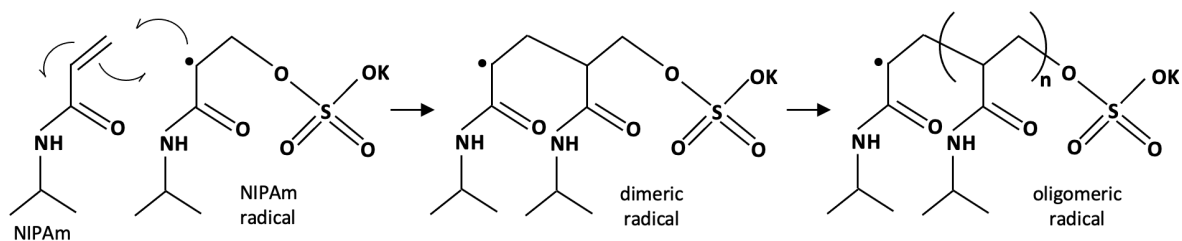
Figure 2.4: Chain propagation of a NIPAm radical forming a dimeric and subsequent oligomeric radicals.

As chains continue to elongate, there are several inevitable fates where these radicals get inactivated, therefore discontinuing propagation. This is the termination step and provided that the reaction mixture is free from impurities such as oxygen, possible termination routes include termination by combination, disproportionation, and chain transfer. Chain termination by combination may result from two scenarios as illustrated in Figure 2.5 where, (A) two active (radical) polymer chains merge into a single chain or (B) an active polymer chain merges with a primary radical. The length of the former chain would essentially be twice of the latter, therefore if a high molecular weight polymer is desired, the initiator concentration should be kept reasonably low to promote more termination via combination of two active polymer chains while avoiding early termination by combination of active growing chains with primary radicals. In termination by disproportionation, an "end of chain" hydrogen from an arbitrary adjacent active polymer chain is transferred resulting in a saturated and an unsaturated polymer

molecule depicted in Figure 2.6. The termination steps described thus far involve the inactivation of two active radicals.
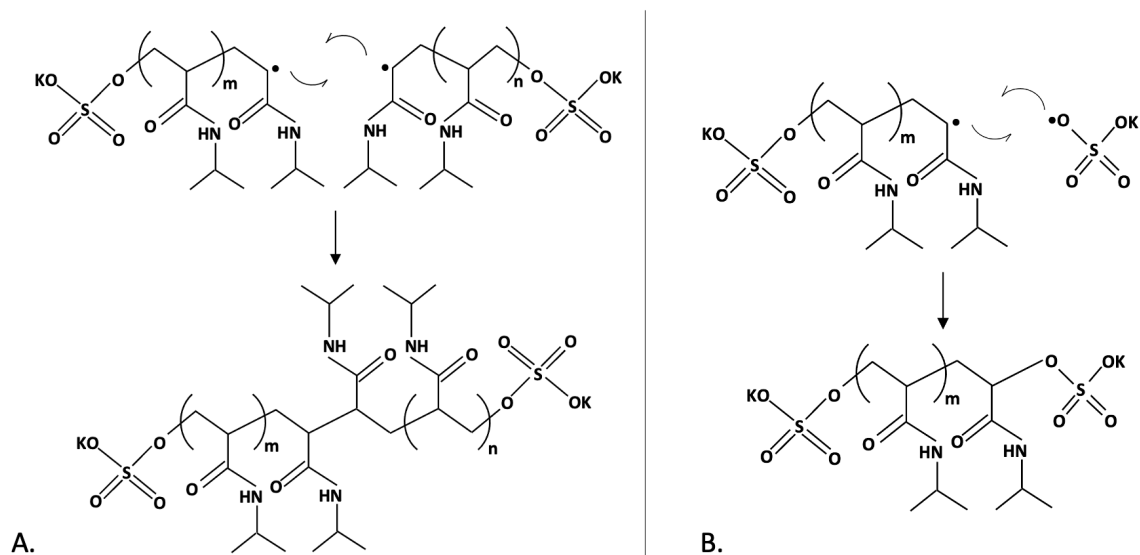
Figure 2.5: (A) Termination by combination of two active (radical) PNIPAm chains and (B) termination by combination of an active PNIPAm chain and a primary radical.
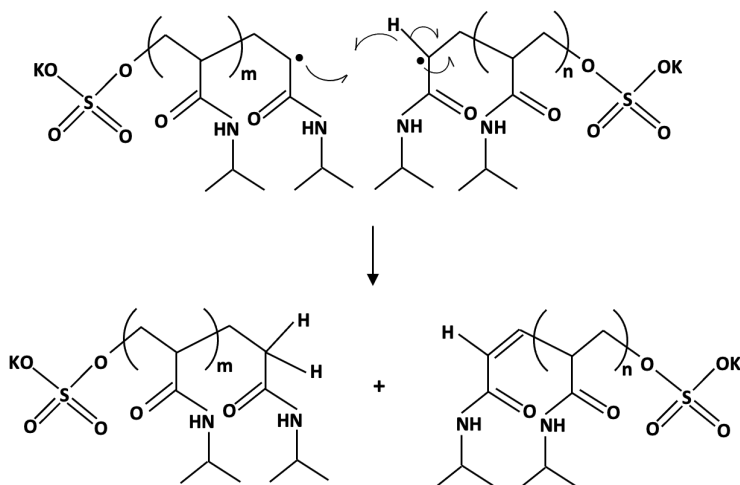
Figure 2.6: Termination of two active PNIPAm chains by disproportionation.

However, termination via chain transfer follows a rather different mechanism where a single radical is terminated instead, while forming a new radical. The switch in chain activity occurs by hydrogen transfer similar to termination by disproportionation, between a propagating polymer chain and four different species, namely the solvent, monomer, initiator and polymer (Figure 2.7). Chain transfer to any species is dependent on the conditions during polymerization, for instance chain transfer to solvent takes place when the chosen solvent is not inert to the polymerization. Significant chain transfer to monomer occurs mainly in cationic addition polymerization and ring opening polymerization while chain transfer to polymer happens when there is a large amount of polymer present (e.g.,. at the end of polymerization). Chain transfers from solvent and monomer form solvent and monomer radicals that are unable to further propagate while chain transfer from initiator leads to formation of a new radical that is able to further initiate. When chain transfer occurs from a polymer chain, the newly formed polymer radical is able to form a branched chain[33], [34].
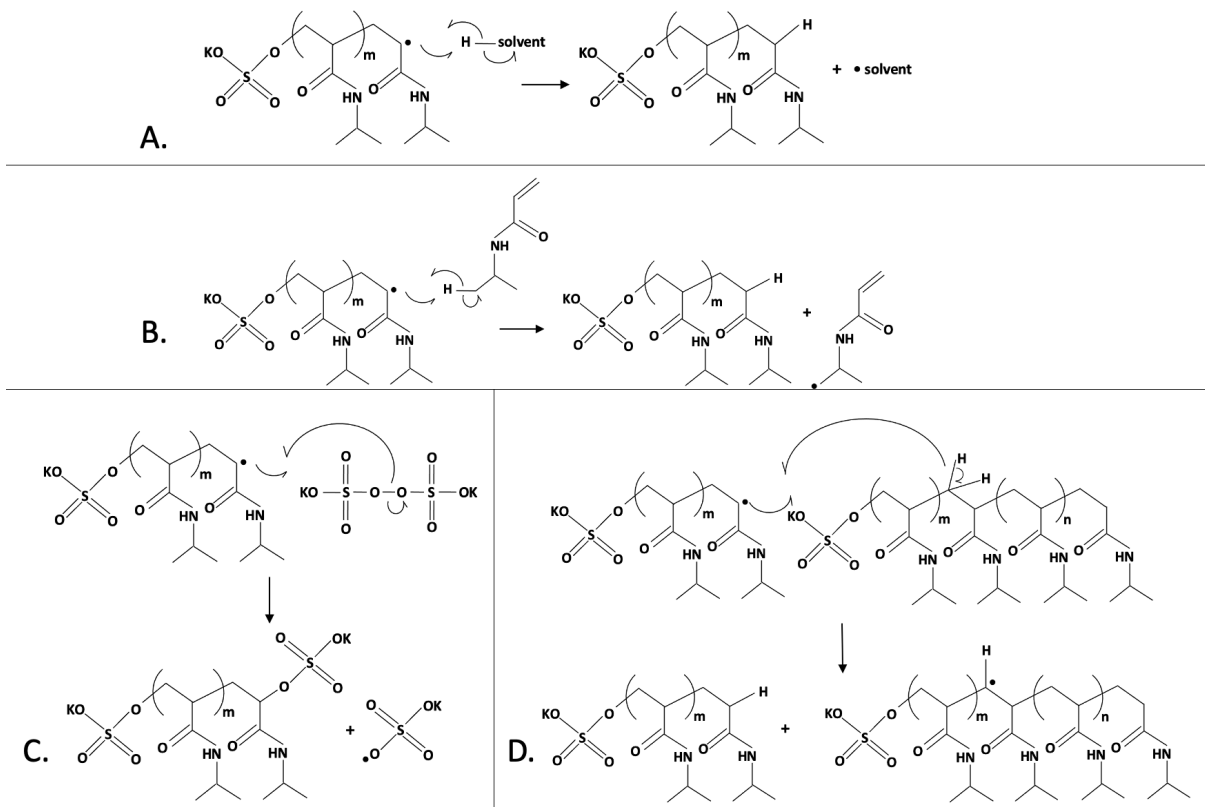
Figure 2.7: Termination by chain transfer from PNIPAm radical to (A) solvent, (B) NIPAm, (C) KPS (initiator) and (D) PNIPAm.

2.2.2 Emulsion Polymerization

In emulsion polymerization, the volume of the reaction mixture is compartmentalized into a large number of very small volume particles suspended in a continuous phase[35]. The size of polymer particles generated by emulsion polymerization is between 10 and 1000 nm and these particles remain dispersed in a continuous aqueous phase[36]. Advantages of emulsion include the capability to obtain high molecular weight polymer with high reaction rates, high monomer-polymer conversion and excellent temperature control.

Main components of an emulsion polymerization system comprise of the aqueous continuous phase (e.g., water), monomer (water soluble or insoluble), surfactant and water soluble initiator[37].

2.2.2.1 Particle Nucleation

The formation of particles in emulsion polymerization is divided into two main mechanisms, namely the heterogenous particle nucleation or micellar particle nucleation and the homogenous particle nucleation, summarized in Figure 2.8.
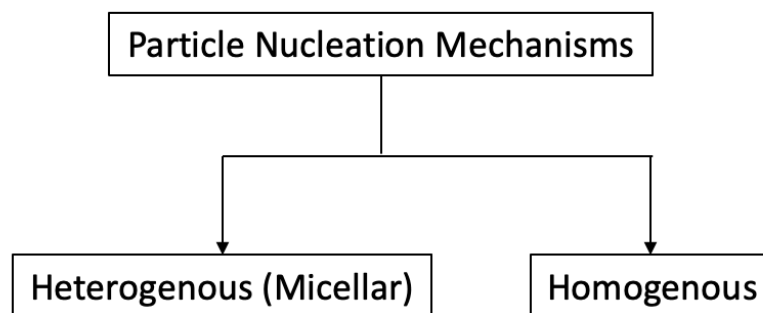
Figure 2.8: Particle nucleation mechanisms.

Micellar particle nucleation (Figure 2.9) occurs when radicals from the aqueous phase enter the monomer swollen micelles (reaction sites). As for homogenous particle nucleation (Figure 2.10), solution polymerized oligomeric radicals become insoluble and self-associate (precipitate), followed by absorption of surfactants to achieve stability. The mode of particle nucleation is dependent on the surfactant concentration and the water solubility of monomer. Well

above the critical micelle concentration (CMC), micellar nucleation predominates to more than 99% in terms of particle formation. Close to the CMC, micellar nucleation still predominates while homogenous nucleation also takes place. The extent of homogenous nucleation in this case is higher for monomers of higher water solubility. As micelles are absent below the CMC, only homogenous nucleation occur. The aforementioned are summarized in Table 2.1.

Table 2.1: Particle nucleation mechanism based on surfactant concentration and water solubility of monomer.

Nucleation mechanism	Surfactant concentration	Water solubility of monomer
Micellar	Well above CMC	Soluble/insoluble
Micellar>homogenous	At CMC	Insoluble
Micellar<homogenous	At CMC	Soluble
Homogenous	Below CMC	Soluble/insoluble

Also below the CMC, is it suggested that the formation of precursor particles is from the coagulation with other particles. The driving force to coagulative nucleation is the relative instability of precursor particles compared to larger particles where there is insufficient amount of surfactant to stabilise a larger amount of smaller particles. As the particles are sufficiently large, the available surfactant can

effectively stabilise the particles where coagulative nucleation ceases[37].
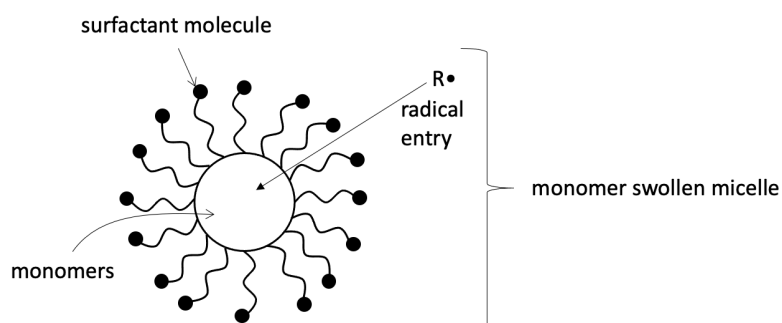
Figure 2.9: Micellar particle nucleation mechanism.
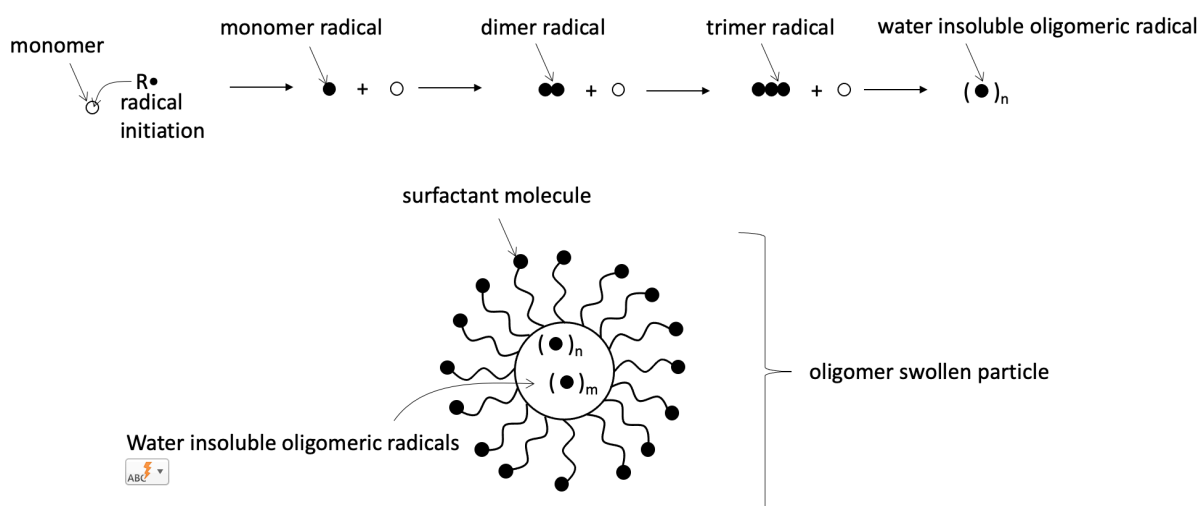
Figure 2.10: Homogenous particle nucleation mechanism.

2.2.3 Recent synthesis methods of PNIPAm

Owing to its LCST being close to human physiological temperature at approximately 32 °C, PNIPAm has found wide interest in potential applications such as drug delivery and tissue engineering. PNIPAm and PNIPAm based polymers are typically synthesized by radical polymerization which takes advantage of the unsaturated vinyl group

(C=C) of its monomers. Among radical polymerizations, precipitation polymerization is one of the most widely employed[38]. Other radical polymerization methods such as emulsion, solution, reverse addition-fragmentation chain transfer (RAFT) and atom transfer radical polymerization (ATRP) have also been reported. Some notable recent reported PNIPAm and PNIPAm based polymers are highlighted and the corresponding ingredients are summarised in Table 2.2. Regardless of which method, all PNIPAm prepared by radical polymerization uses its monomer NIPAm as starting material. In polymerization of NIPAm, initiation is commonly achieved by thermal decomposition of initiators such as ammonium persulfate (APS) [7], [39], KPS [9], [40], potassium peroxodisulfate (PPS) [41], and azobisisobutyronitrile (AIBN) [8], [42] into free radicals. Use of UV decomposed initiator such as Irgacure 184 (Ir 184) has also been reported[43]. Production of PNIPAm microgels (i.e., cross-linked PNIPAm) are mostly (if not all) achieved by employing the bifunctional cross-linker BIS. In emulsion polymerization, sodium dodecyl sulfate (SDS) [39], [44] is commonly used as surfactant, while use of sodium dodecyl benzenesulfonate (SDBS) [8] and centrimonium bromide (CTAB) [45] has also been reported. Polyvinylpyrrolidone (PVP) has been reported as stabilizing polymer when PNIPAm was synthesized by dispersion polymerization[45]. The continuous phase is commonly water. However, in more sophisticated polymerization methods such as RAFT, solvents such as tert-butanol

(t-BuOH)[9] and tetrahydrofuran (THF)[46] has been used to dissolve non-liquid monomers, while in ATRP, use of isopropanol (iso-PrOH)[47] has also been reported. Both RAFT and ATRP are known to provide control over molecular weight and polydispersity. A common catalyst if polymerization at a low temperature is desired is tetramethylethylenediamine (TEMED) [45], [48].

Table 2.2: Synthesis methods of PNIPAm via radical polymerization.

Polymerization type	Initiator	Co-monomer	Product	Ref.
Precipitation	APS	acrylic acid	microgel	[7]
Emulsion	AIBN	-	nanogel film	[8]
Soap-free emulsion	KPS		microgel	[9]
Emulsion	APS	MA	microgel	[39]
Au-seeded precipitation	PPS	-	microgel film	[41]
UV-initiated radical	Ir 184	-	hydrogel	[43]
Precipitation	KPS	DAAM	microgel	[40]
ZnO-seeded precipitation	KPS	-	microgel	[45]
ZnO-seeded dispersion	KPS	-	microgel	[45]
ZnO-seeded emulsion	KPS	-	microgel	[45]
RAFT	AIBN	-	microgel	[42]

Solution	APS	NMA/Am	-	[49]
ATRP	NCPAE	-	styrene co-polymer	[47]
Emulsion	APS	-	microgel	[44]
Solution	KPS	-	nanogel	[48]
Precipitation	KPS	-	nanogel	[48]
RAFT	AIBN	-	Photo-dimerized chains	[46]
Radical	AIBN	-	nanoparticle	[50]

[a]Abbreviation: methacrylic acid (MA), diacetone acrylamide (DAAM), N-methylol acrylamide (NMA), acrylamide (Am), 2-chloro-n-(2-hydroxyethyl propenamide) (NCPAE), gold (Au), zinc oxide (ZnO)

2.3 ECM and Collagen

The ECM is a major, non-cellular constituent which connects cells within connective tissues. The two main classes of macromolecules that constitute the ECM are the fiber forming structural proteins (FP) and proteoglycans. FPs form complex 3D framework to provide structural integrity to tissues and these rigid proteins are mainly collagen and elastin. Surrounding these rigid proteins are proteoglycans and glycoproteins existing in hydrophobic and hydrated gel form providing an osmotically active interstitial space

which fortifies the structural network and provide connection between cells, among other functions[51].

2.3.1 The structural ECM

Collagen, the most abundant protein and predominant form of FP in the ECM provides tensile strength, form and regulation over cell adhesion and migration[52]. The rod-shaped collagen molecule is built upon the assembly of three polypeptide α-chains, each coiled in a left-handed helix where these α-chains entwine together on a single longitudinal axis forming the characteristic left-handed, triple helical structure[53]. These α-chains are characterized by the distinctive repeat units of Gly-X-Y where Gly stands for glycine while X and Y could be any amino acid, often proline or hydroxyproline residues, respectively[54]. The presence of glycine in every third position in the polypeptide chain ensures the proper folding of the collagen molecule in its native triple helical structure through hydrogen bonding between amine (-NH) and carbonyl (C=O) groups between the α-chains[55]. Furthermore, high imino acid content in the X and Y positions of the α-chain and hydroxylation of proline into hydroxyproline were known to improve the stability of the triple helix[56]. A single collagen molecule is about 300 nm in length and 1.5 – 2 nm in diameter[57]. Figure 2.11 shows the cross-linking between three typical α-chains.
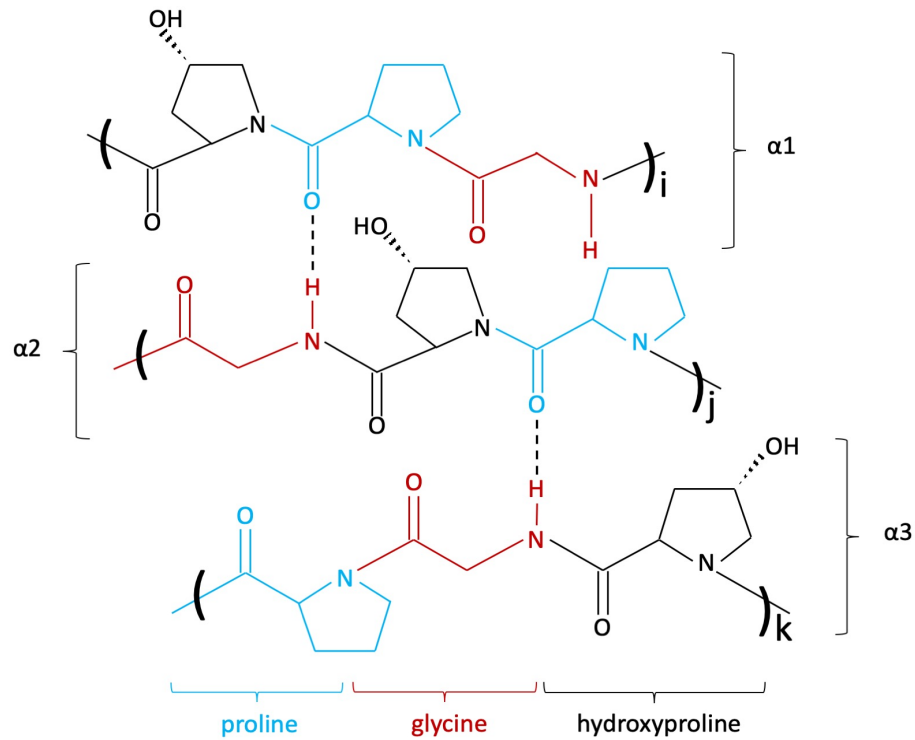
Figure 2.11: Cross-linking of three typical polypeptide α-chains through hydrogen bonding (represented by dashed lines). Cross-links between α1 and α3 chains not drawn, while i, j and k represent number of repeat units corresponding to Y-X-Gly, Gly-Y-X and X-Gly-Y, respectively.

Collagen is further differentiated based on their supramolecular assembly and specific functions, existing as homotrimers and heterotrimers with one or two distinct α-chains[55]. Till date, 29 types of collagen comprised of 46 variation of α-chains have been identified[58], [59], [60]. The collagen family can be distinguished into 8 sub-families, summarized in Table 2.3, reproduced from [53].

Table 2.3: Collagen sub-family and corresponding types.

Collagen sub-family	Collagen type
Fibrillar/fibril forming	I, II, III, V, XI, XXIV and XXVII
*FACITs and related	IX, XII, XIV, XVI, XIX, XX, XXI, XXII and XXVI
Hexagonal network forming	VIII and X
Type IV family	IV
Beaded filaments forming	VI
Anchoring fibril forming	VII
With transmembrane domains	XIII, XVII, XXIII and XXV
Type XV and XVIII	XV and XVIII

fibril-associated collagen with interrupted triple helices (FACITs).

Fibrillar collagen constitute most of the ECM protein in vertebrates [61]. These collagen types were jointly classified due to their fibril forming nature with characteristic striated axial periodicity along these fibrils of approximately 67 nm, often referred to as 67 nm banding or D-banding pattern [56]. Collagen exists in most parts of the body, but different types predominate in different tissues. Table 2.4 summarizes some fibrillar collagens and their corresponding native ECM, reproduced with modifications from [62].

Table 2.4: Types of fibrillar collagens and their native ECM.

Collagen type	Native in
I	Skin, bone, tendon, cornea
II	Cartilage, vitreous, intervertebral disc
III	Blood vessels, intestine
V	Skin, bone, embryonic tissue, cornea
XI	Cartilage, intervertebral disc

Among fibrillar collagens, the heterotrimeric type I collagen is the predominant and most abundant collagen while it is also the most abundant protein in the mammalian kingdom[56]. They form fibrillar constructs with diameter of 50 - 200 nm. Short and non-helical segments at either end of its molecule are responsible for fibril formation by establishing aldimine cross-links between two lysine or hydroxylysine at the C-terminus of one molecule to the N-terminus of its adjacent molecule[63]. These collagen fibrils assemble together to form collagen nanofibers in the range of 50 to 500 nm in the ECM[64]. Figure 2.12 shows the sequence of collagen fiber formation.
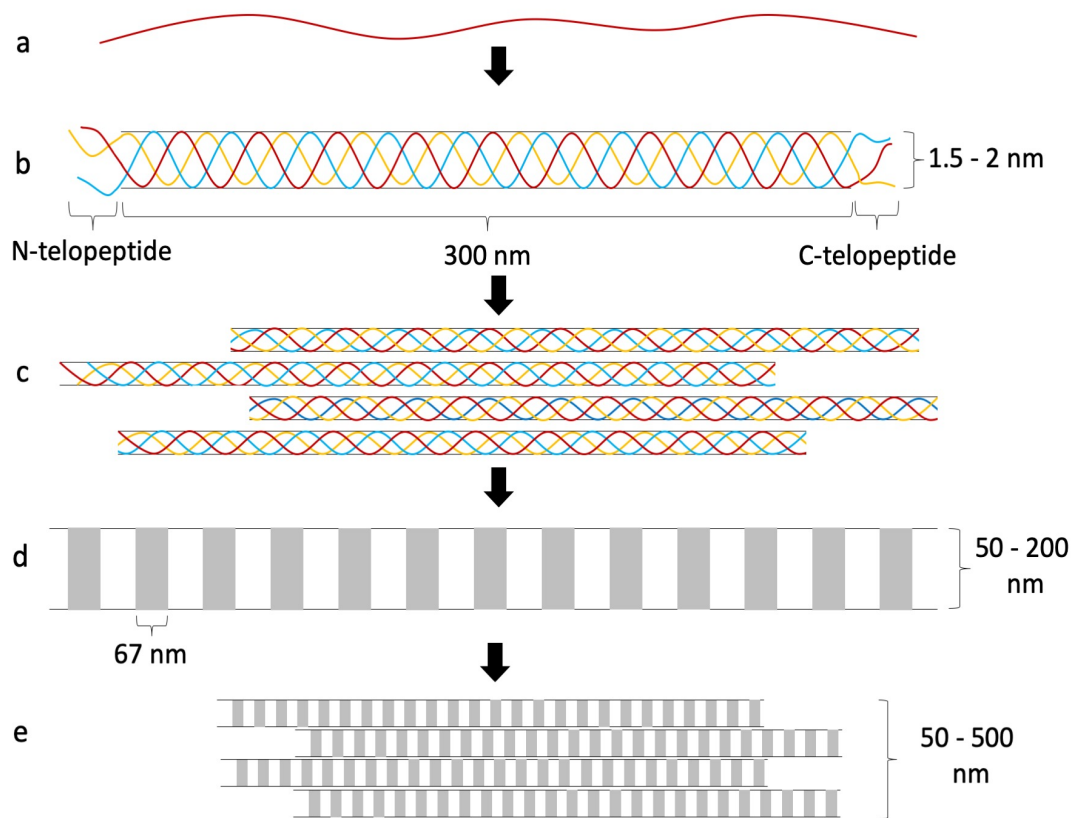
Figure 2.12: Collagen fiber formation. (a) α-chain, (b) procollagen molecule, (c) collagen molecule assembly, (d) collagen fibril, (e) collagen nanofiber.

2.3.2 Scaffold fabrication technologies

Various techniques are available to fabricate scaffolds, essentially forming porous structures necessary for cell and tissue growth. Figure 2.13 shows the general scaffold fabrication technologies used to produce these porous structures.
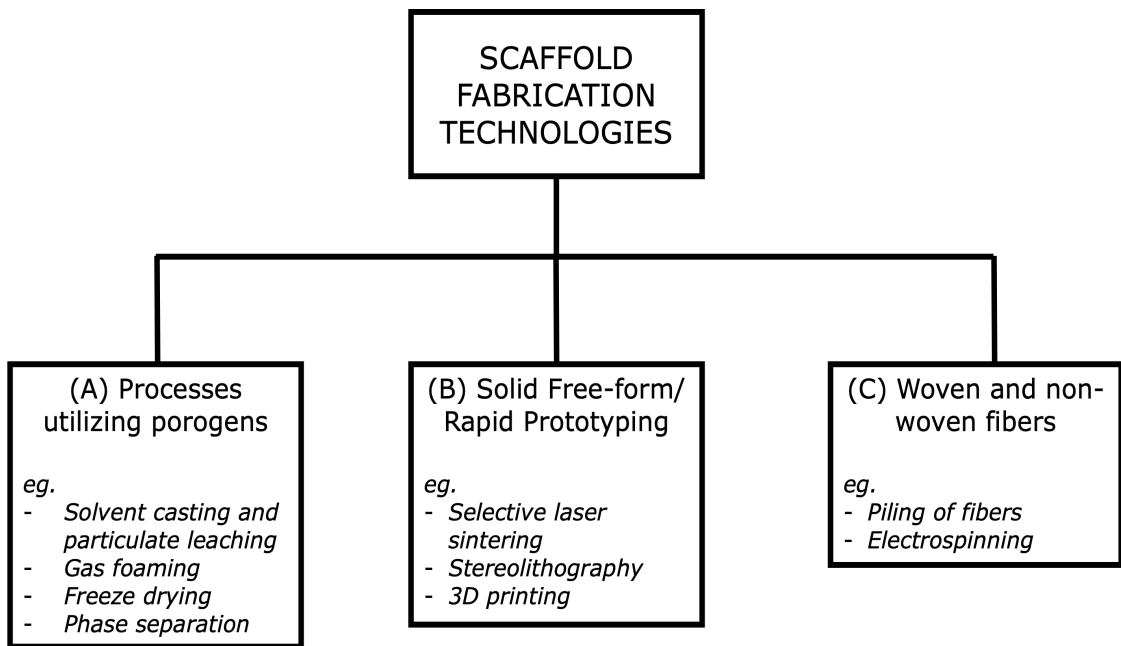
Figure 2.13: General scaffold fabrication technologies used in producing porous artificial ECM.

A) In this process, the scaffold material is mixed with porogens which can be gases (e.g., carbon dioxide), liquids (e.g., water) or solids (e.g., paraffin) either in solid form or in a solvent. The mixture is then casted and porogens can be removed by melting, evaporation, or sublimation.

B) In solid free form/rapid prototyping, materials are delivered to selected point in space forming a porous structure.

C) Porous structures can also be produced by sequential layering of multiple woven or non-woven fibers. These layers are generally bonded together either by heat or adhesives. Fibrous network are

also generated by electrospinning utilizing high voltage to charge up melt or dissolved material forming a continuous jet fibers [65].

2.3.3 Marine collagen

Collagen can be isolated and extracted from most living animals in view of it being one of the most abundant proteins in the world. Type I collagen is most widely used in biomedical applications largely derived from porcine, bovine, and ovine dermis and tendons. Nevertheless, type II collagen is also obtained from cartilaginous tissues of porcine, bovine and chicken. These mammalian sources however raise concerns regarding their immunogenicity and potential disease transmission in tissue engineering applications, while the use of porcine sourced collagens may be deterred by certain religious beliefs. Alternatively, marine collagen isolated from jellyfishes, sponges and specifically fish wastes (e.g., skin, bone, fins and scales) have been widely reported, and is finding increasing application in tissue engineering. Interestingly, it is known that the thermal stability of collagen sourced from fishes varies based on the temperature of their natural habitat which can be attributed to the content of proline and hydroxyproline[60], [62].

Three significant methods for collagen extraction include the use of neutral salt solutions, dilute acid solutions, with and without proteolytic enzyme. Since young collagens have relatively lower

degree of cross-linking, their solubility in neutral salt solutions aid in its isolation from native tissues [66]. However, relatively mature collagens require dilute acidic solutions such as 0.5 M acetic acid (AA) where these are necessary in cleaving intermolecular aldimine cross-links between collagen molecules. Keto-imine cross-links present in more developed collagens are resistant against dilute acidic solutions, therefore proteolytic enzymes, often pepsin, together with dilute acidic solutions are utilized. During this process, atelocollagens are obtained because of removal of telopeptide regions which enables collagen molecules to dissociate from its fibrillar structure. The use of enzymatic extraction is also known to significantly increase collagen yield [62].

From marine invertebrates, isolation of collagen type I from jellyfishes [67]–[71], sea urchins [72], [73], squids [74] and starfishes [75] have been reported. Collagen type II was also yielded from squid [76]. Collagen, mainly type I, has also been derived from a variety of fishes, summarized in Table 2.5.

Table 2.5: Summary of collagen isolated from fishes.

Species	Tissue	Extraction method	Collagen type	Ref.
Red drum	Scales	Enzyme (pepsin)	I	[77]
Indo-pacific king mackerel	Skin	Acid (AA)	I	[78]
Red snapper	Skin	Acid (AA)	I	[79]
Stargazing stonefish	Skin	Enzyme (pepsin)/ acid (AA)	I	[80]
Sharpnose stingray	Skin	Ultrasound assisted enzyme (pepsin)/ acid (AA)	-	[81]
Shark and ray (elasmobranch)	Cartilage	Enzyme (pepsin)/ acid (AA)	I and II	[82]
Shortfin scad	Wastes (bone and skin)	Enzyme (pepsin)/ acid (AA)	-	[83]

Small-spotted catshark	Skin	Acid (AA)	I	[84]
Rabbitfish	Skin	Acid (AA)	I	[85]
Bigeye tuna	Skin and scales	Acid (AA)	I	[86]
Tilapia	Scales	Acid (AA)	I	[87]
Nile tilapia	Skin	Enzyme (pepsin)/ acid (AA)	-	[88]

2.4 Electrospun Nanofibers Scaffold

2.4.1 Principles of electrospinning

The electrospinning technique is one of the most attractive scaffold fabrication methods in the grounds of its relative simplicity, robustness, reproducibility and cost-effectiveness in producing nanofibrous materials. The typical set up consists of a high voltage supply, syringe pump, syringe, metallic collector and spinneret. Solution electrospinning involving the use of a polymer with sufficient molecular weight dissolved in a suitable volatile solvent is mostly favoured in producing TESs as opposed to its alternative, melt electrospinning. In melt electrospinning, molten polymer is attained through elevated temperature which necessitates the need for the extra heat supply[89]. Additionally, melt electrospinning results in fibers within the submicron range[20] which isn't favourable in producing TESs due to the inability to mimic the nanostructured ECM. Particularly in solution electrospinning, the syringe pump provides a constant flow of polymer solution ejected through the metallic spinneret where a hemispherical droplet is suspended at the spinneret's tip. Electrical charge is introduced into the droplet and as the critical voltage is achieved, the droplet at the end of the spinneret conforms into a conical shape, prominently known as the Taylor's cone. During this process, the electrostatic repulsive force acts directly opposite to the surface tension of the droplet and a single

fine jet of polymer solution is formed at the end of the cone. A stable Taylor's cone is imperative for continuous electrospinning, hence a balance between solution depletion and supply must be maintained. Subsequently, the jet travels through the electrically charged gap between the end of the conical droplet and the grounded metallic collector in a whipping motion where the polymer solution is stretched due to bending instability, while the solvent evaporates. With an optimum gap to conserve attraction of charged jet to the grounded collector and sufficient for complete evaporation of solvent, continuous, dry, ultrafine and non-woven membrane composed fibers in the nanometer range is obtained[20][90]. Figure 2.14 shows the conventional electrospinning set up.
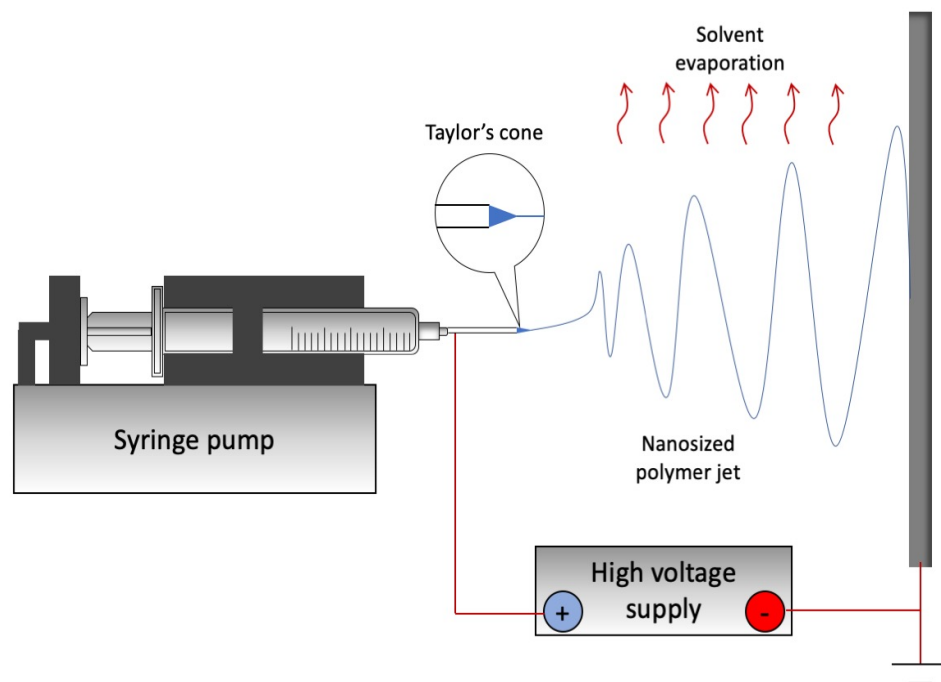
Figure 2.14: Electrospinning set up.

Successful electrospinning requires careful control over a few parameters, namely the solution parameter, process parameter and ambient conditions:

A) Solution parameter

Two major parameters related to the polymer solution determine its electrospinnability, namely the polymer concentration and electrical conductivity. Needless to say, the polymer solution should be prepared with polymers dissolved in their respective good solvent, which in some cases involve a mixture of multiple solvents. For successful electrospinning, a minimum concentration is required to facilitate sufficient chain entanglement to sustain a continuous jet during its stretching and whipping phase. Slightly below the minimum concentration, polymer jets break up forming discontinuous and beaded fibers. Further reducing the concentration would lead to electrospraying where fragmented polymer droplets are collected. In contrast, too high a concentration leads to the inability to electrospin due to the difficulty to overcome the viscoelastic force, while rapid evaporation of solvent at the spinneret's tip may even lead to clogging. Within a suitable range, increment in concentration leads to increased fiber thickness. Increase in viscosity and surface tension of the solution is directly affected by the increase in concentration where thinner fibers are formed at the lower end of these two properties. Alternatively, viscosity and surface tension can be

reduced with the use of surfactant without altering the polymer concentration[91], [92].

Similarly for the electrical conductivity of the solution, there exist an optimum range for successful electrospinning. A solution that is too electrically insulating will not be able to allow sufficient electrostatic repulsion from within the solution to the surface due to the lack of charge. On the other hand, solutions that are too electrically conductive do not possess the capacity to accumulate charge within the polymer droplet which leads to the difficulty in generating a Taylor's cone. One common strategy to increase the electrical conductivity of a solution is to include ionic additives such as salts[90], [93], [94].

B) Process parameters

The process parameters comprise of the applied voltage, solution flow rate and working distance (e.g., the distance between the tip of the spinneret and the collector). The applied voltage plays a direct role in regulating the repulsive force through the Taylor's cone and the charge density within the polymer jet. Higher applied voltage generally favors the formation of thinner fibers[95], [96]. However, contradicting results have been reported where the increase in applied voltage was accompanied by increased fiber diameter[97],

[98] which is attributed to a higher volume of solution ejected caused by the higher electrical repulsion at the solution droplet[99].

As for the solution flow rate, it is established that a higher flow rate contributes to larger fibers. The final process parameter is the working distance in which an optimum distance needs to be established to obtain dry nanofibers. A larger working distance promotes the elongation of the polymer jet to form thinner fibers, while too short a working distance not only produces thick fibers, but wet fibers will be collected due to incomplete evaporation of solvent. The presence of solvent on the collector in excessive amount may also cause fibers to fuse which could severely affect the final morphology of the electrospun membrane. When the working distance is too large, fibers will not further decrease in thickness which is correlated to the solidification of the polymer jet[90].

C) Ambient conditions

Electrospinning under raised ambient temperatures causes the reduction in viscosity and surface tension of the polymer solution. At elevated temperatures, solvent evaporation occurs at a higher rate which favors the formation of thinner fibers. Similarly, this holds true when the relative humidity is low. However, overly rapid evaporation due to too high temperature or too low humidity hamper the stretching of the polymer jet causing thicker fibers to form. When the

humidity goes too high, evaporation rate reduces where collected fibers may not fully dry and water vapour may penetrate the polymer jet causing changes in morphology such as pore formation along fibers[100], [101].

2.4.2 Electrospinning as a scaffold fabrication technique

Owing to its robustness, the electrospinning technique can prepare TESs that meet the requirements in application. For instance, to fabricate a biocompatible scaffold, one could simply choose a biocompatible starting polymer. As discussed in section 2.3, collagen and PNIPAm are a couple of biocompatible natural and synthetic polymer, respectively, that have been successfully electrospun into nanofibers (albeit drawbacks on risk of disease transmission and collagen denaturation for electrospun collagen scaffolds). Morphological properties such as fiber diameter, pore size and porosity are all well tunable and achievable by setting control parameters, where different tissue lineage require different morphological dimension, as reviewed by Ameer J.M. et. al.[102]. Similarly with mechanical properties, specific treatments can be used on electrospun constructs such as cross-linking. It was mentioned in section 2.3 that cross-linking was used to improve aqueous stability of electrospun collagen. Cross-linking was also used to tune their mechanical properties[103], [104]. Finally, electrospinning is an

inexpensive technique involving a simple set up and provides great reproducibility and scalability in fabricating nanofibrous materials. Needleless electrospinning has been introduced to upscale the production of nanofibers[105].

2.4.3 Advances in electrospun collagen scaffold for tissue engineering

Electrospinning is one of the most promising methods in producing TESs capable of physically mimicking the native structure of collagen in the ECM. To that end, electrospinning of collagen itself has been widely reported with the objective of mimicking the biochemical properties and cues that promote cellular adhesion, proliferation, and differentiation. Electrospinning of collagen for the application of tissue engineering was first reported by Matthews et. al. [106], utilizing the fluoroalcohol, hexafluoroisopropanol (HFIP), as solvent. It was reported that the periodic banding pattern of collagen fibrils was retained post electrospinning. However, the preservation of the banding pattern and collagen triple-helical structure were not quantified. As HFIP went on to become a popular solvent in collagen processing, various studies have pointed out its common drawbacks which include concerns on its high cost [107], cytotoxicity [108], environmental impact [109] and even collagen denaturation [107],

[108]. With these concerns, alternative solvents to electrospin collagen have been explored and reported.

A review was conducted in part of an effort to grasp the development and advancement in collagen electrospinning. Briefly, publications concerning the subject were searched on the SCOPUS database with the keywords "collagen" and "electrospinning", using the Boolean operator AND. This returned a list of publications from the year 2002 (first publication on collagen electrospinning by Matthews et. al. [106]) up to 2022 (recent). Returned search results were shortlisted based on their relevance in neat collagen processing via electrospinning as TESs, in reference to the title and abstract of publications, which narrowed down the number of publications to 77. Finally, information (e.g., collagen source, collagen type, additives in electrospinning solution, solvent, collagen concentration, needle gauge, collector type, electrospinning parameters, ambient conditions, cross-linking method, cultured cells, fiber morphology, preservation of collagen D-banding, preservation of triple-helical structure, mechanical properties, porosity, pore size and denaturation temperature) was extracted from the list of publications, with 12 publications taken out due to reasons such as incomplete information and not quantified processing parameters, leaving 65 publications.

Figure 2.15 shows that a large proportion of collagen used in electrospinning were isolated from bovine source (i.e., 73 %), especially from their skin. This is followed by rat, fish, porcine and equine at 15, 5, 4 and 4 %, respectively.
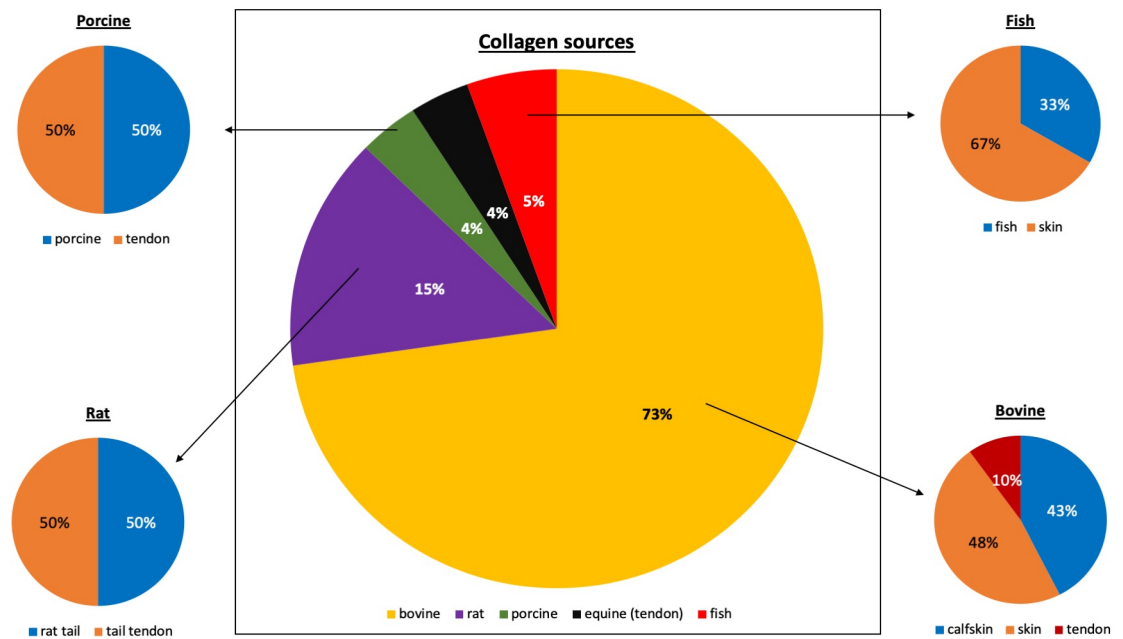
Figure 2.15: Proportion of collagen sources used in electrospinning based on publications from year 2002 up to 2022.

Figure 2.16 shows that collagen has been electrospun from four general solvent systems which include fluoroalcohol, AA, phosphate buffered saline (PBS):ethanol (EtOH), and EtOH:hydrochloric acid (HCl) systems. Fluoroalcohol systems were mostly used (i.e., 62 %). This is followed by greener systems of AA, PBS:EtOH, EtOH:HCl systems at 24, 11 and 3 %, respectively. Fluoroalcohol systems

include the use of HFIP, 85 % HFIP, HFIP:AA (1:1) and TFE, and the
frequency in reported use is summarized in Figure 2.17.
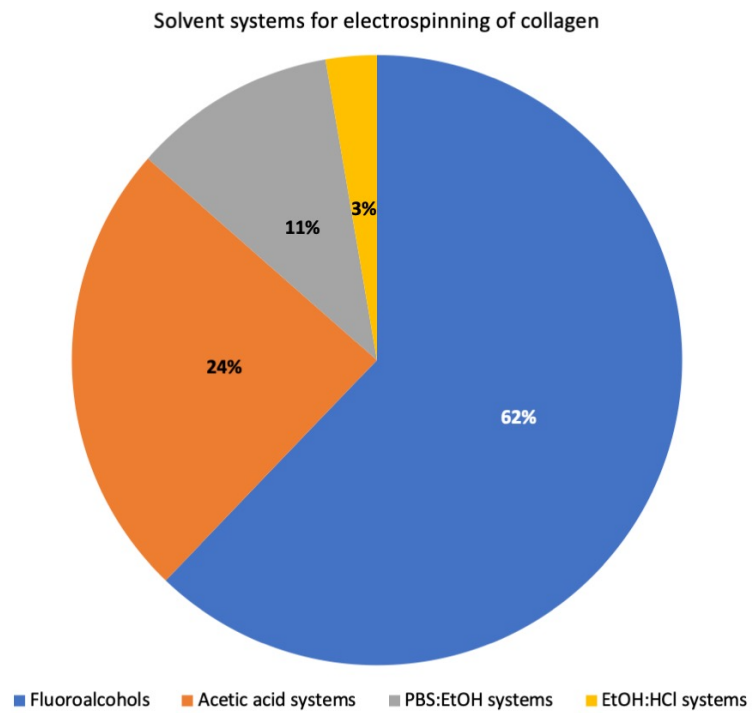
Figure 2.16: Proportion of solvent systems used in electrospinning of
collagen based on publications from year 2002 up to 2022.
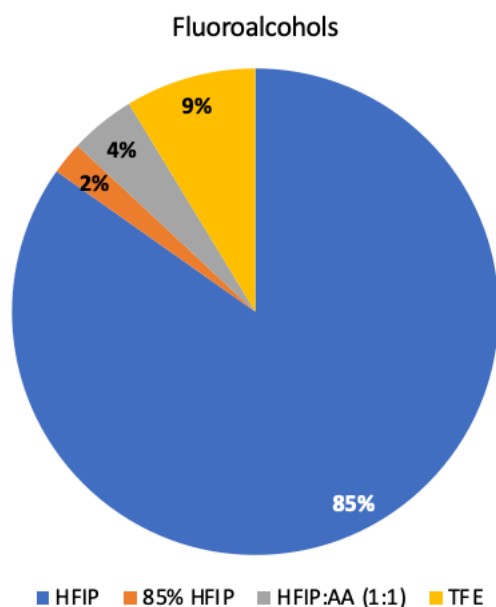
Figure 2.17: Proportion of fluoroalcohol systems used in electrospinning of collagen.
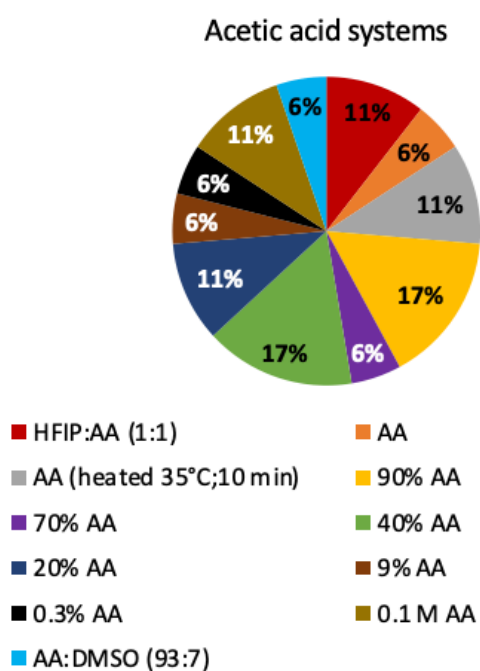
Figure 2.18: Proportion of AA systems used in electrospinning of collagen.

In AA systems, AA has been used in the concentration range of 0.3 % to glacier AA. Preparation of collagen solution with glacier AA with heating (i.e., 35 °C for 10 mins) has also been reported. Aside from that, binary solvents of AA:HFIP and AA:dimethyl sulfoxide (DMSO) has also been reported to produce collagen fibers via electrospinning. The proportion of AA systems reported are summarized in Figure 2.18.
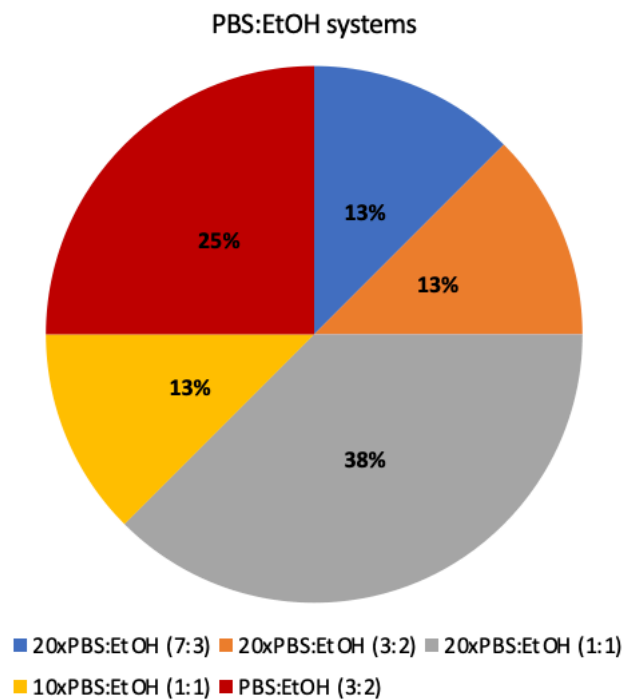
Figure 2.19: Proportion of PBS:EtOH systems used in electrospinning of collagen.

Figure 2.19 shows that in PBS:EtOH systems, 20xPBS:EtOH (1:1) is most commonly used, followed by PBS:EtOH (3:2), 20xPBS:EtOH

(7:3), 20xPBS:EtOH (3:2) and 10xPBS:EtOH (1:1) at proportions of 38, 25, 13, 13 and 13 %, respectively.
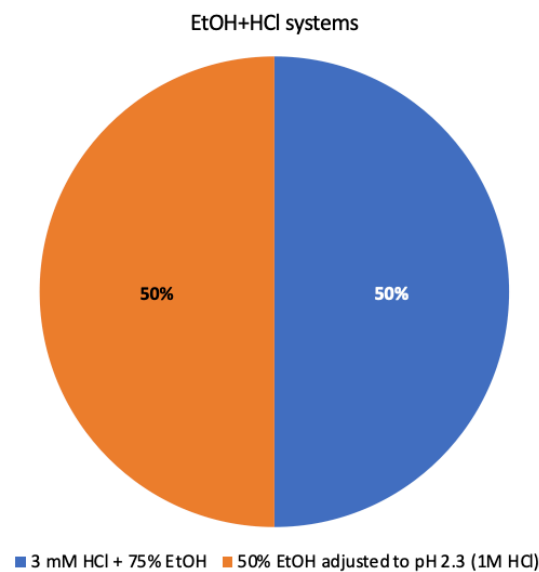
Figure 2.20: Proportion of EtOH:HCl systems used in electrospinning of collagen.

Lastly, Figure 2.20 shows the proportion of EtOH:HCl systems used. A very small amount of this solvent system has been reported, as shown in the earlier Figure 2.16 (i.e., 3 %). The addition of HCl in the solvent system mainly serves the purpose of lowering the pH of the solvent.

A typical drawback of neat electrospun collagen is its weak aqueous stability[110]. This hinders its use as stable scaffolds in tissue culture applications. Considering that, various cross-linking methods have been employed to improve the aqueous stability of electrospun collagen to produce viable scaffolding for tissue culture. Common

chemical cross-linking methods include the use of glutaraldehyde (GTA) vapor[111]–[116], GTA immersion[117], [118], 1-ethyl-3-(3-dimethylaminopropyl)carbodiimide hydrochloride (EDC) coupled with N-hydroxysuccinimide (NHS) [104], [108], [110], [119], EDC[110], [120], [121], and genipin[122]–[124]. Other less common methods that have been reported for chemical cross-linking electrospun collagen include hexamethylene diisocyanate (HMDI) (immersion)[125], transglutaminase (enzymatic cross-link)[122], laser irradiation (photoinitiated by rose bengal)[126], combination of 3 % glycerol + 11 % citric acid (CA) + 2.5 % sodium hypophosphite (SHP)[127], and 1,4-butanediol diglycidyl ether (BDDGE)[104]. Figure 2.21 summarizes the common chemical cross-linking methods used in proportion of its frequency in publication. The most commonly used cross-linker is GTA followed by EDC/NHS, EDC and genipin at 53, 21, 19, and 7 %, respectively.
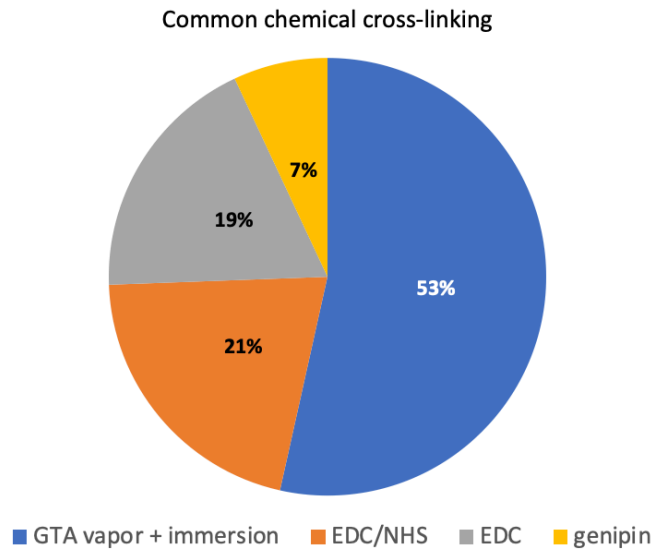
Figure 2.21: Proportion of common chemical cross-linking methods for electrospun collagen.

Aside from chemical cross-linking, electrospun collagen were also physically cross-linked by employing UV ray[122], [128], dehydrothermal (DHT) treatment[129], vacuum dehydration[130], [131] and pre-fibrillization by ammonia exposure (fibrillogenesis triggered by increase in pH)[132].

In-situ cross-linking with EDC/NHS has also been reported with the cross-linkers blended into the electrospinning solution, which aids to better disperse the cross-linker and improve bulk cross-linking of electrospun collagen as opposed to surface cross-linking achieved by exposure of cross-linker post-electrospinning[133]. In other instances of in-situ cross-linking, genipin and GTA were also blended into collagen solutions[134].

Finally, combinations of physical and chemical cross-linking have also been reported which include DHT-EDC[129], vacuum dehydration-EDC[131] and in-situ genipin and GTA cross-linking followed by UV treatment[134]. Table 2.6 shows a summary of optimum electrospinning parameters for various collagen sources/type reported in the literature.

Table 2.6: Summary of optimum electrospinning parameters for various collagen sources/types.

Collagen source	Solvent	Concentration % (g/ml)	Flow rate (ml/h)	Voltage (kV)	Distance (cm)	Ref.
Rat tail tendon (type I)	HFIP	6	1	20	15	[135]
Bovine skin (type I)	HFIP	10	4.3	30	18	[136]
Tilapia skin (type I)	HFIP	5, 11, 18	1.8	20	-	[137]
Bovine skin (type I)	40 % AA	0.25	-	1.5	0.58 (mm)	[138]
Bovine tendon (type I)	90 % AA	20	0.5-3	25-45	10	[139]
Fish (type I)	AA:DMSO (93:7)	10	0.6	17	23	[109]
Calf skin (type I)	PBS:EtOH (3:2)	15	1	17	15	[140]
-	20 % AA	30	0.06	24	15	[104]

-	TFE	10	0.9	18	15	[104]
Porcine (type I)	20 % AA	10	0.1	12	12	[141]
Type I:III (95:5)	50 % EtOH (pH 2.3)	15	1	20	15	[127]
Transgenic tobacco (recombinant type I:III (95:5))	HFIP	12	4 – 8	30	18	[131]
Bovine tendon (type I)	90 % AA	10	2	20	10	[142]
Calfskin (type I)	HFIP	2.4	0.6	25	10.16	[143]
Bovine skin (type I)	TFE	10	0.012-0.03	20-22	15	[144]
Hoki fish skin (type I)	40 % AA	20	0.3	10	10	[145]
Hoki fish skin (type I)	HFIP	8	0.3	10	10	[145]

Bovine achilles tendon (type I)	70 % AA	40	0.75	20	15	[146]
Equine achilles tendon (type I)	0.1 M AA	2.5	0.6	15	18	[147]
Bovine skin (type I)	AA	-	0.7	20	10.5	[148]
Bovine skin (type I:III (95:5))	20xPBS:EtOH (1:1)	16	0.5	20	12	[133]
Calf skin (type I)	HFIP:AA (1:1)	7	0.2	15	20	[123]
Rat tail (type I)	40 % AA	25	0.3	15 to 16	6 to 8	[126]
Calf skin (type I)	85 % HFIP	5	0.25	11	13	[122]
Bovine skin (type I:III (95:5))	10xPBS:EtOH (1:1)	16	1	20	10	[108]

Equine achilles tendon (type I)	0.3 % AA	1	0.6	18	18	[149]
Articular cartilage of fetal calf leg (type II)	HFIP	6	2	22	12.7	[110]
Chicken sternum (type II)	HFIP	-	-	-	-	[113]
Chicken sternal cartilage (type II)	HFIP	4	2	22	10.16	[112]
Calf skin:human placenta (type I:III (1:1))	HFIP	6	5	25	12.5	[111]
Human placenta (type III)	HFIP	4	5	25	12.5	[111]
Human placenta (type I)	HFIP	8.3	5	25	12.5	[111]

2.4.4 Advances in electrospun PNIPAm scaffold for tissue engineering

Work on electrospun PNIPAm have been fairly reported and its potential application include drug delivery[150], tissue engineering[12], [151], wireless control[152], fog harvesting[153], "smart" sensor and artificial muscle[154]. Particularly in the field of tissue engineering, electrospun PNIPAm scaffold finds its application owing to its inherent biocompatibility. Young R. et. al. report of uniaxially aligned PNIPAm nanofibers that are thermo-responsive and biocompatible that find application in vascular, bone or neural grafts where aligned nanofibrous scaffolds are desired[12]. For drug delivery, near infrared responsive (NIR) PNIPAm nanofibers was achieved by incorporation of gold nanorods (GNR) which exhibit absorption in the NIR range where GNRs generate heat due to the plasmon resonance effect in response to NIR irradiation[150].

Various molecular formats of PNIPAm have been successfully electrospun into nano/micro-fibers, ranging from 35 000 to 658 000 Da. Electrospun neat or linear PNIPAm exhibits poor aqueous stability and can be improved by cross-linking, especially when its molecular weight is relatively low (e.g., 40 000 Da), as noted by Cicotte et. al.[10]. Additionally, cross-linked PNIPAm as a starting material has poor electrospinnability. Wang J. et. al. reports that pre-crosslinked

PNIPAm cannot be electrospun and attributed this to its insoluble nature[11]. Use of octaglycidyl polyhedral oligomeric silsesquioxane (OPEPOSS) as cross-linker has been reported for PNIPAm electrospinning, where OPEPOSS was introduced into the electrospinning solution, followed by heat curing (120-160 °C) of the electrospun material[11], [12], [150], [153], [154].

PNIPAm was generally electrospun from organic solvents. However, PNIPAm electrospun from water has been studied by Schoolaert E. et. al. where it was reported that the temperature of the electrospinning solution has to be kept well below 30 °C, while control over ambient temperature and relative humidity was necessary to ensure electrospinnability[155].

Finally, cells tested on electrospun PNIPAm include U-87 MG (brain cancer cell)[150], L-929 fibroblasts[12], [156], EMT6 and MC3T3-E1 cells[10]. Table 2.7 shows the summary of the optimum electrospinning parameters for PNIPAm from the literature.

Table 2.7: Reported optimum parameters for PNIPAm electrospinning in literature.

Molecular weight (Da)	Concentration (wt %)	Solvent	Voltage (kV)	Flow rate (ml/h)	Distance (cm)	Application	Ref.
533000	17	DMF	4 to 9	0.5-3	7 to 21	-	[157]
300000	10	THF:DMF (1:1)	13.5	3	12	Drug delivery	[150]
658000	17	DMF	6.75	1	14	-	[158]
385000	15	THF:DMF (1:1)	9	0.6	18	Tissue engineering	[151]
300000	10	95% EtOH	12	1	10	Dressing carrier for wireless control	[152]
300000	12	THF:DMF (1:1)	15	0.1	10	Tissue engineering	[12]

300000	20	Chloroform: EtOH (2:1)	17	9	15	Drug delivery	[159]
300000	10	THF:DMF (1:1)	15	0.5	15	Fog harvesting	[153]
300000	10	water	15 to 20	0.5	25	-	[155]
300000	12	DMF	10	0.6	12	"Smart" sensor/nano-reactor/catalysis/artificial muscle	[154]
-	25	EtOH	9 to 11	0.4	10	Drug delivery	[156]
40000/300000	10 and 20	MeOH	1kV/cm	3.5	1kV/cm	Mammalian cell culture	[10]
650000	4 to 21	DMF	6	0.5	14	-	[160]
300000	10	THF:DMF (1:1)	13	0.6	17	-	[11]

| 35000 | 15 | MeOH | 20 | - | 20 | - | [161] |

*Abbreviation: N, N-dimethylformamide (DMF)

2.5 Collagen Functionalized Electrospun Polymers

Several techniques of collagen functionalization onto electrospun polymer nanofibers have been reported, with the goal to improve the bioactivity of synthetic polymeric nanofibers. These techniques include surface functionalization, blending and co-electrospinning as discussed in this subsection.

2.5.1 Wet chemical surface functionalization

Surface functionalization of electrospun nanofibers can be achieved by coating with dilute collagen solution. However, several distinct coating methods were reported in the literature. Muniyandi P. et. al. worked on coating calf skin derived type I collagen on electrospun PLLA by single drop coating for physical adsorption with 0.1 % collagen solution[15]. Other physical adsorption methods were also reported where Yang X. et. al. coated poly(D,L-lactide-co-glycolide) (PLGA) nanofibers by dropping fixed volume of collagen solution prepared in 0.5 % AA and let to naturally dry[162]. Tanha S. et. al. coated PCL nanofibers by dipping the membrane in 10 mg/ml of collagen in AA overnight[163].

Cross-linking after collagen coating was also employed which covalently functionalizes electrospun nanofibers to collagen. For instance, Bian T. et. al. functionalized electrospun PVP by soaking

twice in 64 mg/ml collagen solution followed cross-linking with GTA[164], while Janani G. et. al cross-linked collagen coated gelatin nanofibers with roboflavin[165].

Finally, precipitation of collagen from its solution onto electrospun nanofibers was also employed, where PLGA and polylactic acid (PLA) nanofibers were coated with collagen solution of 0.2 mg/ml in 0.02 M AA followed by immersion in ammonia solution to attain basic pH to induce collagen precipitation onto the nanofibers, as reported by Bacakova M. et. al[166]. Table 2.8 summarizes the recent literature on collagen coated electrospun polymer.

Table 2.8: Summary of collagen coated electrospun polymer from the literature.

Electrospun polymer	Collagen source	Collagen type	Collagen solvent	Collagen concentration	Application	Findings	Ref.
PCL	bovine	I	-	-	cartilage tissue engineering	scaffold with increased fiber size and hydrophilicity	[167]
PLLA	calf skin	I	-	0.1 %	cardiac tissue engineering	scaffold capable of modulating proteome expression	[15]
PLGA/PCL	rat tail	I	-	2 %	orofacial tissue regeneration	scaffold with enhanced bone mineralization	[168]

PCL	human	IV	HBSS*	0.3 mg/ml collagen diluted 1:12 in HBSS	kidney proximal tubule grafts	proof-of-concept kidney tubule graft	[169]
PVP	-	-	-	64 mg/ml	bone tissue engineering	biomimetic bone scaffold	[164]
PLGA	-	-	0.5 % AA	-	bone tissue engineering	scaffold with enhanced expression of osteogenic marker genes	[162]
PHBA*/gelatin	-	-	0.1 M AA	4 %	wound healing	scaffold with enhanced wound healing efficiency	[170]

PCL	-	-	AA	10 mg/ml	wound healing	bioactive scaffold	[163]
PLGA	rat tail	-	0.02 M AA	0.2 mg/ml	skin cell carrier	scaffold with enhanced adherence, proliferation and spreading of keratinocytes	[166]
PLA	rat tail	-	0.02 M AA	0.2 mg/ml	skin cell carrier	scaffold with enhanced adherence, proliferation and spreading of keratinocytes	[166]

PMMA*	rat tail	I	-	0.05 mg/ml	muscle tissue engineering	scaffold with enhanced proliferation and migration of fibroblasts	[171]
Gelatin	-	-	-	-	breast cancer studies	scaffold with enhanced cell attachment	[165]

*Abbreviation: Hank's balance salt solution (HBSS), poly(3-hydroxybutyric acid) (PHBA), poly(methyl methacrylate) (PMMA)

2.5.2 Blending

Incorporation of collagen to electrospun polymers can be achieved by preparation of an electrospinning solution containing a blend of collagen and the polymer, which requires a common solvent for both. Hajikhani M. et. al. recently fabricated a mucoadhesive patch by coaxial electrospinning, with PLA-polyethylene oxide (PEO) nanofiber core and PVP-type I collagen (from bovine achilles tendon) as shell with HFIP:EtOH (7:3) as shell polymer solvent[172]. Fish atelocollagen-PCL nanofibrous mat for wound healing was fabricated by a blend of the polymers in HFIP as reported by Chandika P. et. al.[14]. In the work of Zhou X. et. al., a bioactive electrospun scaffold to enhance osteogenic differentiation of MC3T3-E1 was achieved by direct incorporation of type I collagen into PLGA/PCL blend in TFE in the presence of calcium ions[173]. Various polymers have been blended with collagen for electrospinning, and Table 2.9 summarizes the solvents and polymers reported in recent literature.

Table 2.9: Summary of electrospun collagen-blended polymer and respective solvents from the literature.

Solvent	Collagen type	Blended polymer	Application	Ref.
HFIP:EtOH (7:3)	I	PVP	drug delivery	[172]
HFIP	I	PCL	wound healing	[14]
TFE	I	PLGA/PCL	bone tissue engineering	[173]
TFE	I	CS*	tendon tissue engineering	[174]
50 % AA	I	PPy*/chitosan	tissue engineering	[175]
HFIP	I	PCL	bone tissue engineering	[176]
TFE	I	POC*	bone tissue engineering	[177]
20 % AA (collagen) + chloroform (PLA/PEO)	I	PLA/PEO	myocardial tissue engineering	[178]
TFE	-	aspirin loaded PLGA nanoparticles	bone tissue engineering	[13]
HFIP:EtOH (7:3)	I & II	PCL	tissue engineering	[179]

HFIP (collagen) + FA* (chitosan/PCL)	I	chitosan/PCL	bone tissue engineering	[180]
HFIP	-	gelatin	tissue engineering	[181]
90 % AA	-	PCL	-	[182]
HFIP (collagen) + Chl*:DMF (9:1) (PLGA)	I	PLGA	drug delivery	[183]
HFIP	I	PLLA	-	[184]
HFIP	I	PCL	bone tissue engineering	[185]
HFIP	I	PCL	bone tissue engineering	[186]

*Abbreviation: chondroitin sulfate (CS), polypyrrole (PPy), poly(1,8-octanediol citrate) (POC), formic acid (FA), chloroform.

2.5.3 Co-electrospinning

The concept of co-electrospinning of collagen and a particular different polymer is generally conducted with separate solutions of collagen and the polymer, and electrospun simultaneously onto a common collector such that to promote overlapping of collagen and the polymer fibers. Optimised conditions to electrospin collagen and the polymer is necessary to form an independent set-up to its co-spun polymer solution. Polymers that have been co-electrospun with collagen include poly(L-lactide-co-caprolactone) (PLCL)[187]–[189], PLGA[190], [191], PCL[192], [193] and PLLA[194]. Collagen solutions for co-electrospinning were generally prepared in fluorinated solvents such as HFIP and TFE, which are well establish collagen solvents for electrospinning.

Chapter 3

METHODOLOGY

3.1 Materials

97 % NIPAm recrystallized once in n-hexane, KPS, 99 % SDS, 99 % BIS, activated carbon, celite, n-hexane, dialysis sacks with molecular weight cut-off of 12 kDA washed by immersion in deionized water (ddH$_2$O) for 5 hours, 99.5% sodium chloride (NaCl), 99% tris-hydrochloride (tris-HCl), 99% ethylenediaminetetraacetic acid (EDTA), 99% HCl, 99% glacial AA, 96% 2-ethyl-4-methylimidazole (EMI), methanol (MeOH), 99% DMSO, LMW commercially available PNIPAm (Mw= 40,000 g/mol) and gelatin from porcine skin (Type A) were purchased from Sigma Aldrich. THF and DMF were purchased from Chemiz (M) Sdn. Bhd. Commercially available PNIPAm of viscosity average molecular weight 300,000 g/mol was purchased from Scientific Polymer, USA. OPEPOSS cross-linker was purchased from Hybrid Plastics, Inc., USA. Fetal bovine serum (FBS), Glasgow's minimum essential media (GMEM) and 10x phosphate PBS were purchased from ThermoFisher Scientific. Leukemia inhibitory factor (rat) (LIF3010) was purchased from Merck Millipore. All chemicals were used as received, unless stated otherwise. Embryonic stem cell working medium (ESM) was prepared with 42.5 ml of GMEM, 7.5 ml

of FBS and 50 µl of 10 µg/ml LIF3010. Tilapia fish scales (TFS) was obtained for free from a local Tilapia fish farm in Broga, Semenyih.

3.2 Synthesis of PNIPAm

3.2.1 Recrystallization of NIPAm

Recrystallization of NIPAm was carried out with the solvent according to the work of Z. Farooqi et al.[195] following the typical recrystallization technique. Briefly, a boiling water bath was firstly prepared with a metal tray over a magnetic hotplate and a 100 ml conical flask containing approximately 50 ml of n-hexane heated in the water bath. A glass rod was placed in the heating n-hexane to facilitate bubble formation to indicate boiling. Boiling n-hexane was added dropwise to pre-measured raw NIPAm (~6 g) in a separate 100 ml conical flask held over the water bath and continuously swirled until NIPAm crystals are observed to be fully dissolved. An additional drop of boiling n-hexane was added as excess to prevent precipitation of NIPAm. Approximately 30-50 mg of activated carbon was added to the hot NIPAm solution and swirled for 2 minutes to remove high molecular weight and colored impurities. 40-60 mg of celite was added and the solution swirled for another 2 minutes to allow adsorption of activated carbon on celite. The hot mixture was then removed from the water bath and immediately gravity filtered through a fluted filter paper placed in a filter funnel, into a new 100

ml conical flask. The filtered solution was covered and left to cool at room temperature to allow recrystallization of NIPAm. In the instance where there are no observable signs of crystal formation, recrystallization can be induced by addition of small amount of NIPAm crystals, or gentle knocking of the conical flask against a laboratory benchtop. NIPAm crystals was vacuum filtered with constant washing with room temperature n-hexane, transferred to a petri dish and left to dry overnight in an oven at 50 °C. Dried recrystallized NIPAm was stored in a tightly sealed 50 ml centrifuge tube until further use.

3.2.2 Cross-linked PNIPAm

Cross-linked PNIPAm was prepared according to the methods of J. Khan et al. with modifications[44]. Briefly, cross-linked PNIPAm (x-PNIPAm) was prepared by dissolving 1 g of NIPAm, 0.02 g BIS (2 % (w/w) to NIPAm) and 0.04 g SDS (4 % (w/w) to NIPAm) in 100 ml of ddH$_2$O. The mixture was stirred for 1 h at 200 rpm with a magnetic stirrer and subsequently purged with nitrogen gas for 20 minutes to remove reactive oxygen. Then, the mixture was heated to 70 °C under a nitrogen atmosphere with maintained stirring at 200 rpm throughout the reaction. The initiator solution was prepared by dissolving 0.01 g (1 % (w/w) to NIPAm) of KPS in 5 ml of ddH$_2$O and added to the NIPAm mixture. The mixture turned cloudy 10 minutes after the addition of the initiator solution. Polymerization was allowed

to continue for 3 hours, and subsequently cooled to room temperature by quenching in a room temperature water bath. The solution was subjected to 4 cycles of centrifuging at 12000 rpm, 40 °C for 1 h each, where fresh ddH$_2$O was changed in between each cycle. The precipitate appeared as a viscous gel at the bottom of the centrifuge tube and was lyophilized at -59 °C, 0.012 mbar for 24 hours to yield a hard transparent solid.

3.2.3 Cross-linker free PNIPAm

Cross-linker free PNIPAm was prepared according to the methods of J. Khan et al. with modifications[44]. Briefly, cross-linker free PNIPAm was synthesized via radical polymerization from its monomer NIPAm in a 2-litre cylindrical jacketed reactor of 150 mm inner diameter with an anchor type impeller of 90 mm diameter. 2 g of recrystallized NIPAm and 0.08 g (4 % (w/w) to monomer) of SDS were first dissolved by magnetic stirring at 200 rpm in 200 ml of distilled water of ~pH 5 in a beaker at room temperature for 5 minutes. Once dissolved, the mixture was transferred into the jacketed reactor flask to be heated up to 80 °C and purged with nitrogen gas for 20 minutes. Each formulation of the mixture was subjected to continuous stirring of 50, 100 and 200 rpm, respectively to investigate the effects of agitation rate on the synthesized PNIPAM. 0.02 g (1 % (w/w) to monomer) of KPS initially dissolved in 5 ml of

distilled water was subsequently added to the mixture in the reactor flask to initiate polymerization. The thermal decomposition temperature of KPS begins at 70 °C to generate radicals to initiate the polymerization reaction. The temperature and stirring rate were maintained at throughout 4 hours of the synthesis. After 4 hours, the mixture was transferred into a beaker and quenched in a water bath at room temperature. After quenching, the mixture was transferred into dialysis sacks and dialyzed against distilled water for 7 days, replenished with fresh distilled water twice, daily. The dialyzed mixture was left within a freezer for a day at -18 °C and subsequently lyophilized in a freeze dryer for 48 hours at -59 °C and 0.012 mbar. The lyophilized samples were stored in tightly sealed centrifuge tubes covered with parafilm sheets prior to further use and characterization. Figure 3.1 shows the jacketed reactor set up used for PNIPAm synthesis. It should be noted that PNIPAm synthesized at agitation speed of 100 rpm (referred to as A100 PNIPAm hereafter) yielded the most desirable monomer-polymer conversion and was subjected to further use (i.e. electrospinning).

Figure 3.1: Jacketed reactor set up used for the synthesis of PNIPAm.

3.3 Characterization of synthesized PNIPAm

3.3.1 FTIR analysis

Fourier transform infrared (FTIR) spectroscopy analysis was conducted using Perkin Elmer (Frontier FT-IR/FIR, USA) spectrometer to investigate the functional groups specific to PNIPAm at wavenumber 400-4000 cm^{-1} with 16 scans and 4 cm^{-1} resolution. In the case of the study of agitation speed on the polymerization of NIPAm, conversion of NIPAm monomer to PNIPAm at different agitation speeds was also investigated. Freeze dried samples were used in all analyses.

3.3.2 Molecular weight analysis using Static Light Scattering

The molecular weight of PNIPAm was determined by static light scattering (SLS) using the Zetasizer (Nano ZS, UK). The Debye constant was computed after obtaining the change in refractive index (RI) against concentration of PNIPAm in MeOH, giving the refractive index increment (dn/dc) in the form of the gradient on a straight-line plot. The set of concentrations were prepared by serial dilution from a stock solution of 0.03 g/ml, and the RIs were determined by a refractometer (Atago 1T, Japan). A Debye plot was generated with the computed Debye constant, from a set of concentrations of PNIPAm in HPLC grade MeOH. The Debye constant is given by:

$$K = 4\pi^2 n^2 \frac{\left(\frac{dn}{dc}\right)^2}{\lambda^4 N_A} \qquad \qquad ………. \text{eq. 3.1}$$

where n represents the refractive index of solvent, λ represents the wavelength of light in vacuum, N_A the Avogadro's number and c the concentration of solute. The molecular weight was obtained by determining the inverse of the y-intercept of the Debye plot.

3.3.3 Particle size distribution analysis using Dynamic Light Scattering

The particle size and particle size distribution were characterized in terms of average hydrodynamic diameter and its polydispersity index (PDI), respectively. These were measured by dynamic light scattering (DLS) at 173 ° scattering angle using the Zetasizer (Nano ZS, UK). PNIPAm solutions of 1 mg/ml dissolved in HPLC grade MeOH filtered through 0.22 µm syringe filter were used for DLS measurement.

3.3.4 Thermo-responsive phase transition test

The thermo-responsive behavior of synthesized PNIPAm was visually observed in a solution of 0.01 g of PNIPAm dissolved in 10 ml of distilled water in a clear glass vial. The glass vial containing the PNIPAm solution was immersed in a water bath of 40 °C for 2 minutes

and the turbidity of the solution was observed and compared to as it was at room temperature. Increase in turbidity of PNIPAm solution indicates phase separation of PNIPAm from water, which can be attributed to the phase transition of PNIPAm above 32 °C.

3.3.5 Thermal degradation analysis using TGA

Thermal stability analysis was conducted using the Mettler Toledo (simultaneous TGA/DSC 1, USA) instrument. The analyses were performed in the temperature range of 30 to 500 °C at a heating rate of 10 °C/min under constant nitrogen gas flow of 20 ml/min. Approximately 5 mg of PNIPAm sample was used for the analysis. Differential scanning calorimetry (DSC) analysis was also conducted concurrently, and the results used to indicate the LCST of synthesized PNIPAm.

3.3.6 Morphology of synthesized PNIPAm

The morphology of synthesized PNIPAm was observed under FESEM (FEI Quanta 400 F, USA) operated under high vacuum at an acceleration voltage of 20 kV. Samples were mounted onto dedicated stubs with carbon tapes.

3.3.7 Rheological property of PNIPAm

The viscosities of the PNIPAm samples were measured with a viscometer (Brookfield Viscometer DV-II+ Pro, USA) at shear rates ranging from 0.74 to 135 s^{-1}. 0.5 mL of PNIPAm solutions at the concentration of 12 % (w/w) dissolved in MeOH were used for each analysis. The polymer concentration was selected arbitrarily at 4.5 % (w/w) as a preliminary concentration to electrospin PNIPAm given that the solution appeared as a free-flowing and relatively viscous liquid, as observed by sight. The same concentration was kept for all compared samples in order to compare their viscosities.

3.4 Collagen extraction from Tilapia fish scales

Collagen extraction from tilapia fish scales (TFS) was carried out according to the methods by Zhang et. al.[196] with slight modifications. Briefly, 50 g of TFS was cleaned by washing thrice with double-distilled water (ddH$_2$O). All further treatment of TFS were conducted at 4 °C. Cleaned TFS were soaked in 500 ml of salt buffer containing 1 M NaCl, 0.05 M tris-HCl and 20 mM EDTA for 48 hours to remove non-collagenous proteins, and washed thrice with ddH$_2$O. Next, the treated TFS were demineralized by soaking in 750 ml of 0.4 M HCl for 90 minutes, washed thrice with ddH$_2$O and dried in an enclosed container containing silica gel beads (renewed every day) for at least 4 days or until fully dry. Collagen was isolated from the

demineralized TFS by soaking in 250 ml of 0.5 M AA under constant gentle stirring for 48 hours. The mixture was then filtered through filter papers to remove insoluble materials. NaCl was then added to the filtrate to a final concentration of 0.9 M to induce salting out for 24 hours. After that, the solution was centrifuged at 10 000 rpm for 30 minutes at 4 °C, the precipitate collected and resolubilized in 250 ml of 0.5 M AA. Salting out, centrifuging and resolubilizing were repeated thrice to obtain collagen with higher purity. However, in the last resolubilizing process, only 150 ml of 0.5 M AA was used, given that this volume was sufficient to thoroughly disperse collagen and to reduce the acid usage since subsequent washing step will not be required. Furthermore, the reduction in volume of the resulting mixture help ease subsequent experimental steps (e.g., reduce usage of dialysis sacks and quicker drying). The solution was then transferred into dialysis sacks and dialysed against 0.1 M AA for 24 hours and ddH$_2$O for another 24 hours. Lastly, the dialysed solution was left to freeze in a -20 °C freezer for 2 days and lyophilised for 48 hours at -59 °C and 0.012 mbar in a freeze dryer. Dried collagen samples were stored in tightly sealed centrifuge tubes and kept in an enclosed container containing silica gel beads until further use and characterization. Figure 3.2 shows the flowchart for collagen extraction from TFS.
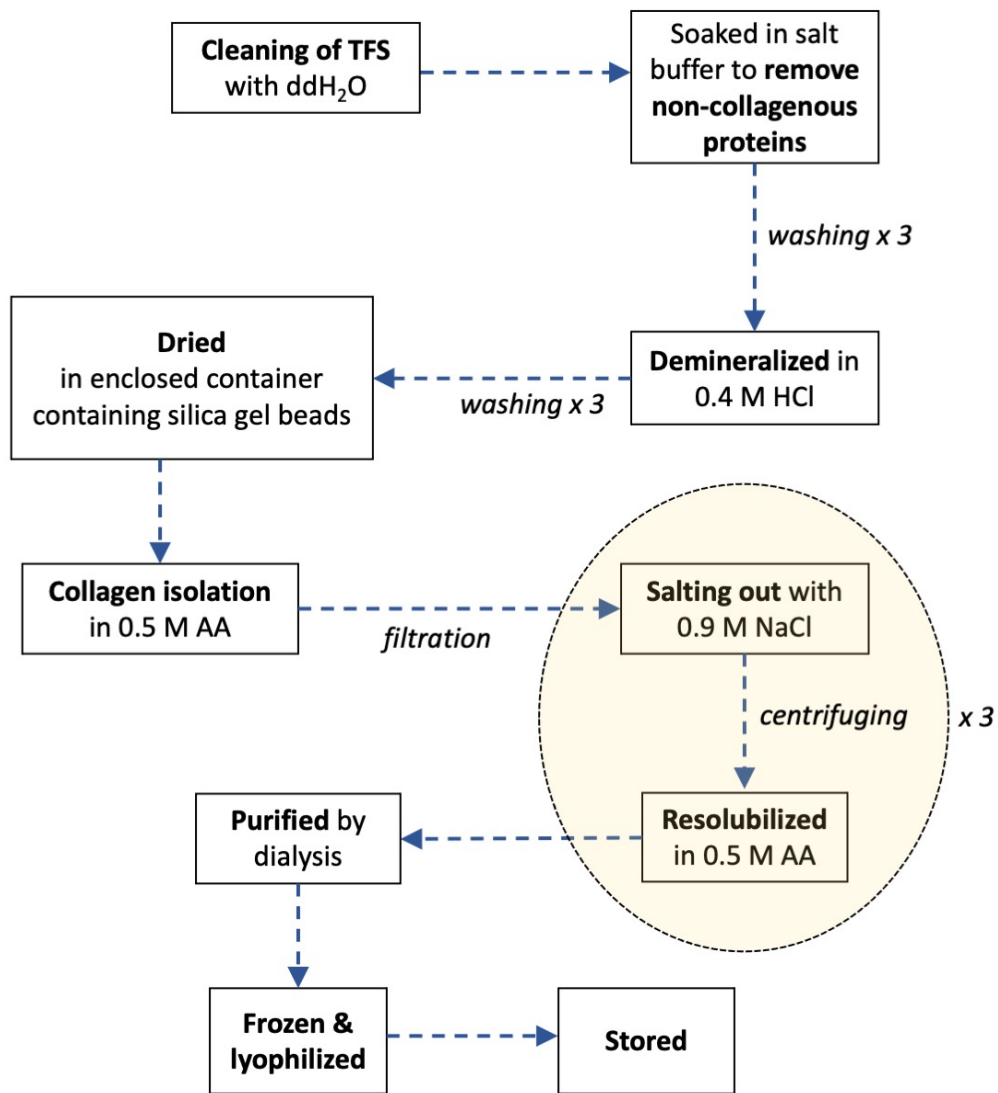
Figure 3.2: Flow chart of collagen extraction procedures from TFS.

3.5 Characterization of extracted collagen

3.5.1 FTIR analysis

FTIR spectroscopy analysis was conducted using Perkin Elmer (Frontier FT-IR/FIR, USA) spectrometer to investigate the functional groups specific to collagen at wavenumber 400-4000 cm^{-1} with 16

scans and 4 cm^{-1} resolution. Lyophilized samples in a freeze dryer were used in all analyses. The integrity of collagen triple helix was evaluated by taking the ratio of absorbance values at 1235 and 1450 cm^{-1}[197].

3.5.2 Morphology of extracted collagen

The morphology of lyophilized collagen was observed under FESEM (FEI Quanta 400 F, USA). Samples were mounted onto dedicated stubs with carbon tapes and directly viewed under low vacuum conditions at accelerating voltage of 10 kV.

3.5.3 Molecular weight analysis using gel electrophoresis

Sodium dodecyl sulfate polyacrylamide gel electrophoresis (SDS-PAGE) was conducted by the Laemmli method with slight modifications. Briefly, 8 % stacking gel and 4 % separating gel were prepared. 6 mg/ml collagen solution was prepared in protein sample buffer under double reducing condition in the presence of 2-mercaptoethanol. Further protein denaturation was carried out in a heating block at 99 °C for 10 minutes. BenchMark^{TM} bovine serum albumin (BSA) solution was used as molecular weight market ranging from 10 to 220 kDa. A loading volume of 10 µl was applied for all samples. Electrophoresis was left to run at 100 V for 4 hours. Resulting gel was stained overnight in 0.05 % Coomassie brilliant

blue R250 dissolved in 15 % MeOH and 5 % AA in ddH$_2$O. De-staining of gel was carried out for 2 hours in a solution containing 30 % MeOH and 10 % AA and lastly, with ddH$_2$O for 1 hour, replenishing with fresh water every 10 minutes. Bands were imaged using ChemiDocTM XRS+ Imaging System (BioRad, USA).

3.5.4 Thermal analysis using DSC

To determine the denaturation temperature of collagen and stability of its triple helical structure, DSC measurement was conducted in triplicates with a Q2000 device (TA Instruments, USA). Samples of about 5 mg were used and heated from 30 to 250 °C at a rate of 10 °C/min under nitrogen flow at 20 ml/min.

3.6 Preparation of collagen functionalized PNIPAm electrospun nanofibers

All electrospinning processes were carried out in an acrylic chamber built in-house at the University of Nottingham Malaysia. The set up consists of a syringe pump (NE 300, New Era), a high voltage supply (ES30P-10W/DDPM/SI, Gamma High Voltage) and aluminium foil wrapped around a square acrylic plate (10x10cm). For the co-spinning set up, an additional syringe pump (KDS 210, KD Scientific) and high voltage supply (ESPS-P303) were used. Temperature and relative humidity were recorded at approximately 25-27 °C and 45-

55 %, respectively. Figure 3.3 shows the dedicated electrospinning chamber along with its set up.
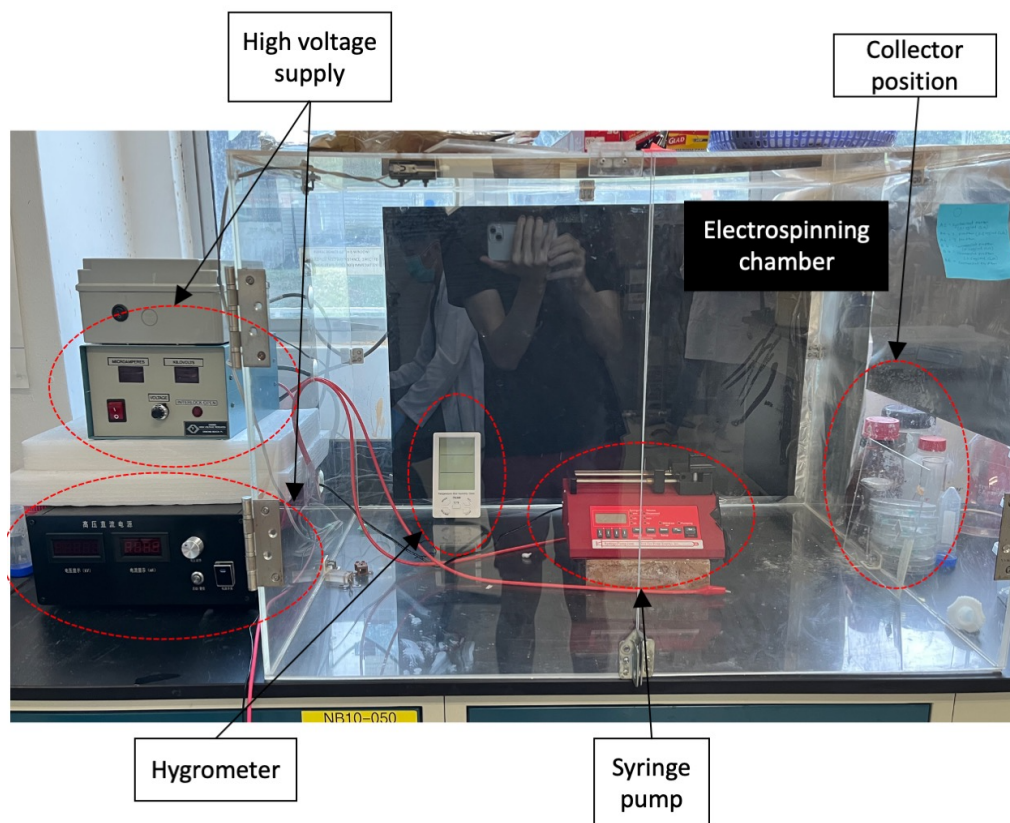
Figure 3.3: Chamber for electrospinning and electrospinning set up.

3.6.1 Preparation of PNIPAm electrospun nanofibers

High molecular weight commercial PNIPAm (300,000 Da) was electrospun according to the established methods by Wang et. al. [11] with slight modifications, as a control to electrospun synthesized PNIPAm. Briefly, 12 % (w/w) commercial PNIPAm solution was prepared with the binary solvent of THF:DMF at a ratio of 1:1.

Electrospinning was carried out at voltage of 13 kV, flow rate 0.6 ml/h and working distance of 17 cm.

With synthesized PNIPAm, preliminary study on electrospinning was conducted on BIS cross-linked PNIPAm (i.e. x-PNIPAm). However, electrospraying was generally observed (further discussions are included in the following results and discussion chapter). Electrosprayed x-PNIPAm was initially compared with electrospun LMW commercial PNIPAm, given the similarity in their viscosities. LMW commercial PNIPAm and x-PNIPAm solutions were both prepared in MeOH at 20 % (w/w) and 4.5 % (w/w), respectively, and were electrospun at similar electrospinning conditions with applied voltage of 19 kV, flow rate 0.5 ml/h and working distance of 18 cm.

The poor electrospinnability of x-PNIPAm motivated the synthesis of cross-linker free PNIPAm (i.e. A100 PNIPAm). However, obtaining straight electrospun nanofibers was not straightforward, and optimisation of electrospinning parameters was required. A study to optimise the electrospinning parameters was conducted with the objective to produce straight nanofibers of A100 PNIPAm. In the study, A100 PNIPAm was electrospun from THF:DMF (1:1) at concentrations of 10 %, 12.5 % and 15 % (w/w), voltage of 9 kV to 15 kV and flow rate of 0.3 ml/h to 0.6 ml/h. Working distance was kept constant at 18 cm. The optimal concentration was found to be 15 % (w/w) A100 PNIPAm in THF:DMF (1:1), voltage of 9 kV, flow

rate 0.6 ml/h and working distance of 18 cm. The higher concentration of synthesized A100 PNIPAm used was due to more consistent electrospun fibers obtained without beads. Table 3.1 summarises the studied parameter for electrospinning A100 PNIPAm.

Table 3.1: Studied solution and electrospinning parameters in electrospinning A100 PNIPAm.

Concentration (% (w/w))	Voltage (kV)	Flow rate (ml/h)	Working distance (cm)
10 to 15	9 to 15	0.3 to 0.6	18 cm

Neat electrospun PNIPAm generally possess poor aqueous stability upon exposure to aqueous media, thus requiring cross-linking. Cross-linker OPEPOSS and catalyst EMI were introduced into the electrospinning solution of commercial PNIPAm and A100 PNIPAm according to the methods established by Wang et. al. at 20 % (w/w) OPEPOSS and 0.3 % (w/w) EMI, both in respect to weight of PNIPAm [11]. Both commercial PNIPAm and A100 PNIPAm were subjected to curing in an oven at 120 °C for 4 hours.

3.6.2 Preparation of collagen functionalized PNIPAm electrospun nanofibers

TFS collagen was prepared in two concentrations of 0.1 % and 0.5 % (w/w) in 0.5 M AA by stirring overnight at 4 °C, and stored at the same temperature until further use. Electrospun PNIPAm were cut into circles of 20 mm with a leather punch and placed in a 24-well culture plate. 0.5 ml of collagen solutions were added to the PNIPAm membranes and left for 1 hour at 4 °C. The solutions were then carefully removed, and the membranes sterilized with 70 % EtOH for 20 minutes followed by three washes with PBS. After the final wash, PBS was removed and the membranes left under UV in a bio-safety cabinet for 15 minutes for further sterilization. Neat electrospun PNIPAm membranes were sterilized similarly, and act as controls for cell culture experiments.

3.7 Characterization of electrospun nanofibers

3.7.1 Polymer solution viscosity analysis

The inherent viscosity of synthesized PNIPAm solution at 15 % (w/w) in THF:DMF (1:1) was measured with a viscometer (Brookfield Viscometer DV-II+ Pro, USA) at shear rates of 0.75, 1.50, 2.25, 3.00, 3.75, 4.50 s^{-1}. The measured shear stress (Pa) against shear rate (s^{-1}) was plotted and the gradient of the straight line gives the viscosity in Pa.s.

3.7.2 Morphological analysis using Field Emission Scanning Electron Microscope

The morphology of electrospun PNIPAm, collagen functionalized (via dip coating) PNIPAm and TFS collagen was observed under a Field Emission Scanning Electron Microscope (FESEM) (FEI Quanta 400 F, USA). Samples were mounted onto dedicated stubs with carbon tapes. Images of electrospun PNIPAm and collagen functionalized PNIPAm were captured under low vacuum mode at an acceleration voltage of 20 kV while images of electrospun TFS collagen were captured under high vacuum mode with an acceleration voltage of 10 kV. High vacuum mode was used to obtain high resolution images of TFS collagen, and due to the non-conductive nature of electrospun PNIPAm, in order to prevent distortion of images due to electron charging on the samples, low vacuum mode was used. The average fiber diameter, pore size and their distributions were analysed based on FESEM images by using ImageJ software (version 1.53), an image analysis software developed by Upper Austria University of Applied Sciences and is free for download at https://imagej.nih.gov/ij/download.html. The average fiber diameter was estimated by taking measurements of 1000 random fibers across the longitudinal direction from random points of the electrospun membrane using the measure function. The average pore size was

estimated by using the analyze particle function taking the maximum Feret's diameters of pores.

3.7.3 Weight Loss Measurement

The aqueous stability of electrospun synthesized PNIPAm was evaluated by the percentage mass loss over time. PNIPAm membrane samples were cut out with a hole puncher and pre-weighted with a microbalance (Mettler Toledo XP6, USA) with a resolution of 0.001 mg, and transferred to 24-well plates containing Glasgow Modified Essential Medium (GMEM) and incubated at 37 °C and 5 % CO_2 (cell culture conditions). Samples were taken out after 1, 2, 3, 5, 7, 14, 21 and 28 days, dried under vacuum of 300 mbar at 40 °C for two days and weighted again. Percentage mass loss was computed with the following equation, and the study was conducted in triplicates (n=3).

$$\% \ mass \ loss = \left(\frac{initial \ mass - final \ mass}{initial \ mass} \right) x \ 100 \ \%$$

………. eq. 3.2

3.7.4 Porosity analysis

The porosity of electrospun synthesized PNIPAm represents the percentage of void space within the bulk and was estimated by using the gravimetric method. Three PNIPAm membranes of approximately

1 x 1 cm were cut out (n=3) with a blade and the actual widths measured, validated and recorded with a vernier calliper by laying the cut out samples flat. The thickness of the membranes were measured under FESEM image at 3 random positions. Measurements were taken with the assumption that the membrane is incompressible and does not expand, and have approximately uniform thickness throughout. The widths and thickness of the membranes allow for computation of the bulk volume of the membranes. Mass of the membranes were measured with a microbalance (Mettler Toledo XP6, USA), and the apparent density of the membranes were computed by the ratio of mass of membranes against bulk volume. The porosity was computed by the following relationship, taking the bulk density of PNIPAm as 1.1 g/cm^3[198].

$$Porosity = 1 - \left(\frac{apparent\ density}{bulk\ density} \right)$$

.... eq. 3.3

3.7.5. Water contact angle analysis

The wettability of electrospun PNIPAm membranes were determined by contact angle analysis. In the investigation, both OPEPOSS cross-linked synthesized and commercial PNIPAm were dip coated with 0.1 and 0.5 mg/ml of collagen solution in 0.5 M AA (as described

previously in section 3.6.2). Table 3.2 summarizes the group studied, and contact angle of each group was investigated for 1, 3, 5 and 7 seconds with averaged measurements from three readings (n=3) for each group and time point. Contact angle below 90 ° indicates hydrophilicity while above 90 ° indicates hydrophobicity[199].

Table 3.2: Summary of studied groups of collagen dip coated PNIPAm.

	Concentration of collagen solution (mg/ml) used		
	0 (neat)	**0.1**	**0.5**
Studied	SP	SP0.1CLG	SP0.5CLG
groups	CP	CP0.1CLG	CP0.5CLG

Note: SP=electrospun neat synthesized PNIPAm, CP=neat commercial PNIPAm, SP0.1CLG =synthesized PNIPAm dip coated with 0.1 mg/ml TFS collagen solution, CP0.1CLG=commercial PNIPAm dip coated with 0.1 mg/ml TFS collagen solution, SP0.5CLG=synthesized PNIPAm dip coated with 0.5 mg/ml TFS collagen, and CP0.5CLG=commercial PNIPAm dip coated with 0.5 mg/ml of TFS collagen.

In the contact angle analysis, a smartphone camera was used to capture video recordings of the water droplet on the surface of the analysed membranes for at least 7 seconds from the moment water was dropped. The line of sight of the camera was kept level with the plane of the glass slide, on which the samples were placed, and the camera held in place with a tripod. 20 µl of distilled water was

dropped with a micropipette, held vertically above the membrane samples. The images of the water droplets were taken from the video recordings and the contact angle was measured using ImageJ software (version 1.53) using the angle tool. Figure 3.4 shows the schematic of the contact angle set up. Figure 3.5 shows a particular example of the analysed imaged for contact angle analysis using ImageJ.
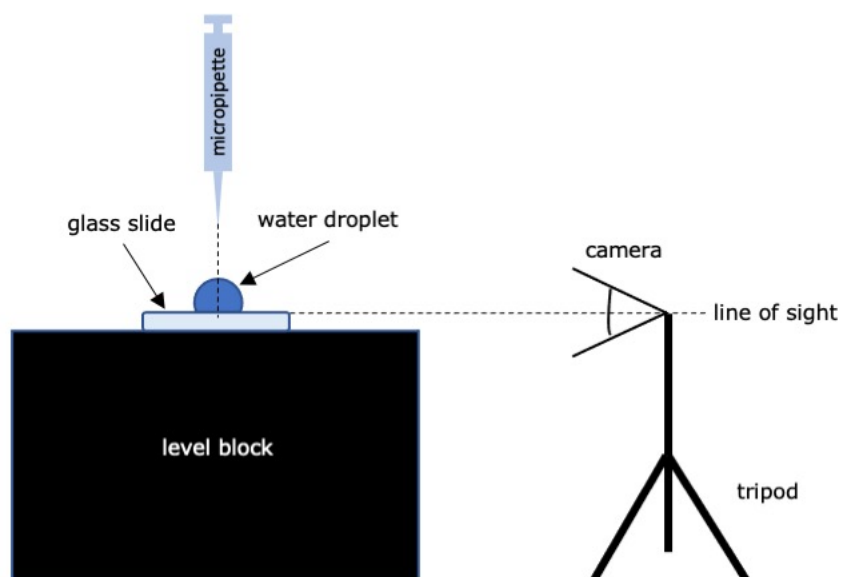
Figure 3.4: Schematic of contact angle set up.
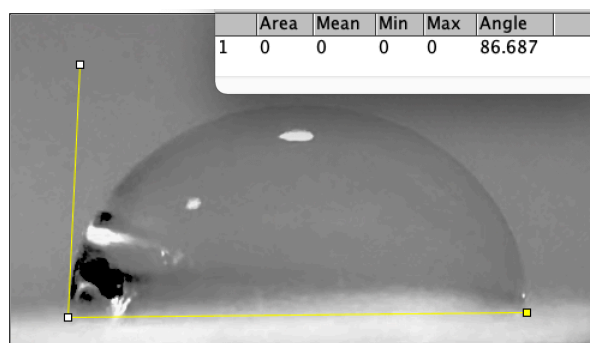
Figure 3.5: Contact angle measurement of a water droplet (1 s) on neat electrospun synthesized PNIPAm giving an angle of 86.7 °.

3.7.6. FTIR analysis of collagen dip coated PNIPAm

FTIR spectroscopy analysis was conducted using Perkin Elmer (Frontier FT-IR/FIR, USA) spectrometer to investigate the functional groups specific to collagen at wavenumber 400-4000 cm^{-1} with 16 scans and 4 cm^{-1} resolution. Samples were dried in an oven at 40 °C for 48 hours prior to analysis.

3.7.7. Thermal degradation analysis using TGA of collagen dip coated PNIPAm

Thermal stability analysis was conducted using the Mettler Toledo (simultaneous TGA/DSC 1, USA) instrument. The analyses were performed in the temperature range of 30 to 500 °C at a heating rate of 10 °C/min under constant nitrogen gas flow of 20 ml/min.

Approximately 5 mg of samples were used for analyses. Samples were dried in an oven at 40 °C for 48 hours prior to analysis.

3.8 Cell culture

Preliminary cell culture studies were conducted using rat amniotic fluid stem cells, also known as R3-AFSC, isolated from full term Sprague Dawley rats. R3-AFSCs were cultured in T25 flasks coated with 0.1 % gelatin at an initial seeding of 750,000 cells beginning from passage 38. All cell culture experiments were conducted under sterile conditions in a biological safety cabinet. All cell culture reagents were pre-warmed in a sterile water bath at 37 °C.

3.8.1 Cell cultivation

A cryovial containing R3-AFSC was first thawed by placing the vial in a 37 °C sterile water bath for 30 seconds. The contents of the cryovial were transferred to a 15-ml centrifuge tube and diluted with 10 ml of ESM. The cells were then centrifuged at 270 x g for 5 minutes to obtain a cell pellet, and the supernatant was discarded. The cells were resuspended in 4 ml of fresh ESM. Concurrently, a T25 flask was coated with gelatin by adding 1 ml of 0.1 % gelatin solution in PBS and left for 5 minutes, and the solution was removed. The resuspended cells were seeded to the coated T25 flask and incubated at 37 °C and 5 % CO_2. After 24 hours, cell attachment was confirmed

under a microscope and incubated for another 24 hours before passaging. Figure 3.6 shows the schematic for cell thawing of R3-AFSC.
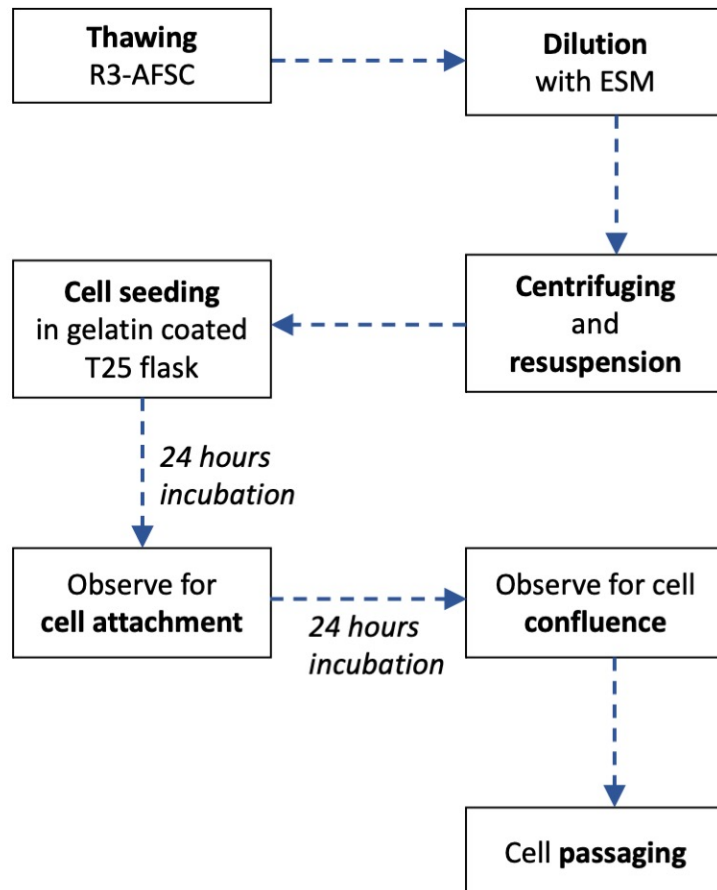
Figure 3.6: Schematic of cell cultivation of R3-AFSC.

Prior to passaging, cells were carefully observed under a microscope for signs of contamination or deterioration. In a biological safety cabinet, the medium was removed and the cells were washed twice with PBS. Approximately 1 ml of 0.25 % trypsin with 1 mM EDTA was added to the flask and the flask was incubated at 37°C for 2 minutes. The flask was then set under a microscope and remaining attached

cells were dislodged by gentle tapping on the sides of the flask. To inactivate the trypsin, 1 ml of pure FBS was added and the cells were dispersed by repeated pipetting, and transferred to a 15 ml centrifuge tube to be centrifuged at 1000 rpm for 5 minutes. Next, the supernatant was removed, and the cells were resuspended in 2 ml of ESM by repeated pipetting. Cells were then counted under the microscope using trypan blue exclusion assay with a haemocytometer. Unstained cells were identified as viable cells and stained cells were identified as non-viable cells, as trypan blue permeates damaged cell membranes. An appropriate volume of the cell suspension containing 750,000 cells was transferred to a new gelatin coated T25 flask, and topped up with ESM to a volume of 4 ml. The seeded flask was left in an incubator for 48 hours at 37 °C and 5 % CO_2 to allow cells to reach confluence. Figure 3.7 shows the schematic of cell passaging of R3-AFSC.

3.8.2 Cell counting

Cell counting was conducted by taking 10 µl of resuspended cells in ESM and mixing with 10 µl of trypan blue by repeated pipetting on a piece of parafilm. Next, 10 µl of the mixture was carefully transferred with a micropipette onto a haemocytometer covered with a glass slide. Cells were counted on the four corner squares on the haemocytometer. The following formula was used to compute the number of cells in the suspension:

$$no.\,of\,cells = \left(\frac{total\,cells\,counted}{4}\right) \times \left(\frac{volume\,of\,suspension}{dilution\,factor}\right) \times 10{,}000$$

………..eq. 3.4

The total cells counted were divided by four to obtain the average of the cell number in the four corner squares.
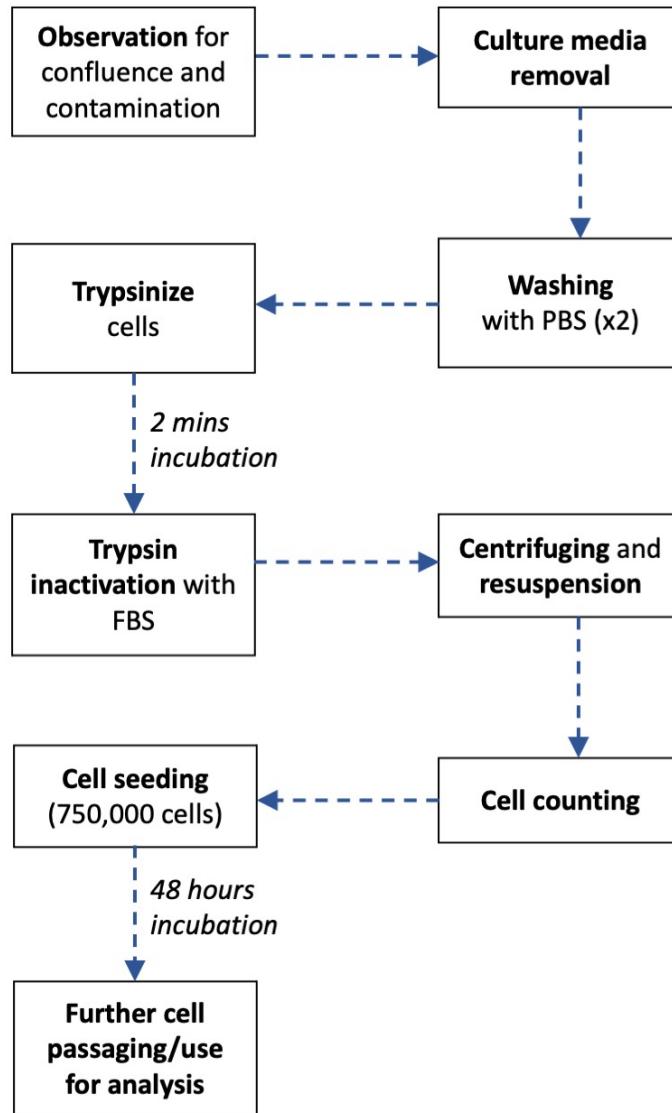
Figure 3.7: Schematic of passaging of R3-AFSC.

3.8.3 Population doubling time

The population doubling time of cells is the time required for a population of cells to double in its amount. It can be estimated by taking the amount of cells at two time points and the duration of culture. The population doubling time was determined by the following formula.

$$Population\ doubling\ time = \frac{duration\ X \log 2}{\log(final\ concentration) - \log(initial\ concentration)}$$

……….eq. 3.5

3.8.4 Cell viability on electrospun scaffolds

The preparation of collagen functionalized electrospun PNIPAm scaffold was described in section 3.6.2. The studied groups of scaffold were similar to the groups summarized in Table 3.1. All scaffolds of 20 mm in diameter were placed in a 48-well plate, designated as shown in Figure 3.8. Gelatin coated wells seeded and not seeded with cells were used as positive and negative controls, respectively.
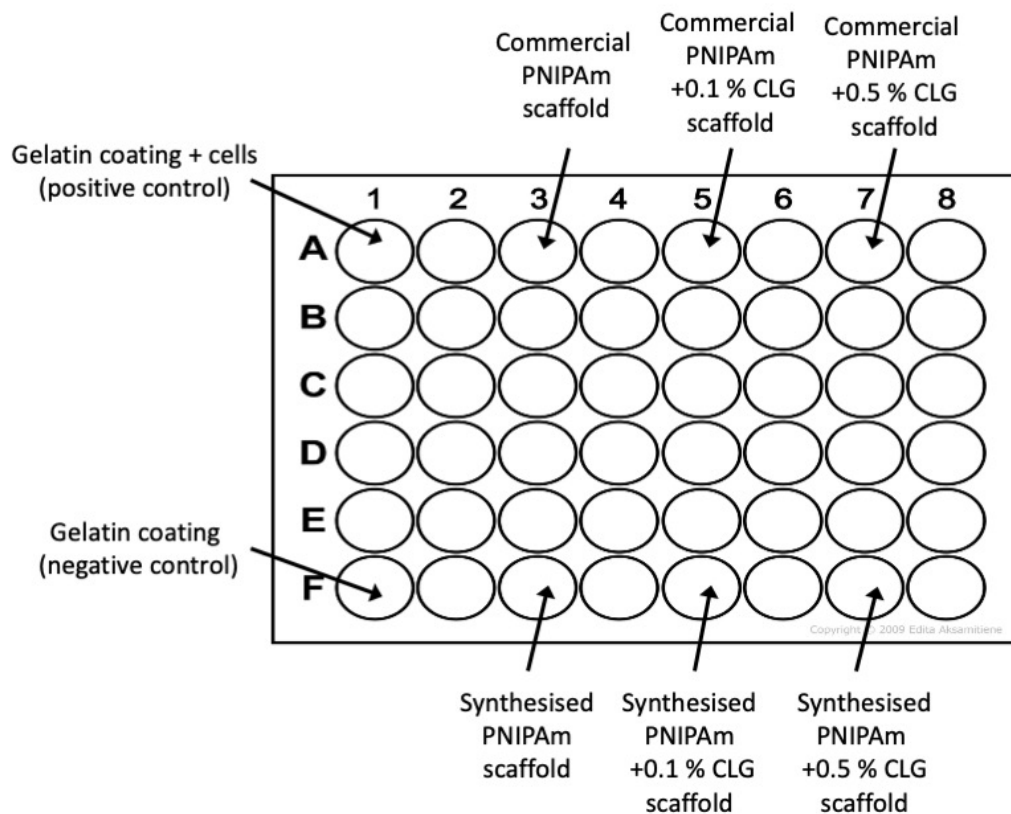
Figure 3.8: Designation of wells in a 48-well plate for cell viability study on electrospun scaffolds.

A stock suspension of cells was prepared at a cell concentration of 300,000 cells/ml. Briefly, cells were counted using a haemocytometer and 600,000 cells were dispersed in 2 ml of ESM. Approximately 0.1 ml of the stock suspension (30,000 cells) was added to the positive controls and each well containing a scaffold. The 48-well plate containing cells and scaffolds was left in an incubator for 1 hour at 37 °C and 5 % CO_2 to facilitate cell attachment, and 0.3 ml of ESM was added to each well to bring the total volume of media to 0.4 ml/well and the plate was incubated for 48 hours.

MTT assay was used to evaluate the cell viability of R3-AFSC on the electrospun scaffolds. MTT solution was prepared at 5 mg/ml in PBS and dissolved by vortexing. The solution was filter sterilized with a syringe filter of 0.22 µm pore size. About 50 µl of MTT solution was added to each well and left to incubate for 4 hours. After 4 hours, 150 µl of DMSO was added to each well to dissolve formed formazan crystals. The culture plate was wrapped with aluminium foil and shaken on an orbital shaker for 15 minutes at 50 rpm. The resulting solution from each well was transferred to a 96-well plate at 0.1 ml volumes and the absorbance at 590 nm was read with a microplate reader (Versa Max microplate reader, USA). Three biological repeats (n=3) were conducted for this study. Cell viability (CV) was evaluated with the following relationship by using the absorbance (Abs) reading:

$$CV\ \% \ = \frac{Abs(seeded\ scaffold) - Abs(negative\ control)}{Abs(positive\ control) - Abs(negative\ control)}\ x\ 100\ \%$$

……….eq. 3.6

3.8.5 Cell release study

Cell seeding onto similar study group of scaffolds was conducted similarly as described in section 3.8.4. The well designation on the

48-well plates were similar to those shown in Figure 3.8. However, incubation duration in this study was 12 hours instead of 48 hours. This first 48-well plate was labelled plate A.

To facilitate cell release, 0.4 ml of ESM at room temperature was added to respective wells in a new 48-well plate (plate B), according to the designation of the plate containing scaffolds. With a pair of forceps, the scaffolds were transferred to the new plate and allowed to sit for 5 minutes to facilitate cell release. Another 48-well plate (plate C) was prepared with 0.4 ml of warm ESM at 37 °C in each well, with similar well designation. After 5 minutes, scaffolds were again transferred to the new plate C containing warm ESM.

After removal of scaffolds, plate A or the seeding plate would contain cells unattached to the scaffolds. Plate B would contain cells that are released from the scaffold after 5 minutes in room temperature ESM and plate C would contain cells that are still attached to the scaffolds after 5 minutes in room temperature ESM.

MTT assay was conducted similarly as described in section 3.8.4 on plates A, B and C.

Fraction of cell released was determined by taking the absorbance at 590 nm of plate B (cells released from scaffold) against absorbance of plate B+C (total cells on scaffold before release). The percentage of cell released was determined by the following formula:

$$\% \ cell \ released = \frac{abs(plate\ B)}{abs(plate\ B) + abs(plate\ C)} \times 100\ \%$$

..........eq. 3.7

Chapter 4

RESULTS AND DISCUSSION

4.1 Analysis on Synthesised PNIPAm

4.1.1 FTIR analysis

PNIPAm hydrogel was synthesized (detailed in section 3.2.2) with the motivation to produce aqueous stable PNIPAm nanofibers by electrospinning. Figure 4.1 shows the FTIR spectra of PNIPAm hydrogel cross-linked with 2 % (w/w) BIS to NIPAm monomer. The peak at 2984 cm^{-1} was assigned to the isopropyl–CH$_3$ asymmetric stretching, while 2937 cm^{-1} belongs to asymmetric –CH$_2$ backbone stretching. The peaks at 1563 and 1632 cm^{-1} were respectively assigned to amide II (-CN) and amide I (C=O). In addition, the peak at 1464 cm^{-1} was assigned to the asymmetric deformation of isopropyl–CH$_3$ vibration and the peak at 1389 cm^{-1} was assigned to the symmetric deformation of isopropyl –CH$_3$. The peaks correspond well to the functional group of PNIPAm as reported in literature [200]. The broad peak at 3334 cm^{-1} belongs to the –OH vibration of water molecules, as a result of hydrated state of the sample [201].
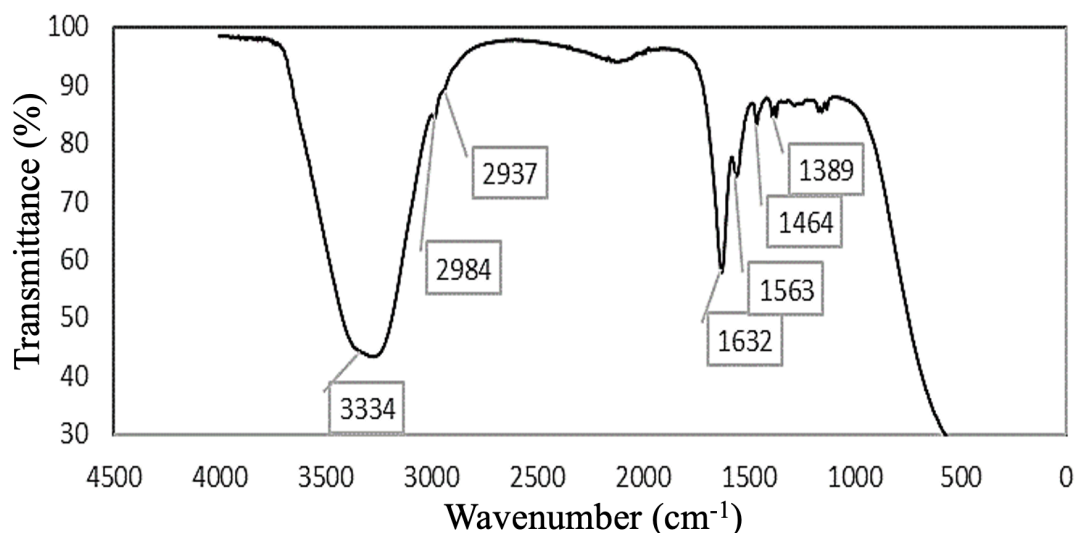
Figure 4.1: FTIR spectra of synthesized BIS-cross-linked PNIPAm hydrogel.

However, the resulting hydrogel shows poor electrospinnability, attributable to its cross-linked nature. This led to further investigation in synthesizing cross-linker free PNIPAm, which exhibits greatly improved electrospinability, and subsequent method to cross-link PNIPAm nanofibers with OPEPOSS after electrospinning to ensure its aqueous stability. OPEPOSS was chosen as the cross-linker because of its solubility in the binary solvent (THF:DMF (1:1)) used for electrospinning, which helps ensure a uniform dispersion of OPEPOSS in PNIPAm during the preparation of PNIPAm electrospinning solution.

4.1.1.1 Effect of agitation rate on the polymerization of NIPAm

Cross-linker free PNIPAm was synthesized via radical polymerization in the presence of surfactant. The agitation rate plays an important role in polymerization employing the use of surfactants (e.g., emulsion polymerization). Studies have been conducted on the effects of agitation rate on the kinetics, molecular weight and molecular weight distribution of hydrophobic monomers suspended in aqueous phase[202], [203]. However, the NIPAm monomer is relatively hydrophilic, and the effects of agitation rate on its polymerization have been scarcely or has not been reported. The formation of reaction sites within the aqueous phase is dissimilar between hydrophobic and hydrophilic monomers. For hydrophobic monomers, surfactant molecules readily attach to the surface of monomer droplets forming micelles, where free radicals derived from the initiator diffuse into micelles to initiate the polymerization and form the reaction sites. As for hydrophilic monomers (e.g., NIPAm), micelles start forming after the initiation by free radicals where increasingly hydrophobic oligomers attract surfactant molecules to spontaneously attach, forming the reaction sites[204]. Figure 4.2(a) shows the micelle formation in the typical oil-in-water emulsion polymerization with hydrophobic monomers and Figure 4.2(b) shows the micelle formation of hydrophilic monomer in water.
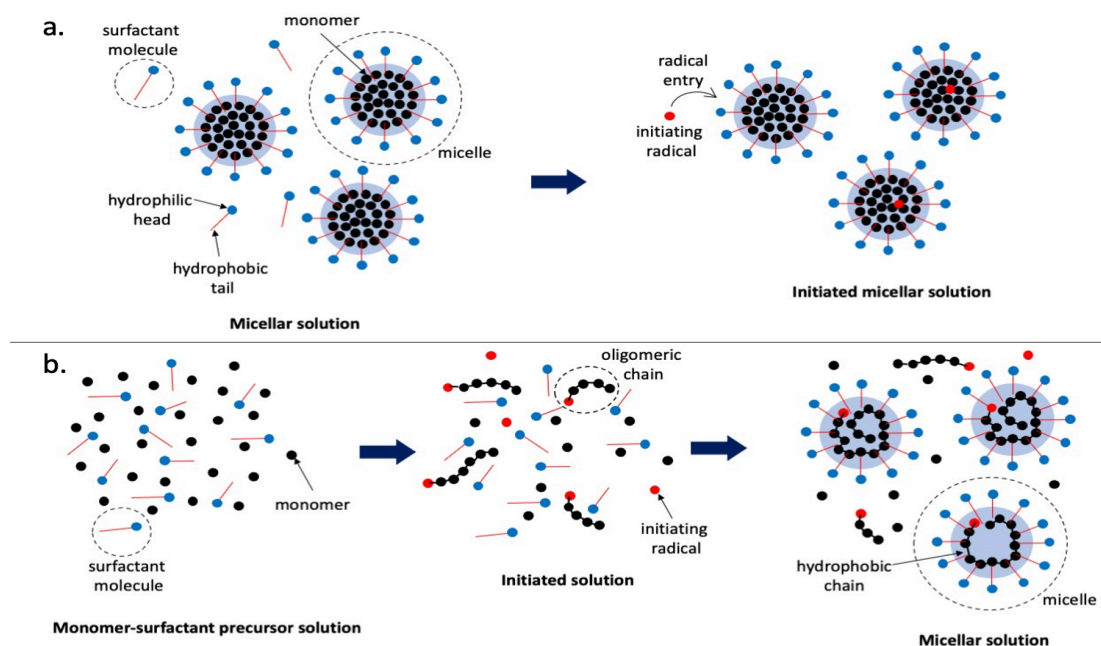
Figure 4.2: (a) micelle formation of typical oil-in water (hydrophobic monomer) emulsion and, (b) micelle formation of hydrophilic monomer in water.

The size of micelles formed and its size distribution for polymerization of hydrophilic monomers is predominantly determined by the shearing rate within the reaction bulk. It has been reported that the emulsion polymerization kinetics of the hydrophobic monomer styrene is dependent of the agitation rate during preparation of the emulsion, and becomes independent of agitation rate during polymerization. This was attributed to the stable dispersion of the emulsion formed prior to polymerization[205]. In this part of the study, the dependence of agitation rate used in polymerization of NIPAm in the presence of SDS surfactant by employing three

agitation speeds of 50, 100 and 200 rpm during preparation and polymerization is discussed in terms of final properties of the polymer and monomer to polymer conversion. Primary free radicals were generated from the decomposition of the thermal initiator KPS. Hereafter, preparation and polymerization of NIPAm at agitation speeds of 50, 100 and 200 rpm are referred to as A50, A100 and A200, respectively.

Figure 4.3 shows the FTIR spectra for recrystallized NIPAm monomer, commercially available PNIPAm, A200, A100 and A50. In the A50 and A100 spectra, the peak at 1619 cm^{-1} which signified characteristic of C=C (indicated by vertical dashed line) stretching is not seen, confirming point of polymerization on the vinyl group. A new broader peak appears at 1635 cm^{-1} for the A50 and A100 samples which belongs to characteristic of the amide I (C=O) stretching. Both A50 and A100 spectra show characteristic peaks of the polymer at 1388 cm^{-1}, 1531 cm^{-1}, 2876 cm^{-1}, 2968 cm^{-1}, and 3284 cm^{-1} which can be assigned to symmetrical deformation of (–CH_3) bend, amide II (C–N) stretch, symmetric (–CH_3) vibration, asymmetric (–CH_3) vibration and stretching of the NH group, respectively[200]. The peak at 1616 cm^{-1} of the pre-dialyzed A200 sample, signature to C=C stretching characteristic of the monomer NIPAm suggests the low conversion of monomer to polymer. Lastly, the A50 and A100 samples show similar peaks with commercial PNIPAm further confirming PNIPAm was

successfully synthesized. Pre-dialyzed sample of A200 was used due to loss of materials after dialysis, which can be attributed to the low monomer-polymer conversion resulting in mostly low molecular weight PNIPAm (below the cut-off size of dialysis sacks of 12 kDa).
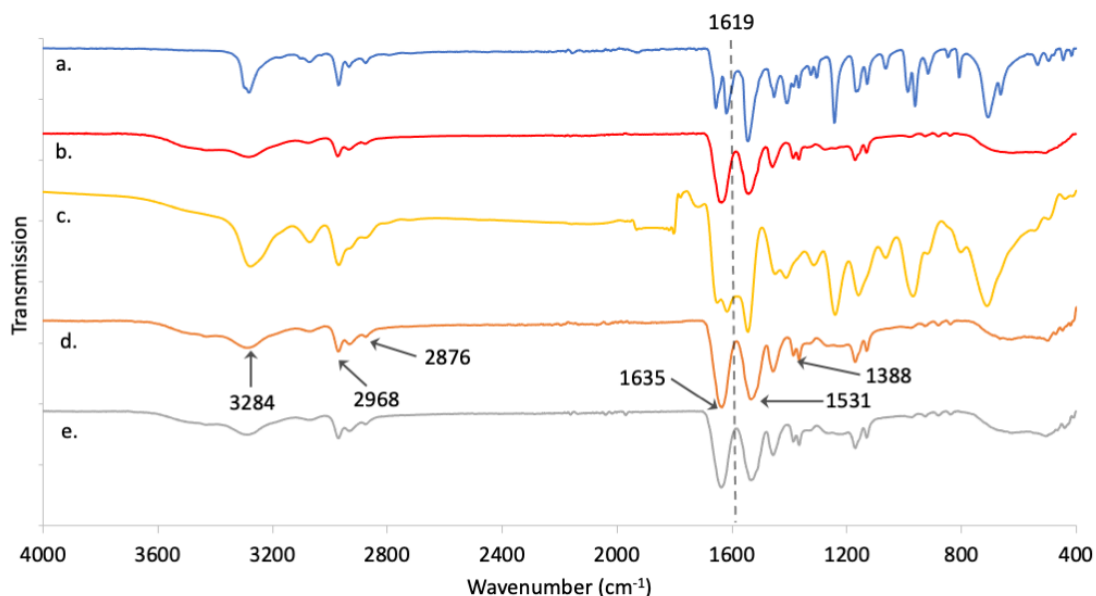
Figure 4.3: FTIR spectra of (a) recrystallized NIPAm, (b) commercial PNIPAm, (c) A200 (pre-dialyzed), (d) A100, (e) A50.

Since the synthesis temperature of 80 °C was well above the LCST of PNIPAm, the turbidity of the final solution after 4 hours of synthesis could provide a visual indication of the conversion of NIPAm to PNIPAm, where the phase separation of PNIPAm from water above ~32 °C would lead to the increase in solution cloudiness. It is worth noting that all runs started off with clear solutions. Both A50 and A100 solutions were cloudy after 4 hours, while A200 remained clear. This further suggests the conversion of NIPAm to PNIPAm in the A50

and A100 runs, and relatively low conversion in the A200 run. Table 4.1 summarizes the solution turbidity before and after polymerization of A50, A100 and A200.

Table 4.1: Summary of solution turbidity before and after (4 hours) polymerization at 80 °C.

Polymerization run	Initial solution turbidity (80 °C)	Final solution turbidity (4 hours at 80 °C)
A50	Clear	Cloudy
A100	Clear	Cloudy
A200	Clear	Clear

Consistent with other work, it has been reported that an increase in agitation intensity causes an increase in inhibition to the rate of emulsion polymerization [5, 8]. Although the reason has not been widely studied, there were reports stating that the efficiency of the free radicals derived from the initiator is dependent on the critical size of the reaction site, affecting the rate of radical entry, where a high agitation intensity results in the formation of small reaction sites insufficient to facilitate efficient radical entry [206]. Given the low monomer-polymer conversion of A200, indicated by FTIR and final solution turbidity, further analyses were conducted only on A50 and A100 PNIPAm.

4.1.2 Molecular weight analysis using static light scattering

The molecular weight of PNIPAm was determined using Zetasizer static light scattering (SLS). The refractive index increment (dn/dc) of both A50 and A100 PNIPAm in MeOH was computed to be 0.2021 ml/g, as shown by the gradient of the straight line of refractive index against concentration in Figure 4.4.
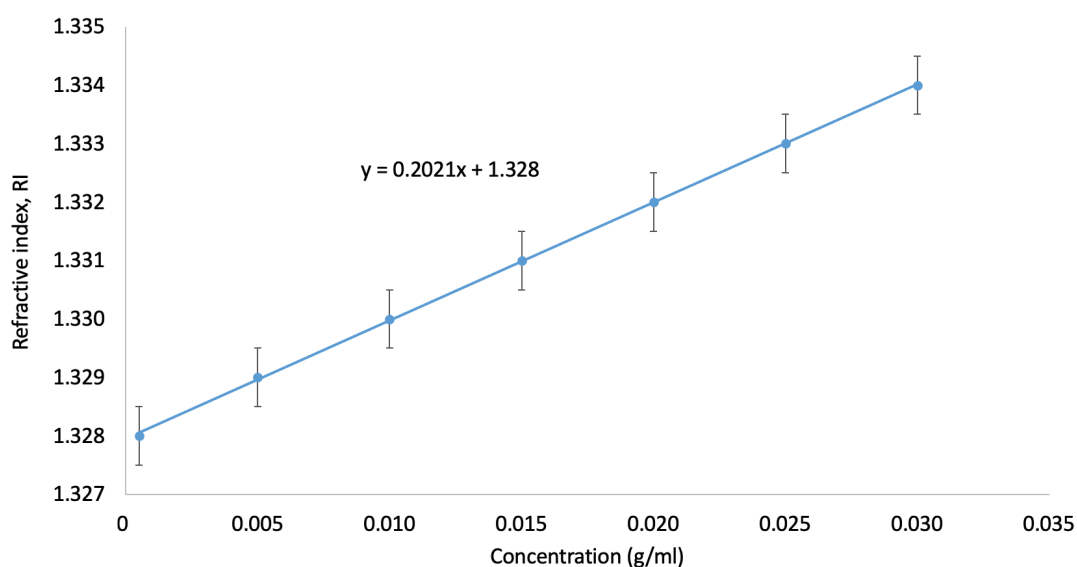
Figure 4.4: Plot of refractive index against concentration of A50 and A100 PNIPAm in MeOH. A50 and A100 PNIPAm both show similar increase in refractive index with increase in concentration.

Figure 4.5 shows the resulting Debye plot. As mentioned in section 3.3.2, the Debye plot is given by Kc/R against concentration of solute and the inverse of the y-intercept of the Debye plot gives the molecular weight of a polymer. K, c and R represents the Debye constant, concentration of solute and Rayleigh ratio (ratio of

scattered light to incident light of the sample), respectively. Altogether, the expression Kc/R represents the intensity of scattered light. The linear Rayleigh equation is presented as follows, where the terms A_2 and M_w are the second virial coefficient and molecular weight, respectively. From the equation, as concentration becomes zero, Kc/R equals $1/M_w$, which as mentioned earlier, makes the y-intercept the inverse of molecular weight. The second virial coefficient, A_2 indicates the particle interaction strength and is correlated to solubility of sample [207]. A_2 can be computed from dividing the gradient of the Debye plot by 2 (since $2A_2$=gradient). Both A50 and A100 gives a negative value of A_2 of -0.0034567 ml/gDa and -0.0004067 ml/gDa. The larger A_2 value of A50 PNIPAm indicates that its particles have higher interaction strength than A100 PNIPAm particles, suggesting that A50 PNIPAm particles have a higher tendency for agglomeration.

$$\frac{Kc}{R} = 2A_2 c + \frac{1}{M_w} \ [207] \qquad\qquad ……….eq. \ 4.1$$

The molecular weight of A50 and A100 PNIPAm were computed from the Debye plot to be 223 kDa and 381 kDa, respectively. The correlation coefficient, r, was used as a measure of spread of plot points of intensity of scattered light (Kc/R) against concentration of solute. The Debye plot of A50 PNIPAm gives a correlation coefficient

of -0.8131 while A100 PNIPAm gives -0.9818, which indicates that the intensity of scattered light of A50 PNIPAm has a relatively lower correlation with concentration of solute, as compared with A100 PNIPAm. The relatively higher spread in A50 as compared to A100 could be attributed to its higher tendency for particle agglomeration, resulting in more largely distributed particle size. Similarly, the low spread in A100's Debye plot could be attributed to the lower tendency for particle agglomeration, resulting in less dispersed particle size. These are further discussed in section 4.1.3 in terms of particle size distribution.
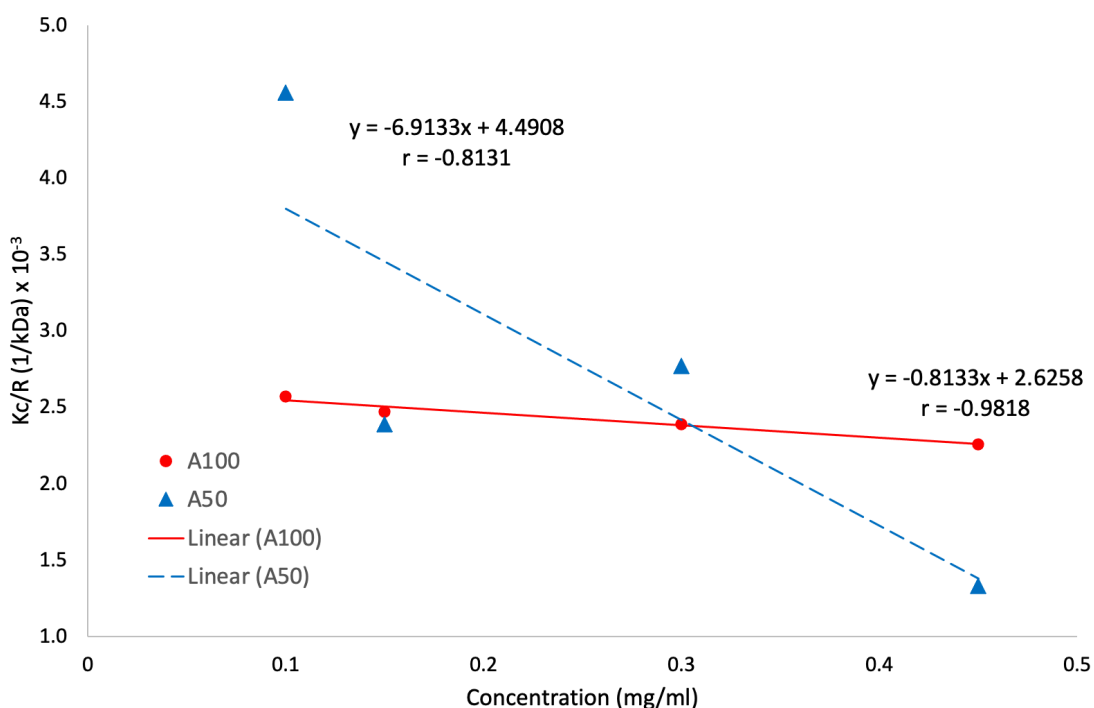
Figure 4.5: The Debye plot of A50 and A100 PNIPAm. K=Debye constant, c= concentration of solute and R=Rayleigh's constant. r represents the correlation coefficient.

4.1.3 Particle size distribution analysis using dynamic light scattering

Figure 4.6 shows the particle size and distribution of A50 and A100 PNIPAm samples as characterized using static light scattering analysis of the Zetasizer. The A50 particles were distributed over a relatively broad range between 20 nm to 1300 nm, with a PDI of 0.535. A100 yielded particles distributed over a narrower range of 140 nm to 520 nm and PDI of 0.090. The higher PDI of A50 as compared to A100 corroborates the higher tendency for agglomeration of A50, forming a more polydispersed system than A100, as discussed in section 4.1.2. The computed average hydrodynamic diameter (i.e., average particle size) values were 153.4 nm and 250.5 nm for A50 and A100 PNIPAm samples, respectively.
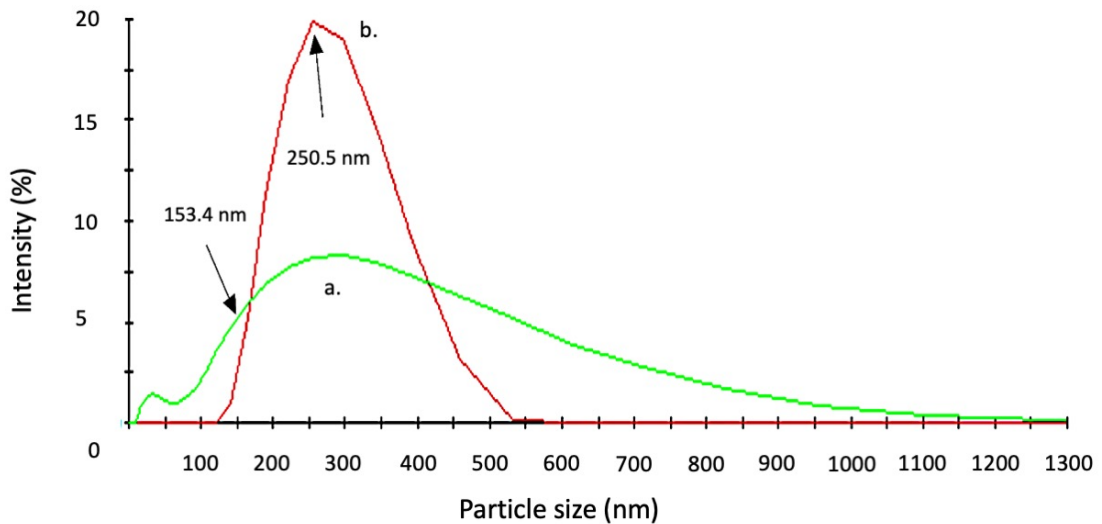
Figure 4.6: Particle size and particle size distribution of A50 and A100 PNIPAm. (a) A50, (b) A100.

The PDI can range from a value of 0 to 1, measuring the spread of particle size distribution with values below 0.1 indicating monodispersed particles and above 0.1 signifying polydispersed particles [208]. The computation of PDI is presented as follows:

$$PDI = \left(\frac{\sigma}{d}\right)^2 \quad [208] \qquad \ldots\ldots\ldots\text{eq. 4.2}$$

In the equation, σ and d represent the standard deviation and average particle diameter, respectively. Table 4.2 shows the computed standard deviation corresponding to the average particle size and PDI of A50 and A100 PNIPAm.

Table 4.2: Summary of average particle size, PDI and corresponding standard deviation of A50 and A100 PNIPAm.

	Average particle size (nm)	PDI	Standard deviation (nm)
A50 PNIPAm	153.4	0.535	112.20
A100 PNIPAm	250.5	0.090	75.15

The lower computed average hydrodynamic diameter value for the A50 PNIPAm was due to a broader distribution of particle size in relative to A100 PNIPAm. The average hydrodynamic diameter values fitted within the range of particle size predicted for polymers synthesized via emulsion polymerization of 10 nm to 1 μm [209]. The broad range of the A50 PNIPAm particle size was ascribed to the low agitation speed during polymerization contributing to a poor dispersion of monomer droplets that act as supply reservoirs of monomer to the reaction sites (i.e., oligomers and growing polymer particles). The growth of the polymer particles is a diffusion-controlled process. As monomers are consumed within the reaction sites, monomer droplets in the aqueous phase act as the supply reservoir allowing diffusion of monomers from the aqueous phase into the reaction sites through a concentration gradient of the monomer. The growth of the polymer depends on the competition between the polymerization rate and the diffusion rate of monomers in the

reaction sites. At the start of polymerization, large monomer droplets within the aqueous phase slow down the diffusion rate of monomers into the reaction sites, where polymerization rate surpasses the diffusion rate. Therefore, relatively smaller particles are formed. As the reaction progresses, the large monomer droplets start becoming smaller as monomers are consumed, subsequently increasing the diffusion rate of monomer until the rate of diffusion equals the rate of polymerization. The time taken for this equilibrium to occur contributes to the formation of particles of various sizes. In a system of well dispersed monomer droplets as in the case of A100, the equilibrium between reaction rate and diffusion rate can be achieved quicker, thus forming a more narrow size distribution of final polymer particles due to a more steady rate of growth of polymer particles[210]. Figure 4.7 shows the schematic demonstrating the effect of monomer dispersion on the monomer diffusion and subsequent growth of polymer particles. In the initial stage of polymerization, the poor dispersion of monomer due to insufficient agitation led to relatively limited monomer diffusion into polymer particles, forming polymer particles in a broad range of sizes (Figure 4.7 (a)), while rate of monomer diffusion gradually increases as monomer are consumed in the monomer reservoir. Uniform particle growth can be achieved when monomers are well dispersed from the initial polymerization stage (Figure 4.7 (b)). Additionally, at agitation speed of 200 rpm during polymerization, the low monomer to

116

polymer conversion could be a result of the inhibition in formation of stable reaction sites at high shear. Short chain oligomeric particles were postulated to not have achieved sufficient hydrophobicity for spontaneous attachment of surfactant to form micellar reaction sites.
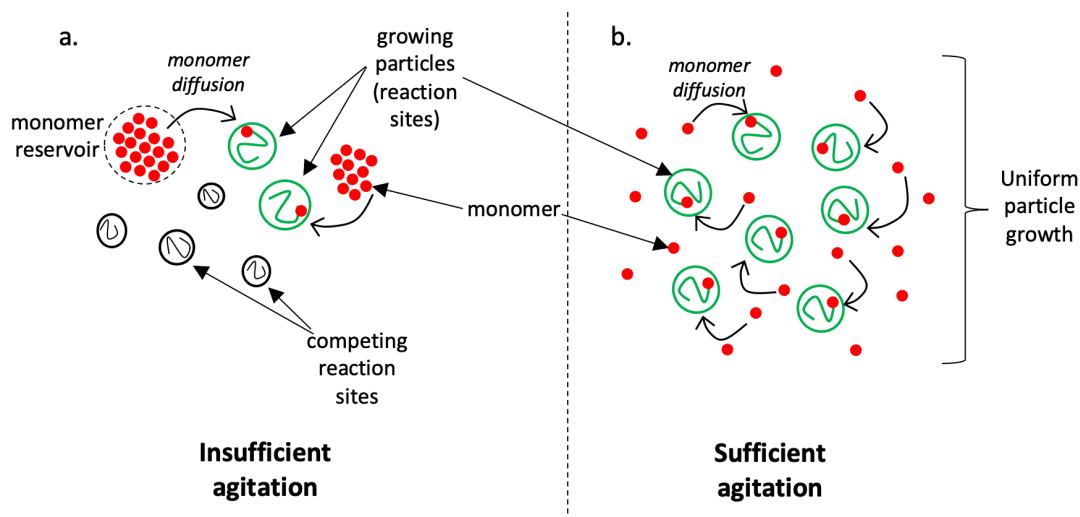
Figure 4.7: Schematic of (a) diffusion of monomer from agglomerated monomer (monomer reservoir) into growing polymer particles across the aqueous phase, and (b) diffusion of well dispersed monomer across the aqueous phase into growing polymer particles.

4.1.4 Thermo-responsive phase transition test

The thermally induced phase transition of the synthesized PNIPAm (A50 and A100) is shown in Figure 4.8. At 25˚C, below its LCST, A50 and A100 PNIPAm dissolved in ddH$_2$O appear to be relatively clear where PNIPAm and water form a homogenous phase. At 40˚C, these

solutions become turbid due to the precipitation of PNIPAm from water [211]. This shows that the synthesized PNIPAm exhibit its characteristic thermo-responsive behaviour. Figure 4.9 shows the schematic of the coil-to-globule transition of PNIPAm molecules across its LCST in water. Below its LCST, PNIPAm chains associate with water molecules and appear in its coiled state, giving a clear solution. Above its LCST, PNIPAm chains self-associate forming a globular state and expelling surrounding water, forming a cloudy solution.
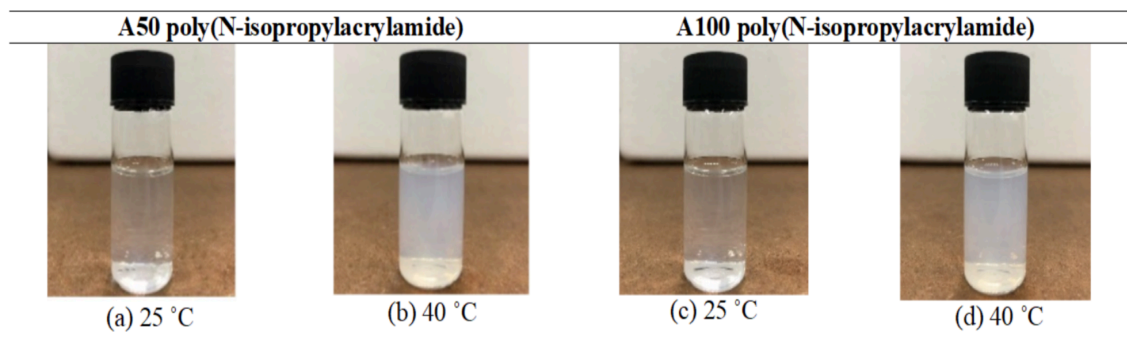
Figure 4.8: Visual representation of synthesized PNIPAm exhibiting phase transition across its LCST. (a) A50 PNIPAm at 25°C, (b) A50 PNIPAm at 40°C, (c) A100 PNIPAm at 25°C, (d) A100 PNIPAm at 40°C.
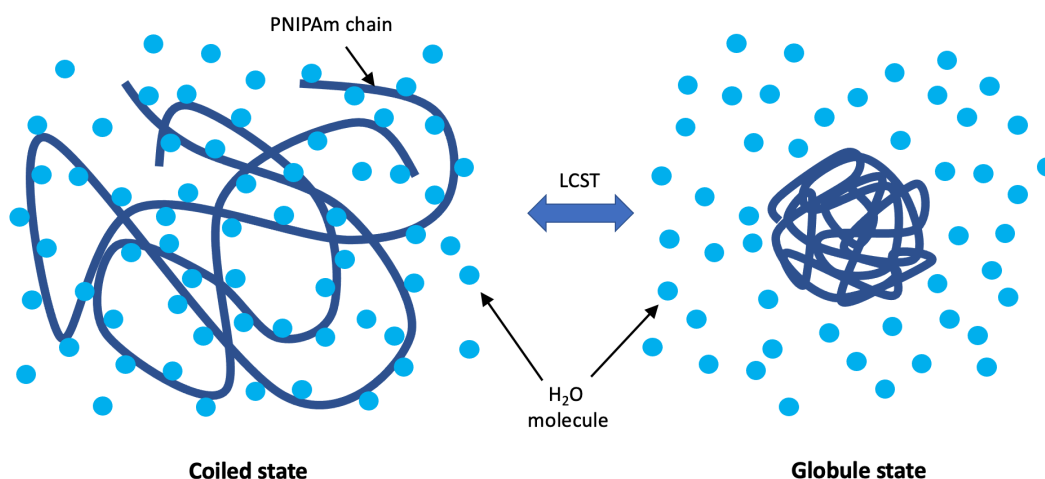
Figure 4.9: Coil-to-globule transition of PNIPAm chains in water.

4.1.5 Thermal analysis using TGA

The TGA and differential thermal gravimetry (DTG) curves of A50 and A100 PNIPAm are shown in Figure 4.10(a) and 4.10(b), respectively. For A50 PNIPAm, a minor weight drops of about 0.6 % from 30°C to 100°C is attributed to the residual water within the PNIPAm sample. The major weight loss depression of approximately 88% was observed from 330°C through 430°C, with the maximum rate of weight loss at 400°C. Similar features were observed for A100 PNIPAm where a minor weight loss of approximately 1 % was observed from 30°C to 100°C, a major weight loss of about 92% from 330°C through to 430°C, and maximum rate of weight loss at 400°C. The minor weight losses from both curves are due to loss of residual water bounded to PNIPAm samples, while the major weight losses indicate the degradation of main chain of PNIPAm backbone.

The main chain degradation occurs at the range of temperature (345°C to 450 °C) as reported by Ribeiro C. A. et. al. [212]. A slight increase in weight initially at about 31 °C can be attributed to the buoyancy effect of the inert nitrogen gas flow caused by heating, leading to a minute reduction in density of gas, consequently causing the weight balance to register an increase in weight[213].
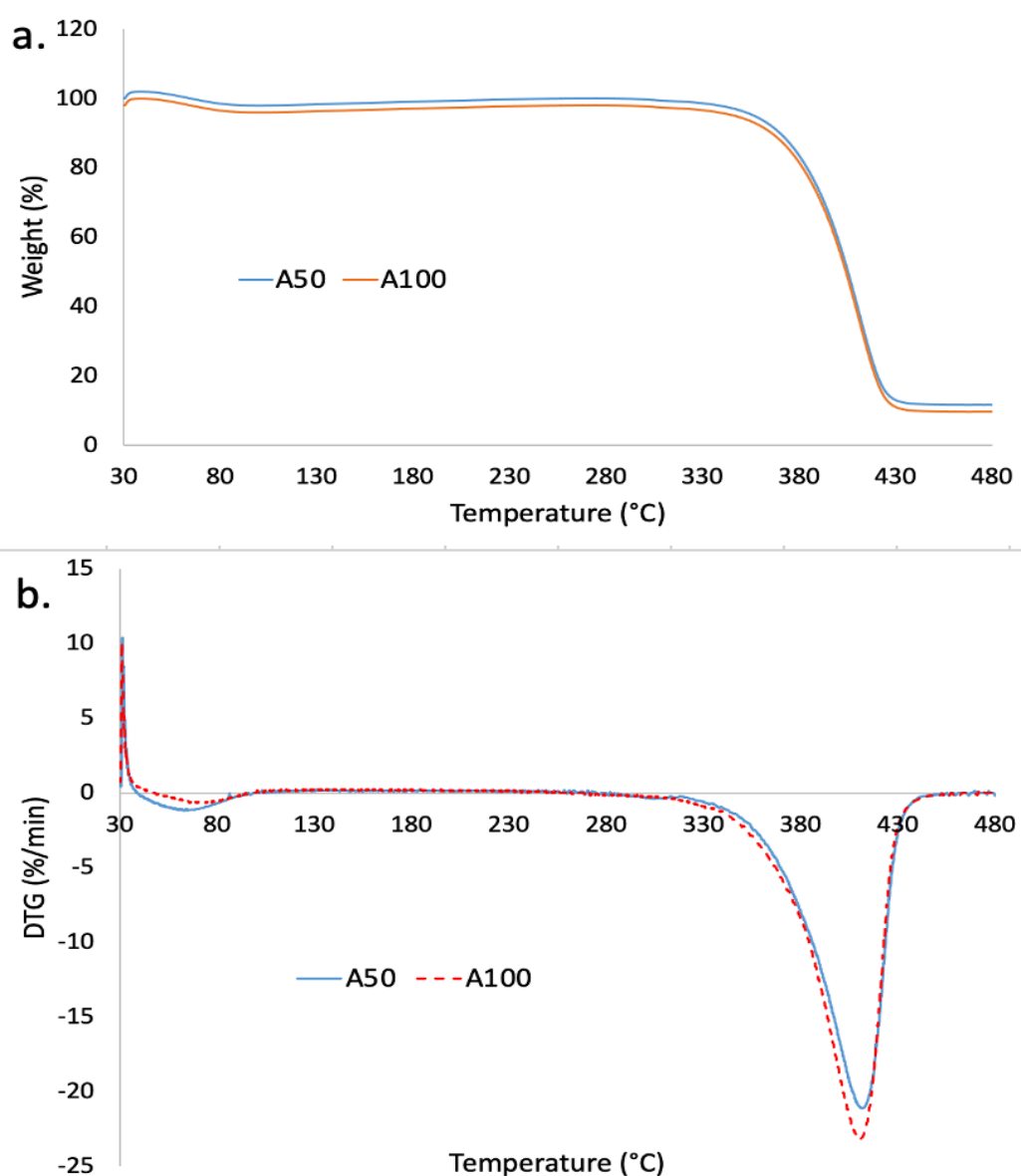
Figure 4.10: (a) TGA and (b) DTG curve of A50 and A100 PNIPAm.

4.1.6 The effect of cross-linking density on the physiochemical properties of PNIPAm

Without cross-linking, PNIPAm is water soluble below and phase separates above its LCST[5], [44], [48], [214]. However, hydrogels or pre-crosslinked PNIPAm has been reported to exhibit poor electrospinnability due to its insoluble nature [11]. Preliminary attempt to electrospin 4 % (w/w) synthesized PNIPAm cross-linked with low amount of BIS (2 % (w/w)) in respect to NIPAm monomer) in MeOH yielded mostly electrosprayed beads as shown in Figure 4.11(a). This was compared to electrospun 20 % (w/w) low molecular weight (Mw= 40,000 g/mol) commercial linear PNIPAm in MeOH which yielded nanofibers, as shown in Figure 4.11(b). It should be noted that both electrospinning solutions exhibited similar viscosities of 28.6 (BIS cross-linked PNIPAm) and 28.1 cP (low molecular weight commercial PNIPAm). The poor electrospinnability of cross-linked PNIPAm can be attributed to its chemical cross-linkage withholding against continuous fiber stretching towards the direction of the collector. Figure 4.12(a) shows the mechanism of chain disentanglement of linear polymer chains when subjected to shear and Figure 4.12(b) shows the resistance to chain disentanglement of cross-linked polymer during electrospinning.
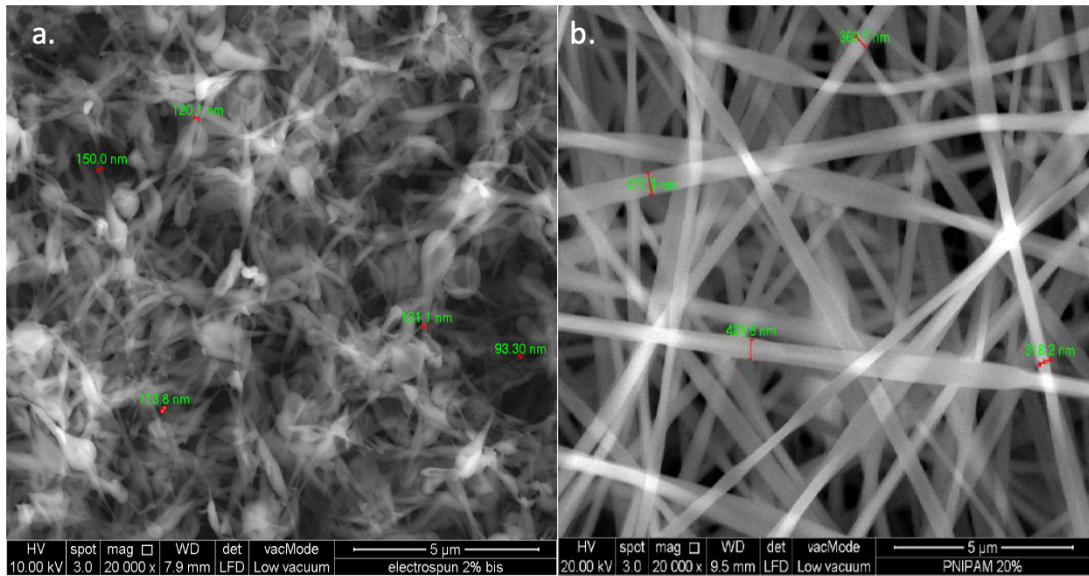
Figure 4.11: FESEM images of electrosprayed/electrospun PNIPAm from (a) 4 % (w/w) cross-linked PNIPAm with 2 % (w/w) BIS and (b) 20 % (w/w) of low molecular weight commercial linear PNIPAm, both dissolved in MeOH.
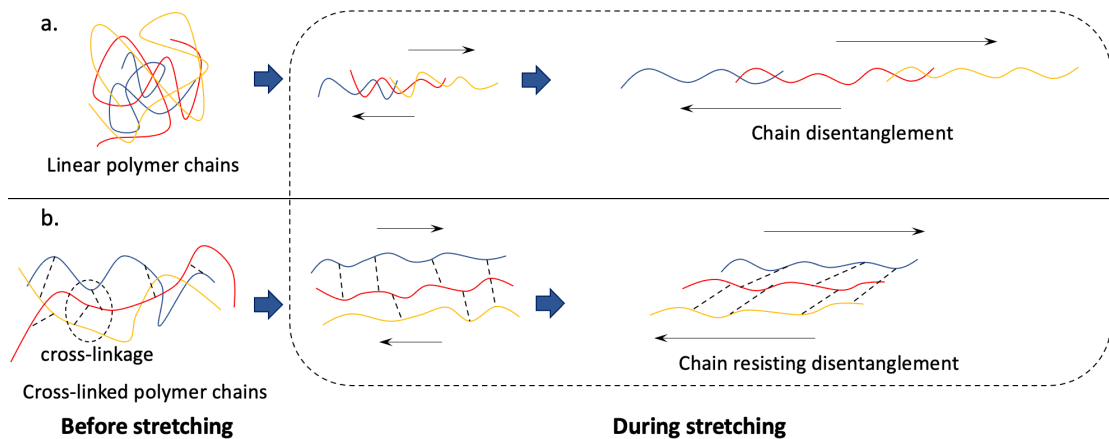
Figure 4.12: (a) chain disentanglement of linear polymer chains during electrospinning and, (b) resistance to chain disentanglement of cross-linked polymer during electrospinning.

4.1.7 Rheological analysis of synthesized PNIPAm

The apparent viscosities of the A50 and A100 samples were compared at a concentration of 12 % (w/w) in MeOH (section 3.3.7) as a representation of their respective rheological behavior. Figure 4.13 shows the plot of shear stress against shear rate of A50 and A100 PNIPAm and the gradients of the straight lines represent their viscosities. The low viscosity of 0.0165 Pa·s (0.17 poise) of A50 PNIPAm can be attributed to the relatively broader distribution of PNIPAm particle size as compared to A100. Vice versa for the relatively higher viscosity of 0.1799 Pa·s (1.80 poise) of A100 can be attributed to its narrow particle size distribution. This is in agreement as reported in literature where a more polydispersed system contributes to a lower viscosity[215]. The viscosity is also a function of chain entanglement between polymer chains, where higher chain entanglement would lead to higher viscosity. In turn, an average higher molecular weight leads to greater chain entanglement in polymer systems. The higher viscosity of A100 as compared to A50 can be corroborated by their higher and lower average molecular weights, respectively, as discussed in section 4.1.2. Sufficient chain entanglement is crucial for the electrospinnability of a polymer[216]. The higher viscosity of A100 PNIPAm suggest its better potential for electrospinning into nanofibers. According to N. Amariei et. al. , as a general rule of thumb, a solution with viscosity of 1-20 poise is a

suitable solution for electrospinning[217]. Therefore, further analysis was conducted on A100, and interchangeably referred to as synthesized PNIPAm.
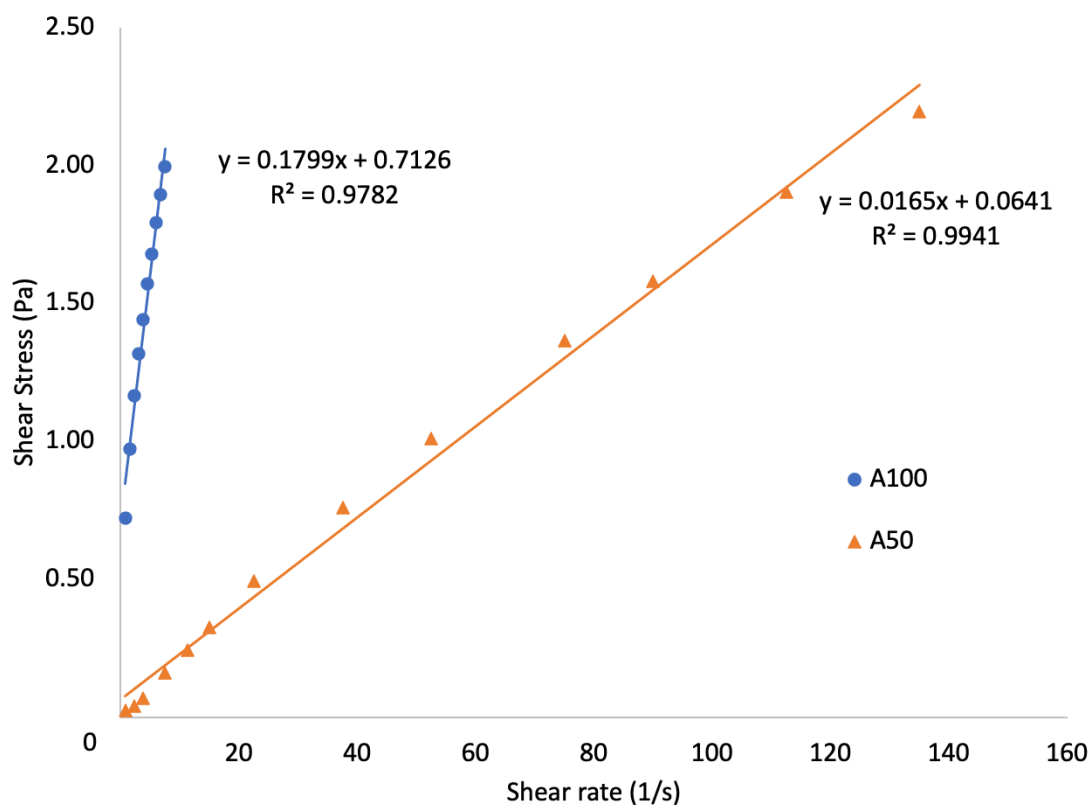
Figure 4.13: Plot of shear stress against shear rate of A50 and A100 PNIPAm. The gradients of the straight lines give the viscosities (i.e., A50=0.0165 Pa.s and A100=0.1799 Pa.s).

4.2 Isolation of Collagen from Tilapia Fish Scales

4.2.1 Functional group analysis

The FTIR spectra of type I collagen as extracted from tilapia fish scales is shown in Figure 4.14, and the peaks are in conformance

with type I collagen sourced from freshwater fishes. Characteristic peaks at wavenumbers 1634 and 1550 cm^{-1} are assigned to amide I (C=O) stretching and amide II (-NH) bending, respectively. The transmission ratio of amide III at 1238 cm^{-1} and amide II (-CH) bending vibration at 1450 cm^{-1} indicates the integrity of collagen triple helical structure where the calculated value was 0.977 indicative of intact triple helical structure[218]. The computation is presented as follows, with the transmission values for wavenumbers 1238 and 1450 cm^{-1} being 72.26 and 73.94 %, respectively as indicated in Figure 4.14

$$Ratio\ of\ \%\ transmission = \frac{72.26}{73.94} = 0.977$$

……….eq. 4.3

Further, the amide A band associated with the -NH free stretching occurs at wavelengths of 3400-3440 cm^{-1}. The amide A band for the extracted collagen occurs at 3303 cm^{-1}, where a shift to lower frequency occurred, indicative of -NH groups participating in hydrogen bonding forming a more ordered structure. Lastly, the Amide B peak appears at 3079 cm^{-1} and its assigned to the CH$_2$ stretching vibration [219].
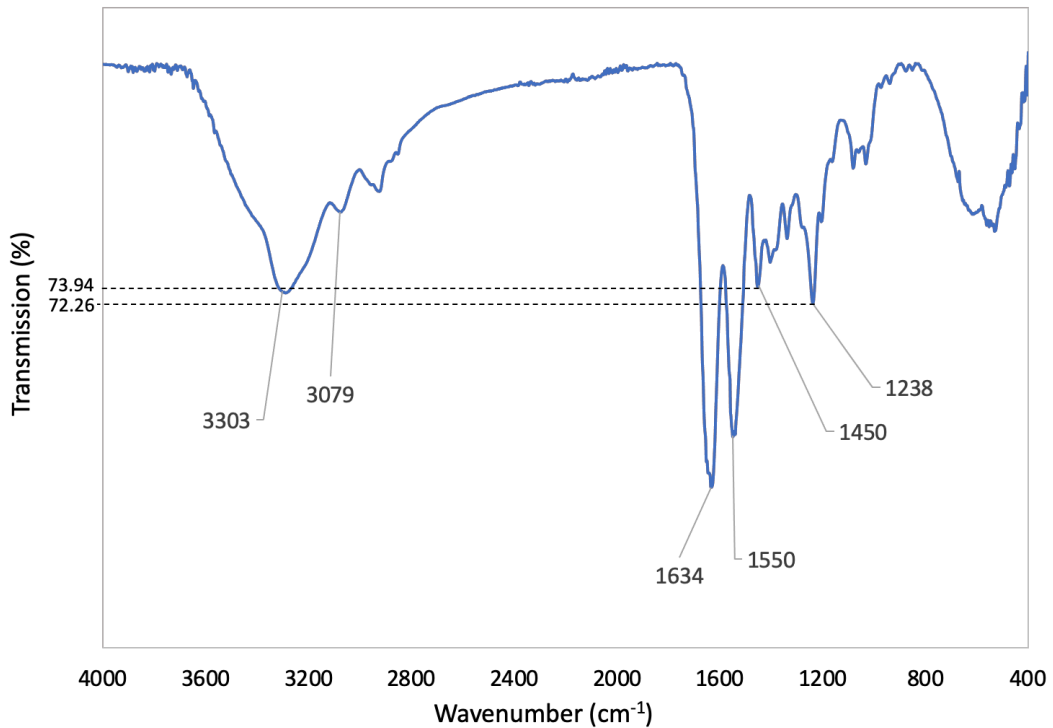
Figure 4.14: FTIR spectra of collagen extracted from Tilapia fish scales.

4.2.2 Thermal properties of fish scale derived collagen

Figure 4.15 shows the DSC curve for collagen extracted from Tilapia fish scales with two endothermic peaks at 85.48 and 155.2 °C. The first peak at 85.48°C could be attributed to the denaturation of collagen from its fibrillar and triple helical structure into random coils of α–chains by breakage of intra- and inter-molecular hydrogen bonds and release of loosely bound water. The second endothermic peak at 155.2°C can be attributed to the degradation of polypeptide α–chains and evaporation of residual strongly bound water. The denaturation temperature of dry extracted collagen is in close

agreement reported in other literature on other fish collagen films by R.M.T. Fernandes et al. of 65.9, 70.9 and 74.9 °C for collagen samples prepared from swim bladders of *Pescada Amarela*, *Gurijuba* and *Pescada Branca* fishes, respectively [220]. On collagen extracted from carp fish skin as reported by Safandowska M. et. al., the denaturation temperature was assigned at 77 °C (in agreement with this work and R.M.T. Fernandes et. al.) while a second peak at 120 °C was assigned to further conformational changes of triple helix and destruction of material[221]. There is a contradiction in DSC thermal peak assignment between this work and Safandowska M. et. al. in the temperature range of 100 to 200 °C.

Figure 4.16 shows the TGA curve for collagen extracted from Tilapia fish scales along with a DTG plot to indicate inflexion points in the TGA curve. Approximately 40 % of mass loss occur in the temperature range of 230 to 370 °C, which can be attributed to the destruction of material (as opposed to 120 °C reported by Safandowska M. et. al.). The slight increase in weight at 34 °C can be attributed to the buoyancy effect of nitrogen gas flow during heating, leading to a small reduction in gas density, consequently causing the weight balance to register an increase in weight[213]. Nevertheless, denaturation temperature of collagen is related to the hydroxyproline content, habitat of fish, collagen level of hydration and collagen extraction methods. In general, collagen in its dry state

is found to have higher thermal stability in terms of maintaining its triple helical structure than collagen in solutions [222].
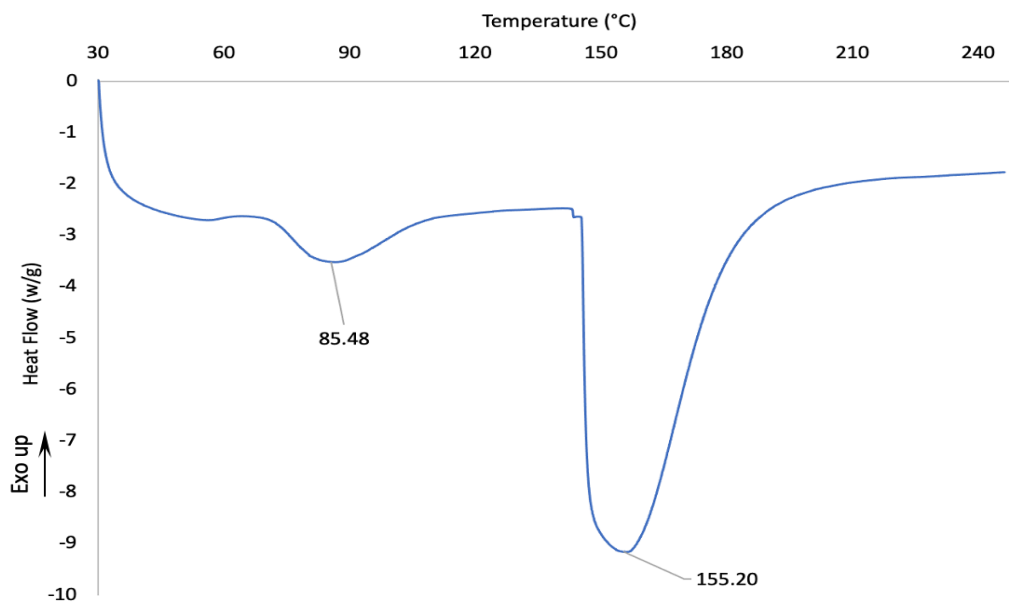
Figure 4.15: DSC curve of collagen extracted from Tilapia fish scales.
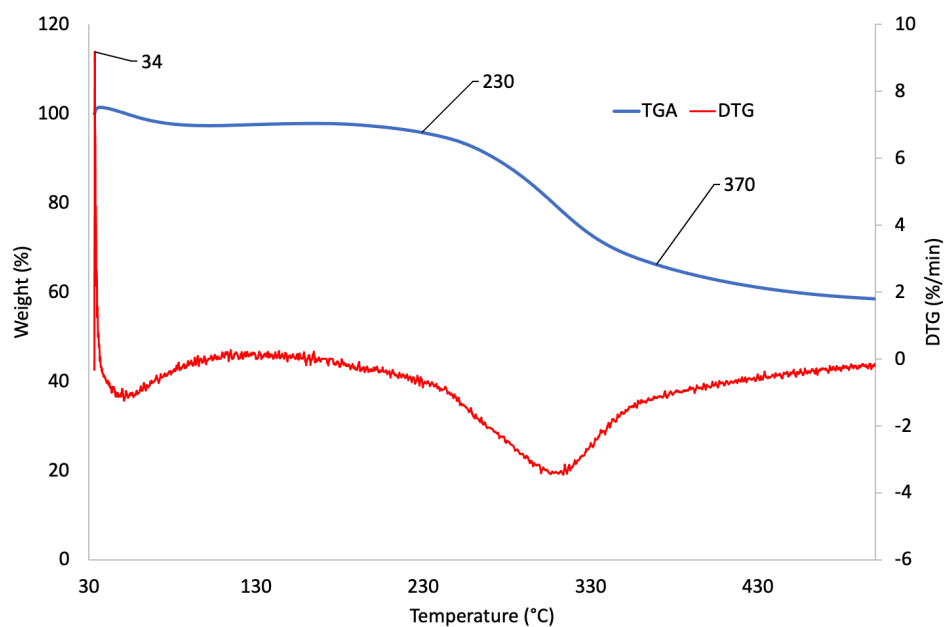
Figure 4.16: TGA and DTG curve of collagen extracted from tilapia fish scales.

4.2.3 Molecular weight

Figure 4.17 depicts the acrylamide gel image upon completion of SDS-PAGE. It was found that the extracted collagen comprises two α-chains (α_1 and α_2), with estimated molecular weight in the range of 120 - 150 kDa corroborating collagen type I. The relative band intensity of α_1 was approximately double that of the α_2, indicating that the extracted collagen could be deduced as $(\alpha_1)_2\alpha_2$ [223]. The high band intensity at approximately 250 kDa showed that the acid soluble collagen contained high population of cross-linked β (dimer) structure composed of inter and intra molecular crosslinks dimerized by the α-chains [219].
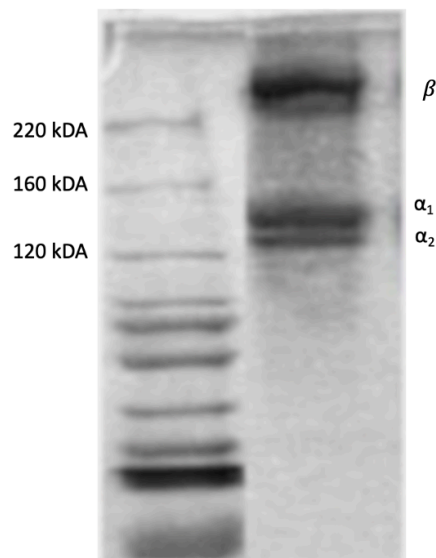
Figure 4.17: Image of acrylamide gel after SDS-PAGE. Molecular weight marker (left) and extracted tilapia fish scale collagen (right).

4.3 Optimization of PNIPAm electrospun nanofibers

Electrospinning of synthesized PNIPAm into nanofibers was investigated as described by the methods in section 3.6.1. Fiber size are reported by mean ± standard deviation. Briefly, synthesized PNIPAm was dissolved in THF:DMF (1:1) at 10, 12.5 and 15 % (w/w) concentrations. Figure 4.18 shows the FESEM images of resulting electrospun synthesized PNIPAm. At 10 % (w/w), electrospinning was conducted at applied voltage of 15 kV and flow rate of 0.3 ml/h which yielded some nanofibers with beads on strings morphology (Figure 4.18(a)). Working distance was kept constant at 18 cm throughout the electrospinning investigation. The production of high amount of beads and inconsistent fibers were attributed to insufficient PNIPAm chain entanglement to maintain a stable electrospinning jet. To improve chain entanglement, concentration of synthesized PNIPAm was increased to 12.5 % (w/w), with applied voltage of 9 kV and flow rate of 0.3 ml/h. Significantly improved morphology was observed in terms of formation of straight and continuous nanofibers. However, beads on string morphology was still observed (Figure 4.18(b)). Further increase in concentration to 15 % (w/w) yielded straight PNIPAm nanofibers without beads, as shown in Figure 4.18(c). At this concentration, synthesized PNIPAm was electrospun at applied voltage of 9 kV and flow rate of 0.6 ml/h. The significant improvement in nanofiber morphology with increment

in PNIPAm concentration indicates that concentration plays a significant role in formation of nanofibers during PNIPAm electrospinning.
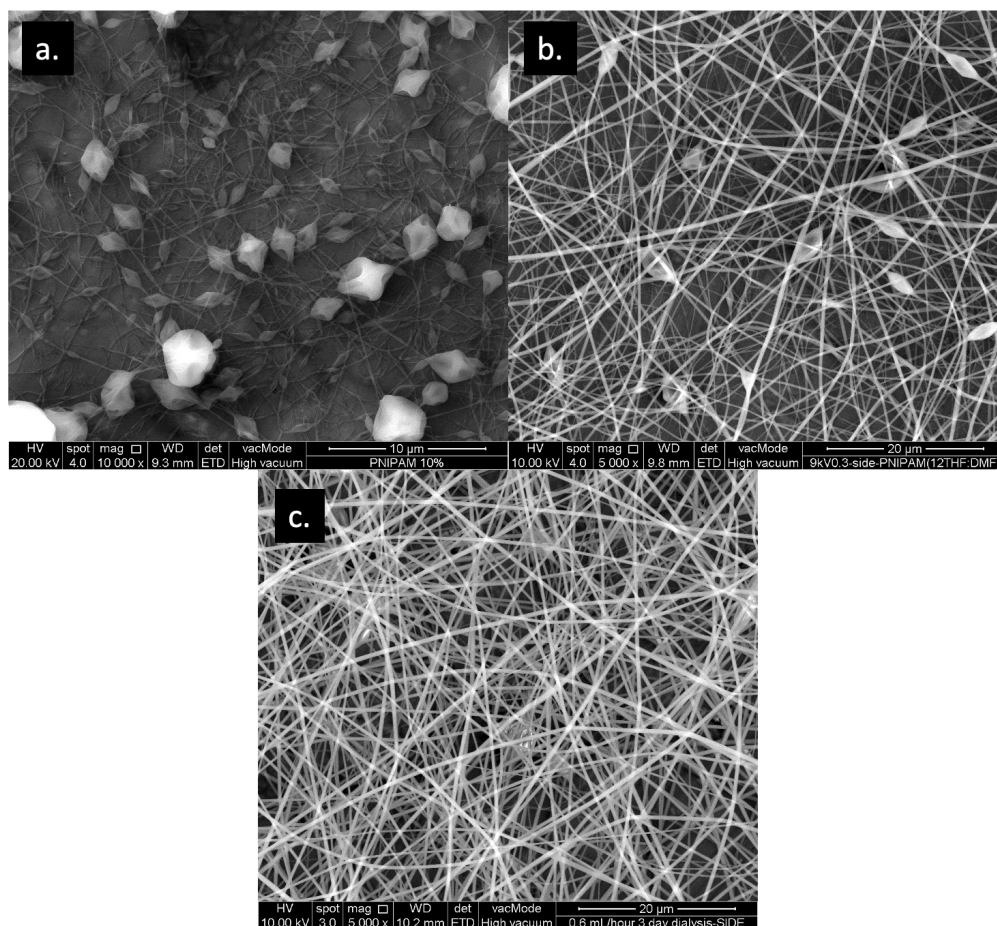
Figure 4.18: Electrospun synthesized PNIPAm from THF:DMF (1:1) at concentrations of (a) 10 % (w/w), (b) 12.5 % (w/w) and (c) 15 % (w/w).

Since 15 % (w/w) of synthesized PNIPAm in THF:DMF (1:1) shows good potential in yielding beadless and straight nanofibers, further investigation was conducted to study the effect of applied voltage and

flow rate at this concentration. Figure 4.19 shows the FESEM images of electrospun PNIPAm at 15 % (w/w) concentration in THF:DMF (1:1) with a combination of applied voltages (i.e., 9 and 15 kV) and flow rates (i.e., 0.3 and 0.6 ml/h). Straight nanofibers without beads were observed at every voltage-flow rate combination. Figure 4.20 shows the corresponding fiber diameter distribution of electrospun synthesized PNIPAm at similar investigated voltage-flow rate combinations. The fiber diameter at 9 kV and 0.3 ml/h was 325.05 ± 115.76 nm. The measurement methodology is highlighted in section 3.7.2. An increase in flow rate to 0.6 ml/h resulted in a slight increase fiber diameter (335.02 ± 114.89 nm). This was expected as the increase in flow rate increases the amount of PNIPAm ejected from the spinneret tip. Increase in applied voltage from 9 kV to 15 kV at flow rate of 0.3 ml/h yielded fiber with increased diameter of 388.98 ± 183.58 nm. A similar increase in fiber diameter was observed at flow rate of 0.6 ml/h and 15 kV. The increase in fiber diameter at both flow rates with the increase of applied voltage (from 9 to 15 kV) was due to increased acceleration of PNIPAm jets towards the collector. PNIPAm jets at 15 kV were pushed through the electric field quicker than at 9 kV, resulting in reduced whipping and stretching of jets.

Additionally, one-way analysis of variance (ANOVA) analysis coupled by Tukey's post-hoc test was conducted to verify significant

differences in the mean of fiber diameters from all four voltage-flow rate combinations at significance level of $p < 0.05$. No significant difference was found between electrospun synthesized PNIPAm at 9 kV-0.3 ml/h and 9 kV-0.6 ml/h. Similarly, no significant difference was found between electrospun PNIPAm at 15 kV-0.3 ml/h and 15 kV-0.6 ml/h. These suggest that flow rate during electrospinning of synthesized PNIPAm does not significantly affect the size of nanofibers formed. However, an increase in voltage from 9 to 15 kV at both flow rates resulted in significant difference between their means. This suggests that the applied voltage plays a more significant role in determining the final size of synthesized PNIPAm nanofibers. Nevertheless, it is noteworthy to mention that at these voltage-flow rate combinations, nanofibers of PNIPAm in the range of 200 to 900 nm were effectively fabricated. Further work was conducted on electrospun synthesized PNIPAm at concentration of 15 % (w/w) in THF:DMF (1:1), applied voltage of 9 kV, flow rate of 0.6 ml/h and working distance of 18 cm, given that these conditions produced PNIPAm nanofibers with the lowest spread in fiber diameter as indicated by its standard deviation of 114.89 nm (as mentioned in section 3.6.1).
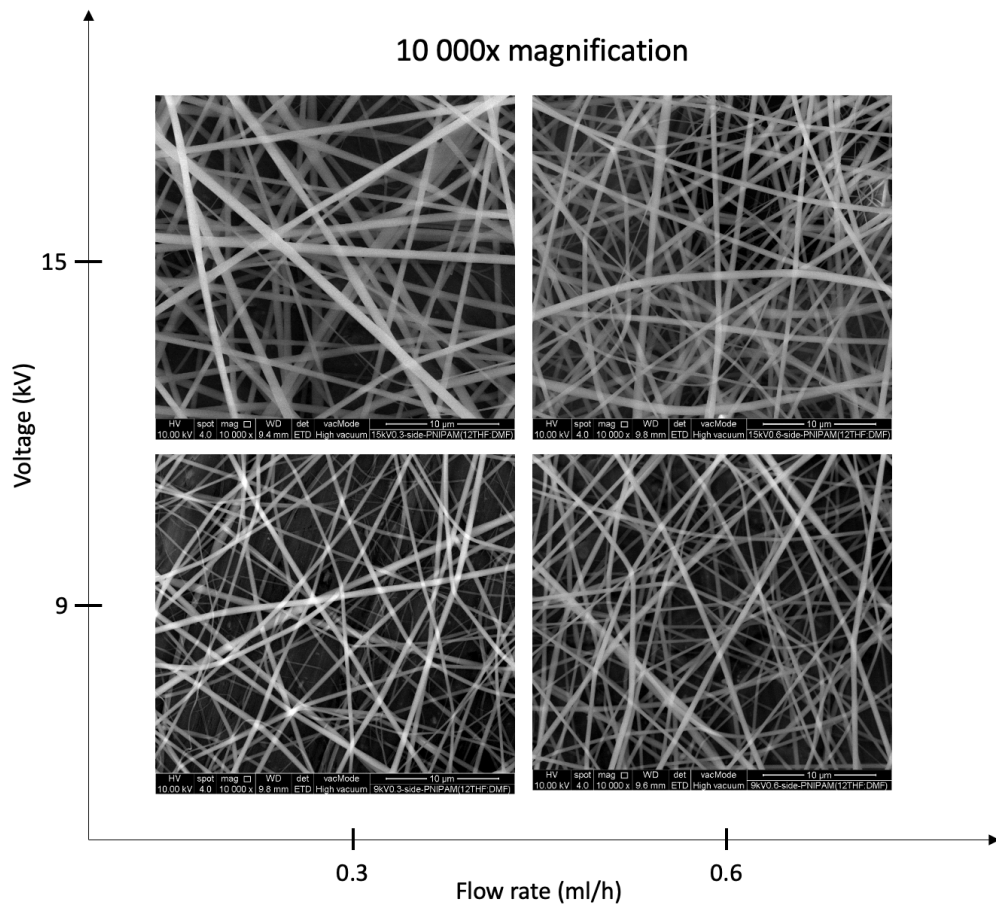
Figure 4.19: Electrospun synthesized PNIPAm from THF:DMF (1:1) at 15 % (w/w) concentration from combinations of applied voltage of 9 and 15 kV, and flow rate 0.3 and 0.6 ml/h.
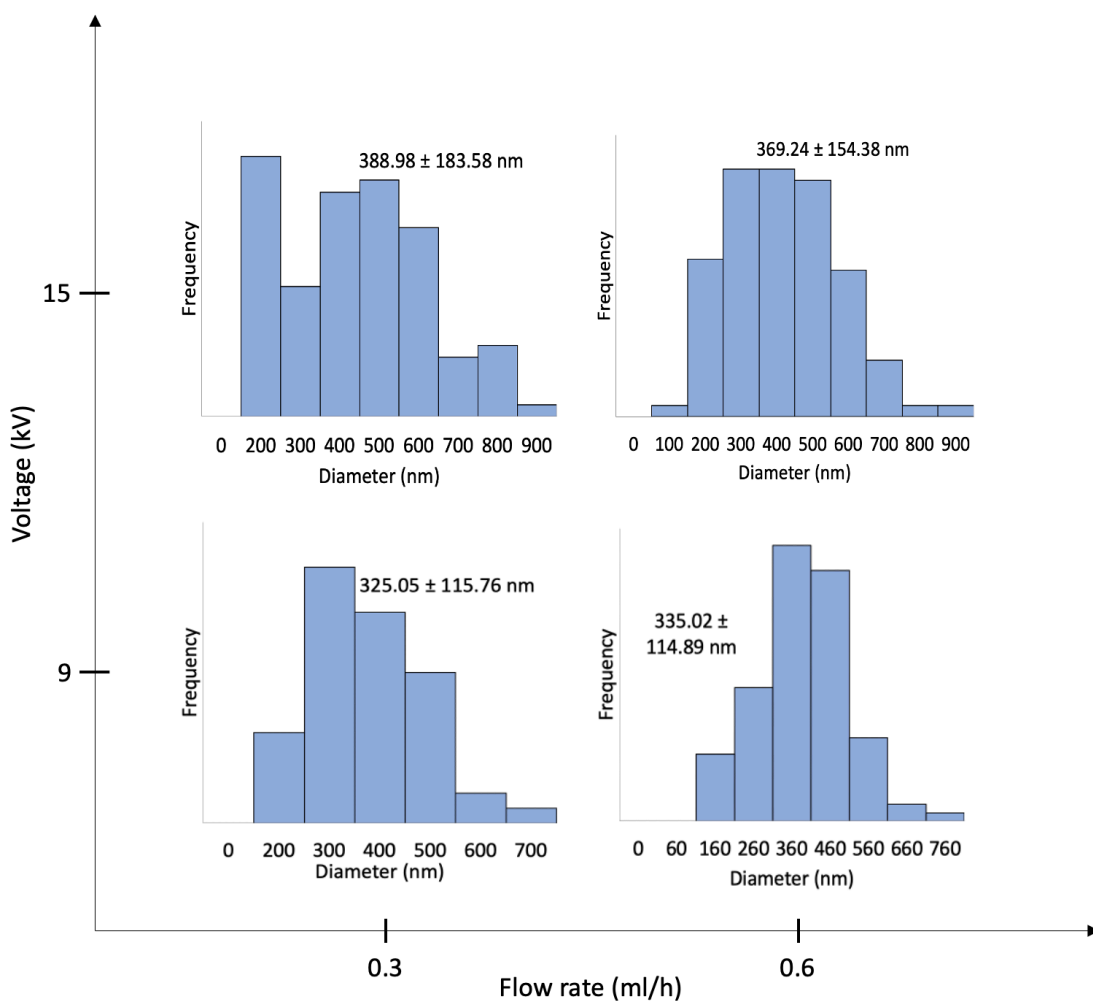
Figure 4.20: Fiber diameter distribution of electrospun synthesized PNIPAm from THF:DMF (1:1) at 15 % (w/w) concentration from combinations of applied voltage of 9 and 15 kV, and flow rate 0.3 and 0.6 ml/h.

Neat electrospun PNIPAm dissolves immediately in water upon exposure. Cross-linker was used to mitigate the instant dissolution of electrospun neat PNIPAm membrane in water. The addition of OPEPOSS as cross-linker and curing post-electrospinning yielded PNIPAm membranes with improved stability in aqueous environment. The resulting cross-linked PNIPAm membranes can withstand instant

dissolution upon aqueous exposure. R. E. Young et. al. studied the aqueous degradation of OPEPOSS cross-linked and aligned electrospun PNIPAm at 37 °C (above LCST of PNIPAm) in water for 24 hours and 7 days, and reported no significant mass loss at the end of both durations[12]. In the literature, study on aqueous degradation of OPEPOSS cross-linked electrospun PNIPAm over extended periods of more than 7 days have not been reported. The resulting electrospun and post crosslinked nanofibrous PNIPAm membrane was characterized in the following sections (section 4.3.1 to section 4.3.6). Fiber and pore sizes are reported as mean±standard deviation.

4.3.1 Solution viscosity

Viscosity of electrospinning solution is one of the most important parameters to ensure electrospinnability. Figure 4.21 shows the plot of shear stress against shear rate of the electrospinning solution of synthesized PNIPAm at 15 % (w/w) in THF:DMF (1:1) (detailed in section 3.6.1). The linear plot indicates the Newtonian flow of the solution and the viscosity is given by the gradient, 0.1218 Pa·s (1.22 poise). The viscosity corresponds closely to A100 PNIPAm at 12 % (w/w) in MeOH (i.e., 0.1799 Pa.s (1.80 poise)) as discussed in section 4.1.7. The slight difference in these viscosities can be related to the

the slight difference in concentration (15 vs. 12 % (w/w)) and different solvent used (THF:DMF (1:1) vs. MeOH).
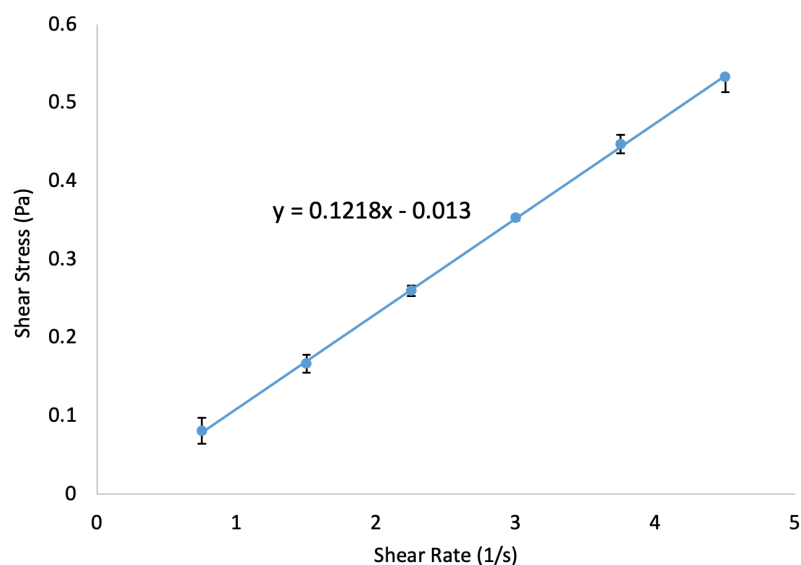
Figure 4.21: Plot of shear stress against shear rate of electrospinning solution of synthesized PNIPAm with OPEPOSS+EMI in THF:DMF (1:1).

4.3.2 Fiber diameter distribution

The fiber diameter distribution of electrospun synthesized PNIPAm before and after cross-linking (i.e., heat curing process for 4 hours at 120 °C) is presented in Figure 4.22. Before cross-linking, the fiber diameter was 369.24 ± 154.38 nm and after cross-linking, fiber diameter was increased to 436.35 ± 187.04 nm. Additionally, prior to cross-linking, sizes of electrospun fibers were in the range of 100 to 900 nm. After cross-linking the range of fiber size increased to 100

to 1000 nm. The increase in fiber diameter indicates that swelling of fibers took place upon cross-linking with OPEPOSS. Nevertheless, electrospun PNIPAm fibers (cross-linked or uncross-linked) highly mimic the fiber size of native collagen fibers (i.e., 50 to 500 nm) in the native ECM [64].
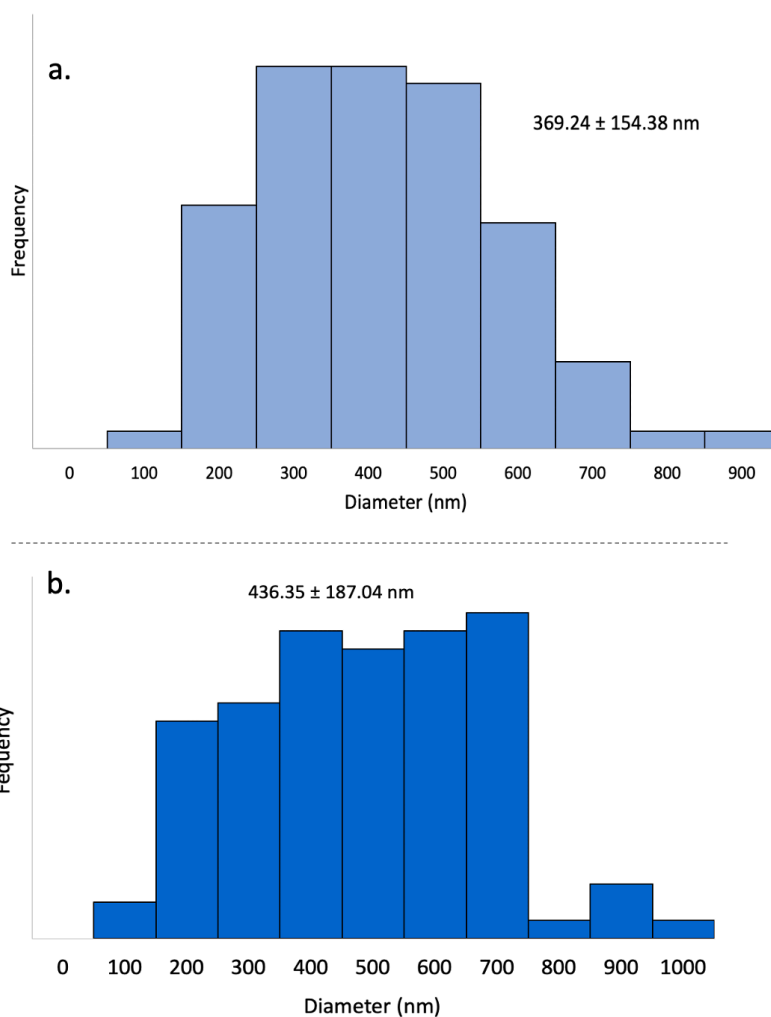
Figure 4.22: Fiber diameter distribution of nanofibers of electrospun synthesized PNIPAm (a) before cross-linking/curing, and (b) after cross-linking/curing (4 hours at 120 °C). An increase in fiber diameter occurred upon cross-linking.

138

4.3.3 Pore size distribution

The pore size distribution of electrospun synthesized PNIPAm membrane before and after cross-linking is shown in Figure 4.23. The pore size before cross-linking was 2.63 ± 2.98 µm and 1.24 ± 1.27 µm after. The reduction in pore size can be attributed to the swelling of PNIPAm fibers. Figure 4.24 shows the FESEM image of cross-linked and uncross-linked electrospun synthesized PNIPAm. Several intersections between fibers for cross-linked electrospun PNIPAm exhibit fusing of fibers, indicating point of cross-linking between fibers. Cross-linking is also expected to occur within individual fiber. Additionally, pores of electrospun membranes were generally observed as trapezoidal in shape, therefore, pore size was determined by using the maximum Feret diameter as mentioned in section 3.7.2. The Feret diameter measures the distance between two tangential lines on the edge of a measured particle. The maximum Feret diameter takes the maximum of the Feret diameter measured and all pore size measurements were conducted with ImageJ (version 1.53) using the analyze particle function. Figure 4.25 shows a simple schematic of the measurement of maximum Feret diameter of a pore on the surface of electrospun synthesized PNIPAm membrane. Nevertheless, the pore sizes before cross-linking range from 2 to 18 µm while after cross-linking, the range of pore sizes reduced to 1 to 8 µm with most of the pores measuring around 1 µm. From the

electron micrograph in Figure 4.24, observing perpendicularly to the plane (i.e., into the page) of electrospun synthesized PNIPAm membrane shows that larger pores are located on the planar surface of the membrane and pore sizes become smaller towards the inner thickness (i.e., into the page). It is suggested that a pore size of 5 μm is suitable for neovascularization, while 5-15 μm is optimal for fibroblast ingrowth[93]. Scaffolds with small pore sizes supports the adhesion of cells while larger pores facilitate migration of cells from the surface to the inner layer. It is to note that if pore size is much larger than cells, it may be difficult for cells to adhere to the scaffold and most cells would adhere to the culture plate[224]. Narrow pore sizes were reported to inhibit tissue differentiation due to insufficient vascularization[225]. The pore size of cross-linked electrospun synthesized PNIPAm scaffold are relatively small (i.e., 1.24 ± 1.27 μm), which suggests that it could support cell adhesion on its planar surface. Since larger pores are also on the planar surface of the membrane, the range of pore size (i.e., 1 to 8 μm) suggests that cell ingrowth or cell migration towards the inner layers is possible for cells such as fibroblasts. The narrow pore sizes may also inhibit cell differentiation. However, this may be favorable for cell culture applications where maintaining cell phenotype is desirable.
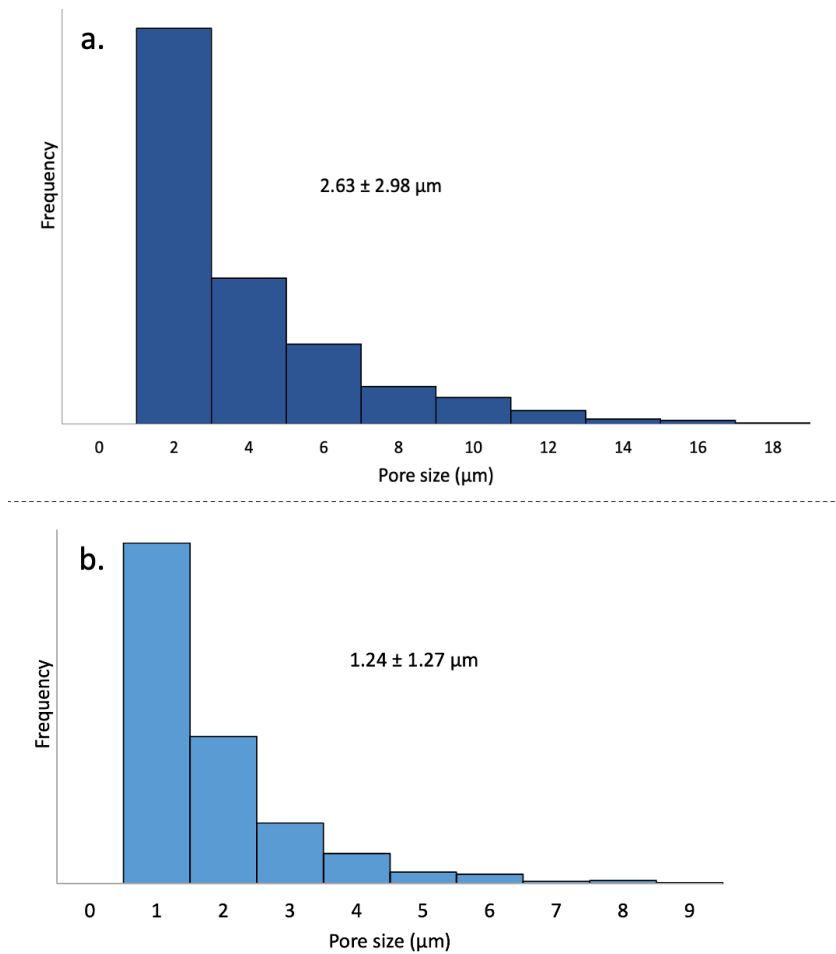
Figure 4.23: Pore size distribution of nanofibers of electrospun synthesized PNIPAm (a) before cross-linking/curing, and (b) after cross-linking/curing (4 hours at 120 °C). A reduction in pore size occurred upon cross-linking.
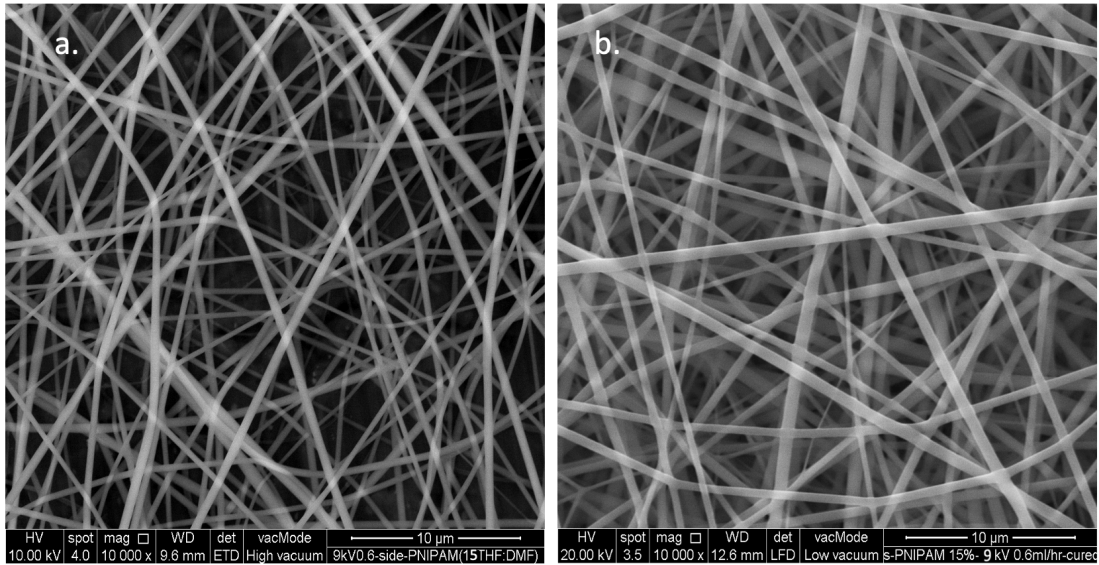
Figure 4.24: FESEM micrograph of nanofibers of electrospun synthesized PNIPAm (a) before cross-linking/curing, and (b) after cross-linking/curing (4 hours at 120 °C). Magnification x10 000. Fused fibers at fiber intersections can be observed after cross-linking.
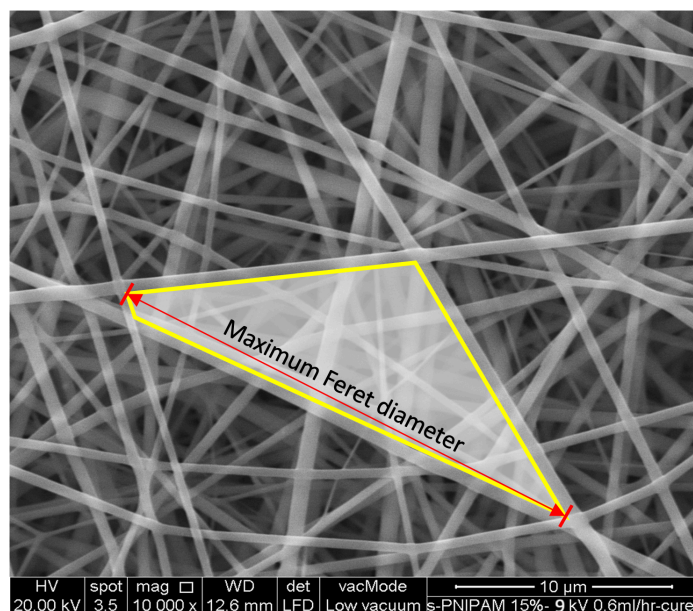
Figure 4.25: Schematic of maximum Feret diameter measurement on a trapezoidal pore on the surface of electrospun synthesized PNIPAm.

4.3.4 Porosity

The porosity of a nanofibrous membrane represents the percentage of void space within a porous membrane. Figure 4.26 shows the cross-section of uncross-linked and cross-linked porous PNIPAm nanofibrous membrane under FESEM.
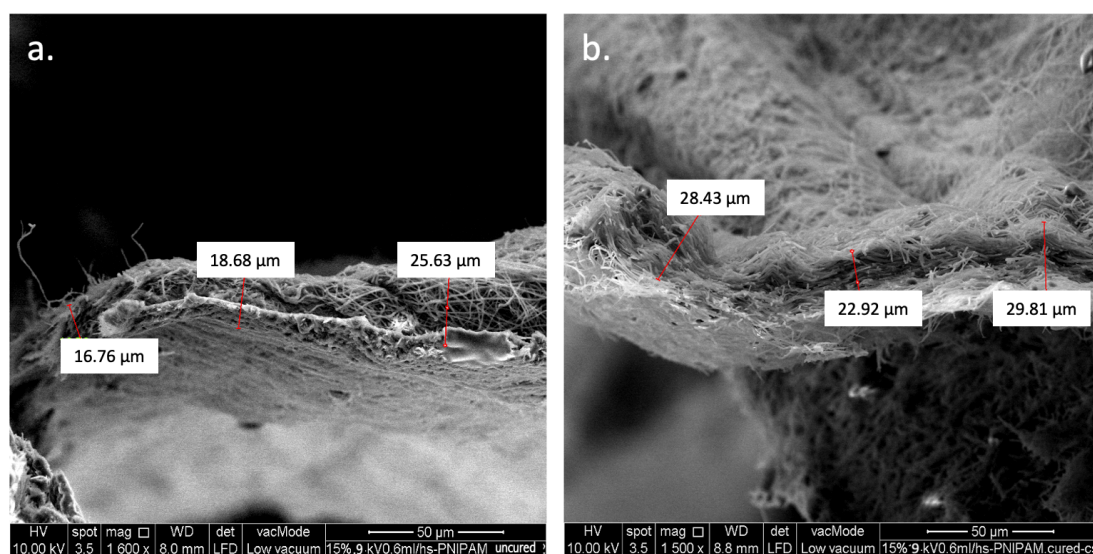
Figure 4.26: Cross-section of electrospun nanofibrous membrane of synthesized PNIPAm (a) before cross-linking/curing, and (b) after cross-linking/curing (4 hours at 120 °C). Magnification x1500.

The porosity of electrospun membrane of PNIPAm before cross-linking was computed to be 74.4 %. After cross-linking, the porosity was computed to be 63.6 %, as estimated by the gravimetric method detailed in section 3.7.4. The slight decrease in porosity can be attributed to the expansion of fibers upon cross-linking and can be corroborated with the decrease in pore size. For stem cells, it was reported that a porosity of 96 % was optimum to induce stem cell

chondrogenic differentiation while 75 % was optimum for osteogenic differentiation[225].

4.3.5 Aqueous stability

Uncross-linked electrospun PNIPAm have poor aqueous stability and dissolves instantly upon exposure to aqueous media. After cross-linking, electrospun PNIPAm membrane was able to withstand instant aqueous dissolution. A degradation study of electrospun PNIPAm membrane in GMEM was conducted across 1, 2, 3, 5, 7, 14, 21 and 28 days incubated at 37 °C and 5 % CO_2. Figure 4.27 shows the percentage mass loss of PNIPAm membrane in GMEM from day 1 through day 28. The profile shows a relatively rapid degradation at the beginning from day 1 through day 7 with approximately 19 % mass loss. Onwards from day 7 up to day 28, degradation rate can be observed to slow down up to a total mass loss of 35 %. The gradual degradation of cross-linked electrospun PNIPAm can be attributed to the dissolution of loosely entangled PNIPAm chains at the membrane surface where these chains were not covalently cross-linked to the bulk membrane.
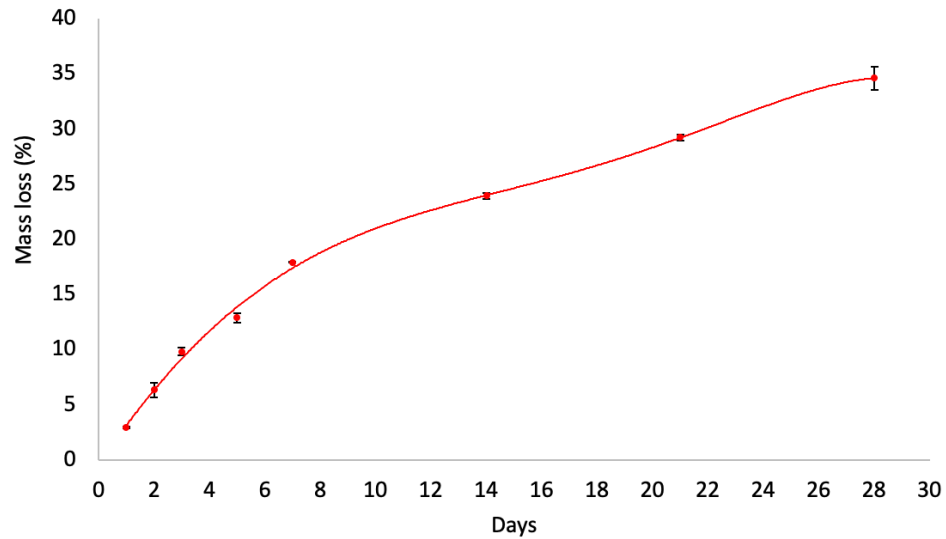
Figure 4.27: Percentage mass loss over time of electrospun cross-linked PNIPAm membrane in GMEM incubated at 37 °C and 5 % CO_2 simulating cell culture conditions.

4.3.6 Elemental analysis

Figure 4.28 shows the molecular structure of a repeat unit of PNIPAm while Table 4.3 shows the estimated elemental composition of PNIPAm. The weight percentage was computed by the following equation:

$$Weight\ \% = \frac{N_{a,x} \times M_{a,x}}{(N_{a,x} \times M_{a,x}) + (N_{a,y} \times M_{a,y}) + (N_{a,z} \times M_{a,z})} \times 100\ \%$$

………..eq. 4.4

Where $N_{a,x}$ is the number of atoms of element x and $M_{a,x}$ is the atomic weight of element x. $N_{a,y}$ is the number of atoms of element y and

$M_{a,y}$ is the atomic mass of element y. Similarly for $N_{a,z}$ and $M_{a,z}$. For instance, taking six carbon atoms (atomic mass=12 u), one nitrogen atom (atomic mass=14 u) and one oxygen atom (atomic mass=16 u) in a PNIPAm repeat unit. The weight percentage of carbon is therefore:

$$Carbon\ weight\ \% = \frac{6 \times 12}{(6 \times 12) + (1 \times 14) + (1 \times 16)} \times 100\ \% = 71\ \%$$

……….eq. 4.5

The atomic percentage is computed by simply taking the fraction of a particular element in the molecule. For instance, the atomic percentage of carbon is:

$$Carbon\ atomic\ \% = \frac{6}{(6 + 1 + 1)} \times 100\ \% = 75\ \%$$

……….eq. 4.6

Table 4.4 shows the elemental composition of uncross-linked electrospun synthesized PNIPAm and Figure 4.29 shows the corresponding energy dispersive X-ray (EDX) spectra. The weight and atomic percentage of carbon, nitrogen and oxygen elements are in close agreement with the composition estimated in Table 4.3 for PNIPAm and can be assigned to the organic groups within PNIPAm chains. The silicone peak in Figure 4.29 is assigned to the presence

of cross-linker OPEPOSS. Figure 4.30 shows the molecular structure of OPEPOSS constituting a silsesquioxane cage at the core and eight glycidyl groups surrounding the cage. Table 4.5 shows the elemental composition of electrospun cross-linked synthesized PNIPAm with OPEPOSS and Figure 4.31 shows the corresponding EDX spectra. No significant change in elemental composition was observed. This was expected as the electrospinning and curing (i.e., cross-linking) process was not expected to alter the elemental composition of PNIPAm and OPEPOSS. The aluminium peaks in the EDX spectrum in Figures 4.29 and 4.31 were assigned to the presence aluminium foil collector during EDX analysis.
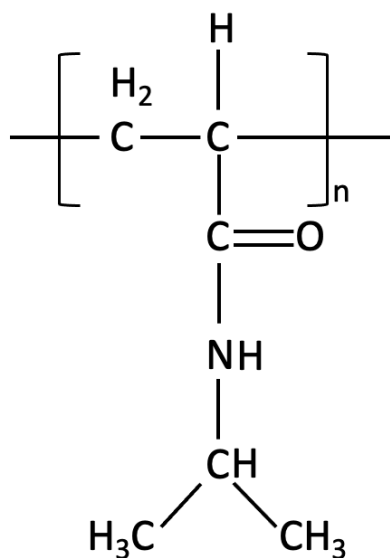
Figure 4.28: A repeat unit of PNIPAm molecule constituted by six carbon, one nitrogen and one oxygen atom.

Table 4.3: Calculated elemental composition of PNIPAm.

Element	Weight %	Atomic %
Carbon (C)	71	75
Nitrogen (N)	14	12.5
Oxygen (O)	16	12.5

Table 4.4: Elemental composition of uncross-linked electrospun synthesized PNIPAm (before curing for 4 hours at 120 °C).

Element	Weight %	Atomic %
Carbon (C)	70.50	75.09
Nitrogen (N)	13.25	12.10
Oxygen (O)	15.78	12.61
Silicone (Si)	0.46	0.21
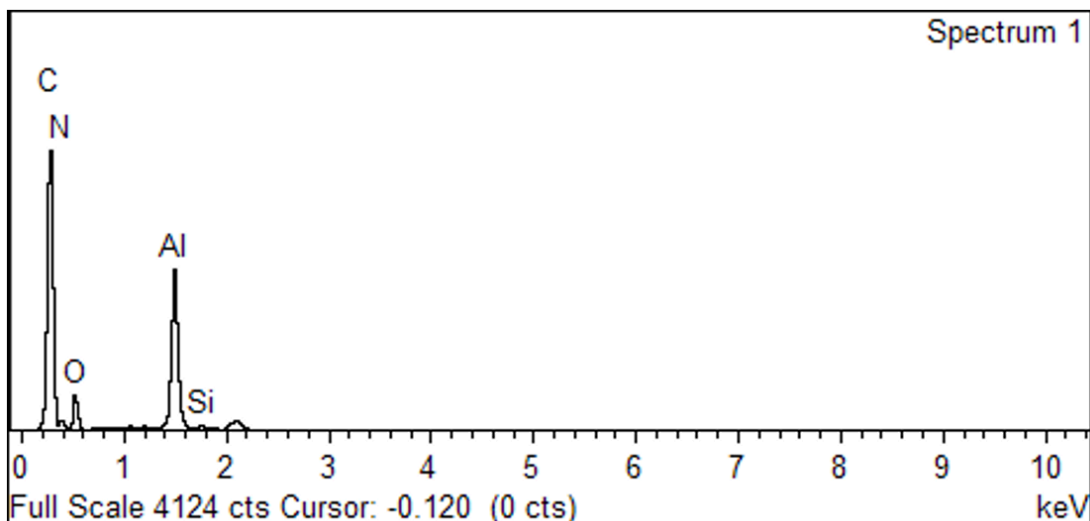
Figure 4.29: EDX spectra of uncross-linked electrospun synthesized PNIPAm with OPEPOSS (before curing for 4 hours at 120 °C).
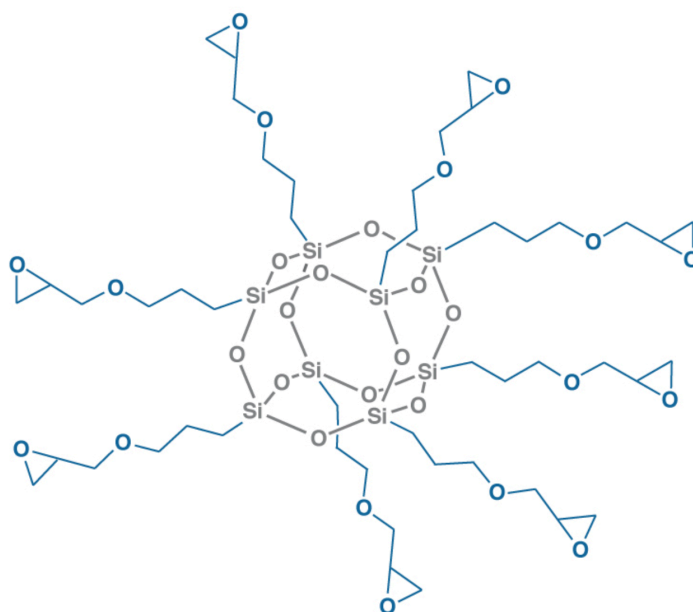
Figure 4.30: Molecular structure of OPEPOSS. Eight glycidyl groups (in blue) surrounds the silsesquioxane cage. Image from hybridplastics.com[226].

Table 4.5: Elemental composition of electrospun OPOEPOSS cross-linked (after curing for 4 hours at 120 °C) synthesized PNIPAm.

Element	Weight %	Atomic %
Carbon (C)	70.61	75.21
Nitrogen (N)	12.95	11.82
Oxygen (O)	15.95	12.74
Silicone (Si)	0.49	0.22
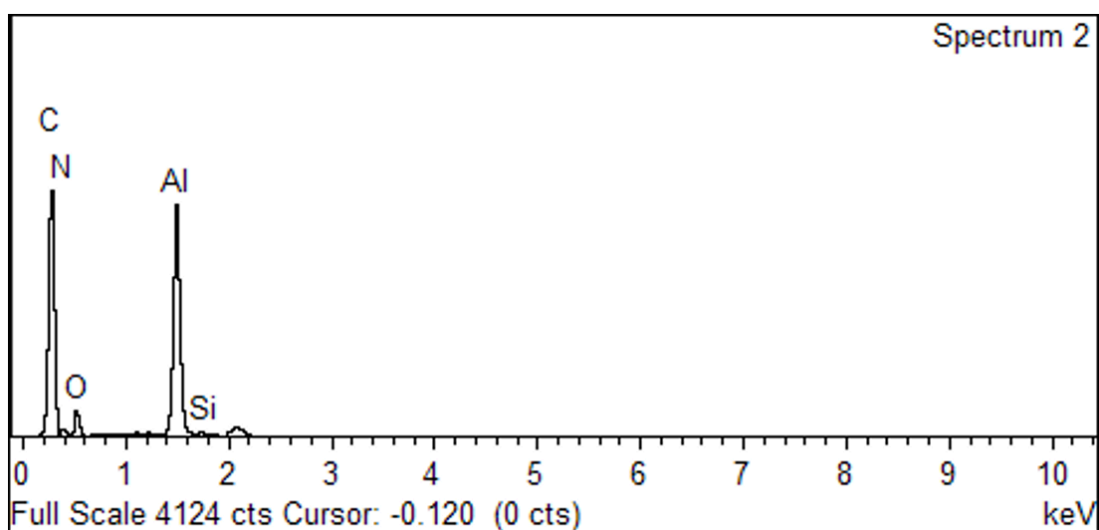
Figure 4.31: EDX spectra of electrospun OPOEPOSS cross-linked (after curing for 4 hours at 120 °C) synthesized PNIPAm.

4.4 Characterization of Collagen Functionalized PNIPAm Electrospun Nanofibers

Electrospinning of collagen from fluorinated solvents (e.g., HFIP, TFE) has been well established in literature, and the functionalization of synthetic polymers with collagen by using fluorinated solvents to form a blend has been widely practised. A blend of both PNIPAm and collagen should therefore be easily obtained with the use of fluorinated solvents, since PNIPAm is soluble in most organic solvents. However, it was noted by Zeugolis et. al. that electrospinning collagen from fluorinated solvents denatures collagen, and results in gelatin nanofibers[107]. A potential alternative approach to functionalize electrospun PNIPAm is by dip-coating in TFS collagen solution and dip-coating was similarly suggested by Zeugolis et. al. as a functionalization method to avoid denaturation of collagen. Both high molecular weight (300,000 Da) commercially available PNIPAm and synthesized PNIPAm were doped in two different concentrations of collagen in 0.5 M AA, as detailed in section 3.6.2. To briefly compare electrospun high molecular weight commercial PNIPAm and synthesized PNIPAm, the fiber diameter and pore size of the commercial PNIPAm was characterized. Figure 4.32 shows the FESEM image of electrospun high molecular weight commercial PNIPAm after cross-linking with OPEPOSS (detailed in section 3.6.1). Nanofibers were observed to be relatively curly, and

this could be due to the contraction of fibers after cross-linking. Figure 4.33 shows the corresponding fiber diameter distribution of cross-linked electrospun high molecular weight commercial PNIPAm. The fiber size of 165.09 ± 47.79 nm is significantly smaller as compared to cross-linked electrospun synthesized PNIPAm of 436.35 ± 187.04 nm (section 4.3.2). This can be attributed to the lower polymer concentration used of 12 % (w/w) versus 15 % (w/w) in THF:DMF (1:1) for high molecular weight commercial PNIPAm and synthesized PNIPAm, respectively. Additionally, its lower molecular weight of 300,000 Da as compared to the molecular weight of synthesized PNIPAm of 381,000 Da could have also contributed to the significantly smaller fiber diameter due to a lower degree of chain entanglement, allowing more stretching of PNIPAm jet in the electric field during electrospinning. Figure 4.34 shows the corresponding pore size distribution of cross-linked electrospun high molecular weight commercial PNIPAm. Pore sizes were similarly represented by their maximum Feret diameter as detailed in section 4.3.3. The pore size of cross-linked electrospun high molecular weight commercial PNIPAm was determined to be 0.58 ± 0.66 µm, which is significantly smaller than that of electrospun cross-linked synthesized PNIPAm of 1.24 ± 1.27 µm. The formation of smaller pore size can be attributed to the reduced whipping of the PNIPAm jet in the electric field, leading to more closely deposition of fibers on the collector. Table 4.6 summarizes the fiber diameter and pore size of cross-linked

electrospun high molecular weight commercial PNIPAm and synthesized PNIPAm.
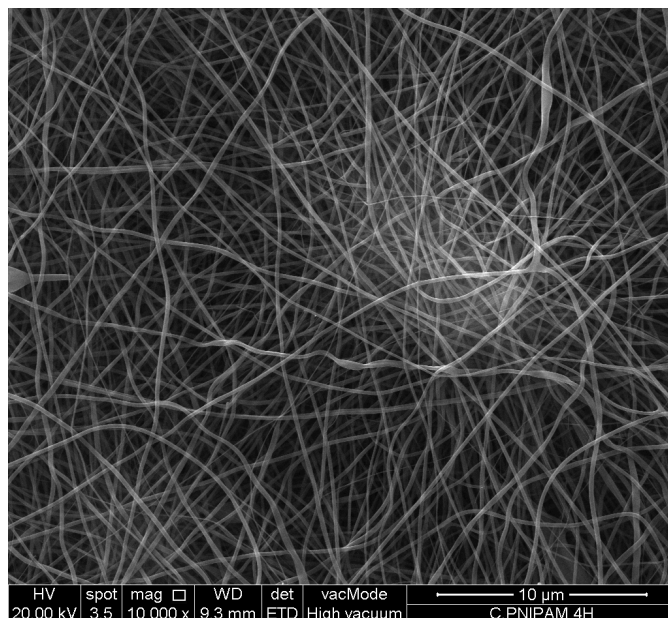
Figure 4.32: FESEM image of electrospun high molecular weight commercial PNIPAm.
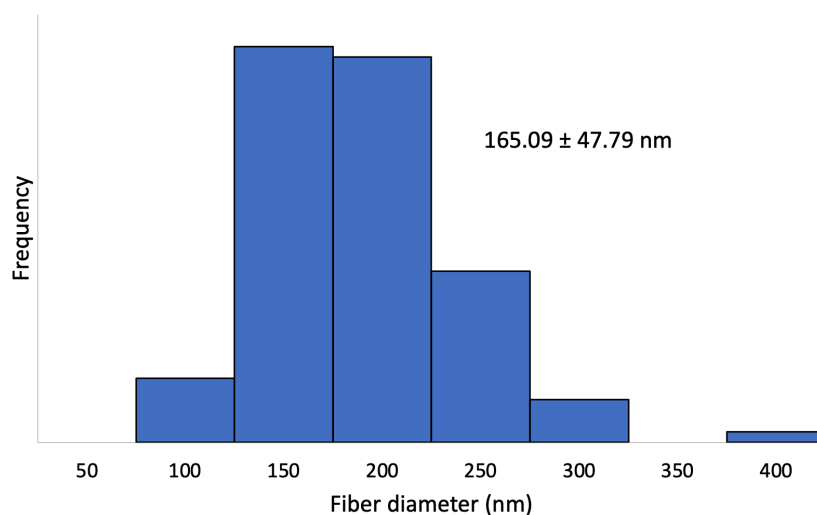
Figure 4.33: Fiber diameter distribution of OPEPOSS cross-linked electrospun high molecular weight commercial PNIPAm.
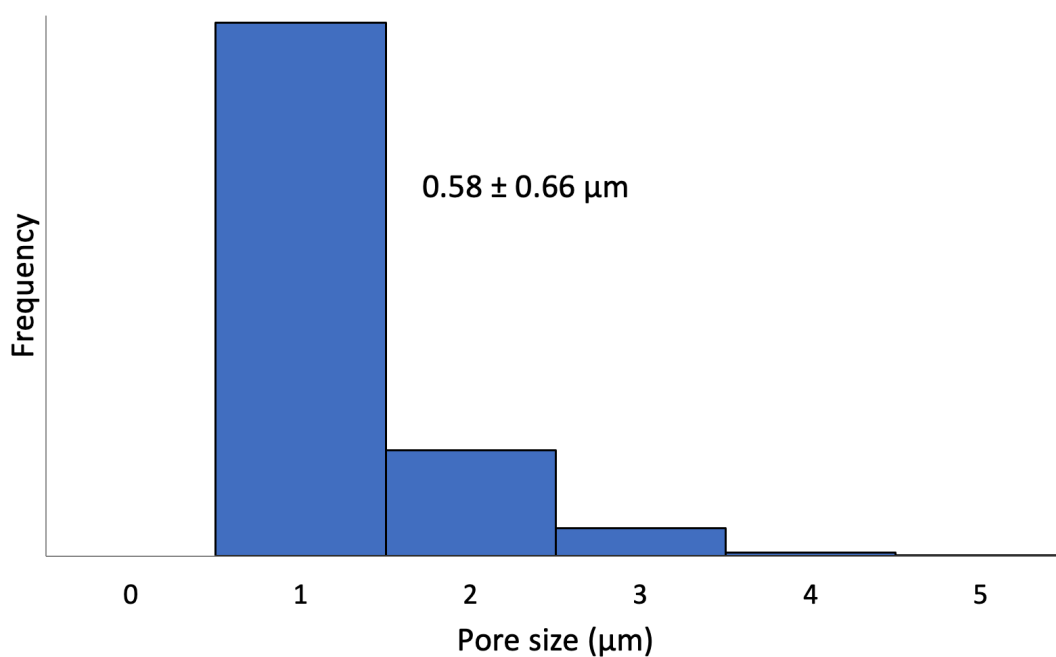
Figure 4.34: Pore size distribution of OPEPOSS cross-linked electrospun high molecular weight commercial PNIPAm.

Table 4.6: Fiber diameter and pore size of electrospun cross-linked high molecular weight commercial PNIPAm and synthesized PNIPAm.

	Fiber diameter (nm)	Pore size (µm)
Commercial PNIPAm	165.09 ± 47.79	0.58 ± 0.66
Synthesized PNIPAm	436.35 ± 187.04	1.24 ± 1.27

4.4.1 Water contact angle analysis

Wettability of scaffolds play an important role in its interaction with cells. In the work of Valamehr et. al., it was established that hydrophobic surfaces promoted the proliferation and differentiation of stem cells[227]. Tengvall et. al. and Gessner et. al. reported that hydrophobic surfaces promote protein adsorption, thus enhance cell adhesion onto the substrate. On the contrary, hydrophilic surfaces induce cell separation as water interact with the substrate surface via hydrogen bonding, disrupting points for cell attachment[228], [229]. Therefore, the wettability of doped scaffolds was studied and compared as detailed in section 3.7.5. Figure 4.35 shows the contact angle of each studied groups. Investigated group assignment: synthesized PNIPAm (SP), commercial PNIPAm (CP), dip coated synthesized PNIPAm in 0.1 mg/ml collagen (SP0.1CLG), dip coated commercial PNIPAm in 0.1 mg/ml collagen (CP0.1CLG), dip coated synthesized PNIPAm in 0.5 mg/ml collagen (SP0.5CLG), dip coated commercial PNIPAm in 0.5 mg/ml collagen (CP0.5CLG). All groups show a decreasing contact angle from 1 to 7 seconds of water drop exposure. It should be noted that a contact angle below 90 ° indicates hydrophilicity and above 90 ° indicates hydrophobicity [199]. Neat electrospun commercial PNIPAm was the only group to give a water contact angle of more than 90 ° at initial stage (i.e., from 1 to 3 seconds), which could be attributed to its small pore size of 0.58 ±

0.66 μm, inhibiting water penetration better than neat electrospun synthesized PNIPAm (contact angle slightly below 90 °). Both neat electrospun synthesized and commercial PNIPAm show a final contact angle of approximately 70° at 7 seconds confirming the hydrophilicity of PNIPAm at 25 °C (i.e., below LCST of 32 °C). Addition of 0.1 mg/ml of collagen to both electrospun synthesized and commercial PNIPAm decreases the initial and final contact angles, indicating an increase in hydrophilicity of the functionalized material with collagen surface coating. A further increase in hydrophilicity was observed with introduction of higher collagen content of 0.5 mg/ml. With the increase in hydrophilicity of PNIPAm scaffolds while hydrophobic surfaces favor cell attachment, the addition of collagen may diminish the capability of PNIPAm scaffolds for cell attachment. However, introduction of collagen also increases the cell adhesion molecules on PNIPAm scaffolds. Therefore, there exist a competition between hydrophilicity and amount of cell adhesion sites which could potentially lead to an optimum collagen content to maximize cell attachment.
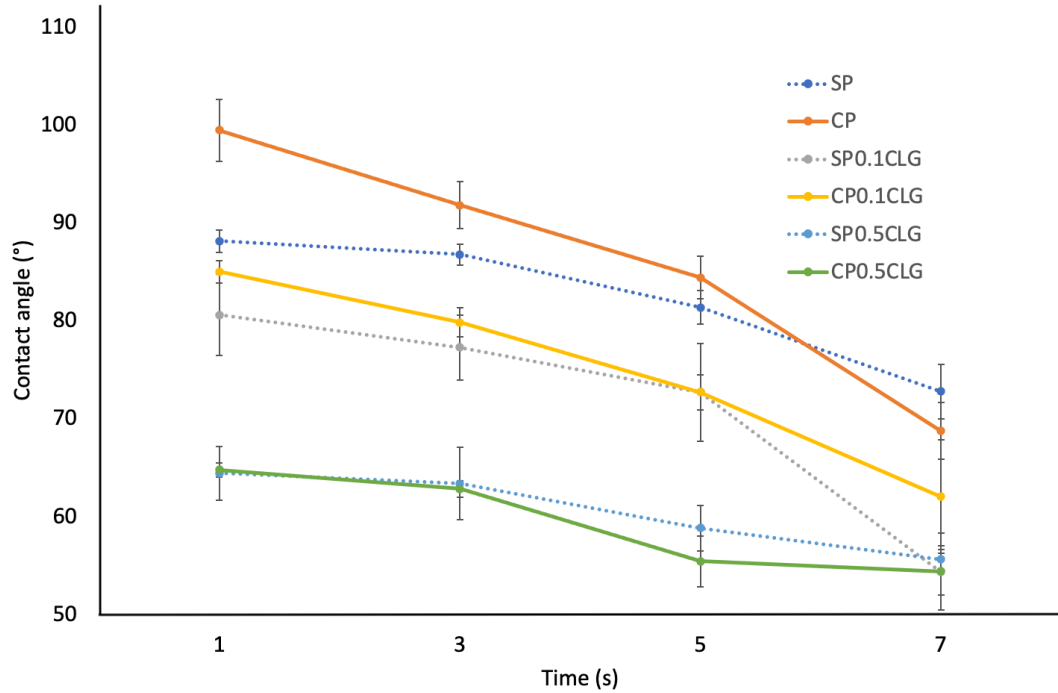
Figure 4.35: Contact angles of neat and collagen doped PNIPAm.

4.4.2 Morphology of collagen dip coated PNIPAm

Figure 4.36 shows the FESEM images of each studied groups. Figures 4.36(a) and 4.36(b) show similar fibrous morphology with noticeable swelling of fibres, which can be attributed to hydration resulting from sterilization and PBS washing processes. In Figures 4.36(c) and 4.36(d), flaky materials (circled in red) can be observed together with a layer of coating on the fibres, suggesting the immobilization of collagen on the surface of electrospun PNIPAm. As collagen content increased, thicker layer of coating can be observed together with filling of micropores, suggesting higher content of collagen immobilized on the surface of electrospun PNIPAm.
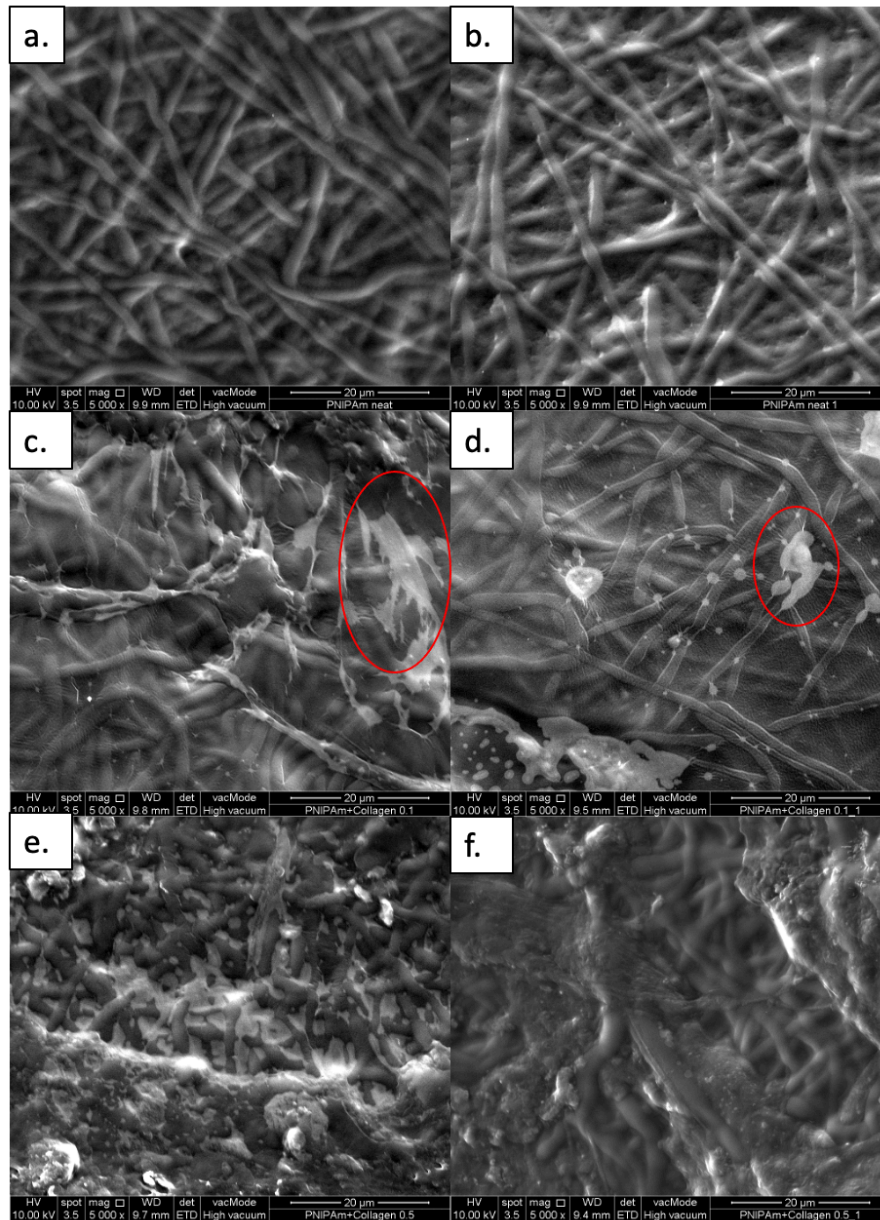
Figure 4.36: FESEM micrograph of (a) SP, (b) CP (c) SP0.1CLG (d) CP0.1CLG, (e) SP0.5CLG and (f) CP0.5CLG. All groups were sterilized and washed with PBS.

4.4.3 FTIR analysis of collagen dip coated PNIPAm

Figure 4.37 shows the FTIR spectra of each group. All groups exhibit similar peaks, which corresponds to the FTIR spectrum of PNIPAm as discussed in section 4.1.1.1. No significant peaks could be observed to confirm the presence of collagen. This can first be explained by the low content of collagen present on the PNIPAm nanofibers, which does not significantly contribute to peaks at wavenumbers specific to collagen. Besides that, PNIPAm and collagen also possess similar functional groups such as C=O, -NH and -CH, which would result in overlapping of peaks in an FTIR spectrum, albeit the little contribution from collagen.
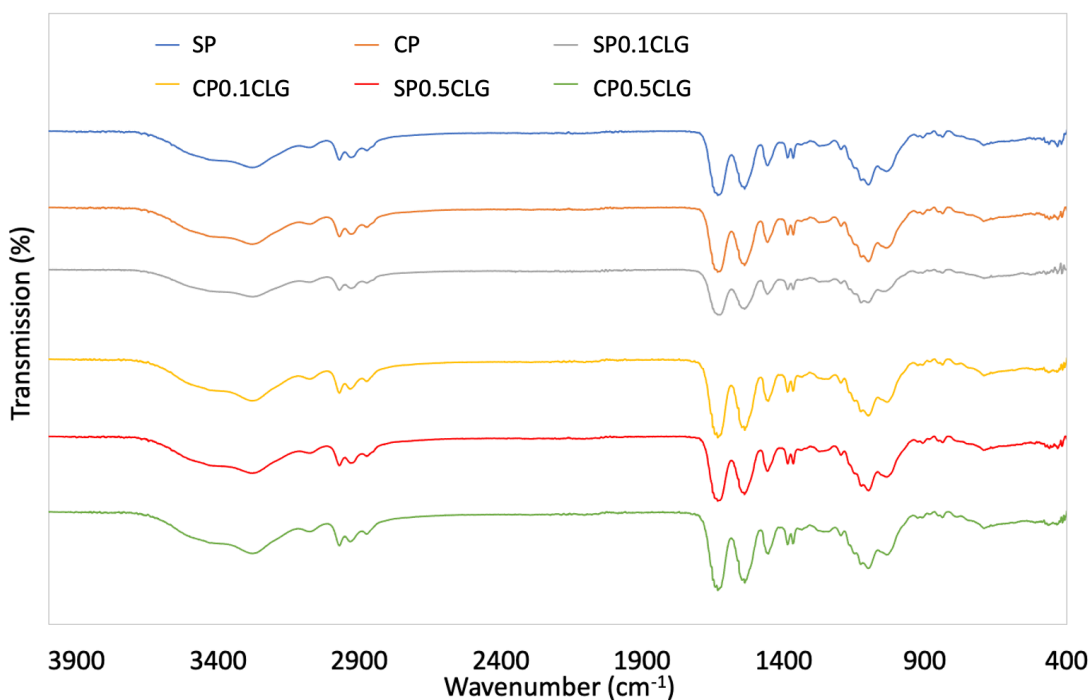
Figure 4.37: FTIR spectrum of SP, CP, SP0.1CLG, CP0.1CLG, SP0.5CLG and CP0.5CLG. All groups were sterilized and washed with PBS.

4.4.4 Thermal analysis of collagen dip coated PNIPAm

Figure 4.38 shows the TGA curve of the studied groups. All groups show similar degradation profile as PNIPAm as discussed in section 4.1.5, with major degradation occurring at approximately 380 °C. Both neat synthesized and commercial PNIPAm also show a final weight of ~10 %, which is in close agreement with the TGA curve of PNIPAm (section 4.1.5). Samples dip coated with 0.1 mg/ml collagen show a higher final weight of ~25 % while samples dip coated with 0.5 mg/ml of collagen show further increase in final weight of ~30 %. The increase in final weights can be attributed to heat shielding by collagen, and as collagen content increased, there exist further

heat shielding. This further corroborates the immobilization of collagen on PNIPAm nanofibers in dip coated groups.
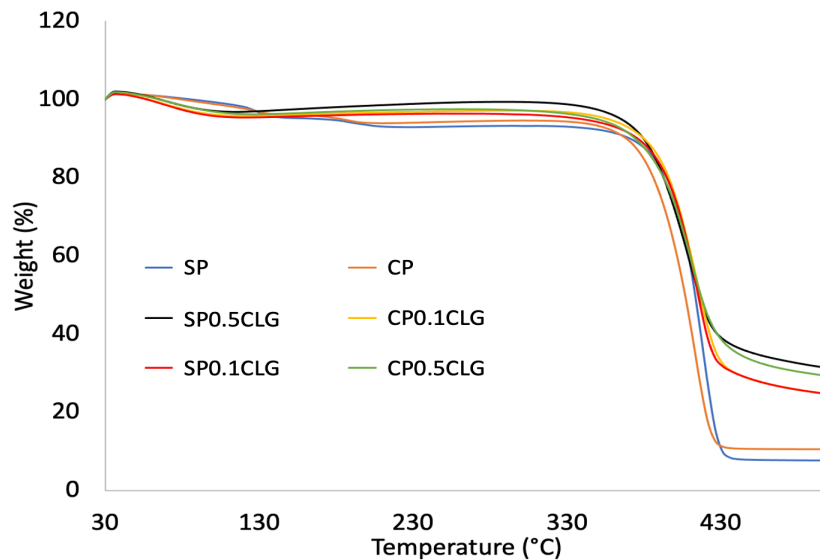
Figure 4.38: TGA curve of SP, CP, SP0.1CLG, CP0.1CLG, SP0.5CLG and CP0.5CLG. All groups were sterilized and washed with PBS.

4.5 Cell Culture Studies

This section explores preliminary assessment on the cell viability of R3-AFSC on electrospun PNIPAm scaffolds along with their TFS collagen functionalised formulations. As a proof-of-concept study, the spontaneous cell release by cooling (immersion in room temperature culture media) was also investigated.

4.5.1 Cell culture

R3-AFSC was first seeded on gelatin-coated substrate which was used as a positive control and observed after 4 and 48 hours. Figure 4.39 shows microscope images of R3-AFSC at 4 hours after initial

seeding, 24 hours, and confluence. At 4 hours seeding, the cells appeared slightly elongated as they spread out to attach to the gelatin-coated T25 flask. At 24 hours, more cells appear to attach to the flask. At confluence, all cells appear fusiform forming a cell monolayer. The population doubling time for R3-AFSC was computed as 22.93 hours. The relatively short population doubling time gives R3-AFSC great proliferative potential, making it a good source of stem cells capable of doubling its population within a day.
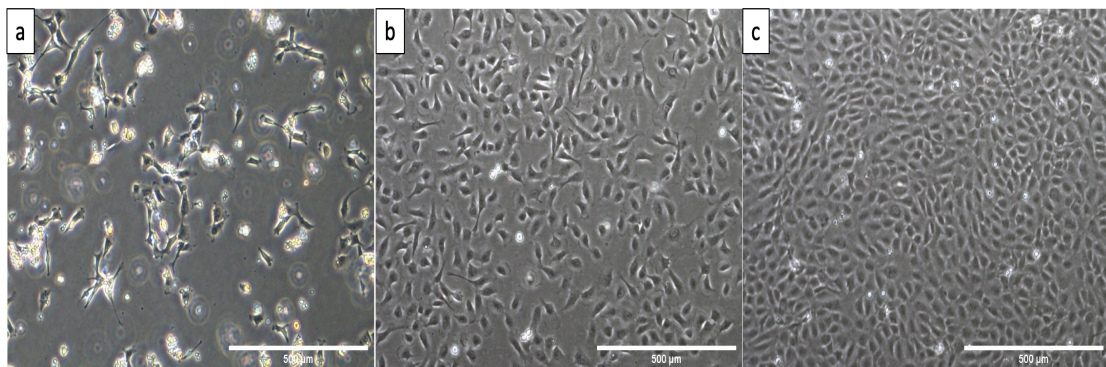
Figure 4.39: Microscope images of R3-AFSC at (a) cell attachment after 4 hours (b) 24 hours and (c) cell confluence after 48 hours.

4.5.2 Cell viability

PNIPAm is known to be biocompatible and cells such as brain cancer cells[150], fibroblasts[12], EMT6 tumour cells and MC3T3-E1 osteoblasts[10] have been studied on electrospun PNIPAm. However, study on stem cells on electrospun PNIPAm has yet to be reported. Additionally, as PNIPAm was synthesized from its monomer NIPAm

and surfactant SDS, both of which are known to be toxic. There was concern over the cell viability of electrospun synthesized PNIPAm, even after extensive purification of PNIPAm after synthesis. Hence, a study on cell viability on electrospun synthesized PNIPAm was carried out to address these concerns and was compared to cell viability on electrospun commercial PNIPAm. Both electrospun synthesized and commercial PNIPAm were also functionalized with TFS collagen at different concentrations to investigate the effect of collagen functionalization on the cell viability on these scaffolds. Figure 4.40 shows the sterilized and PBS washed scaffold before cell seeding.
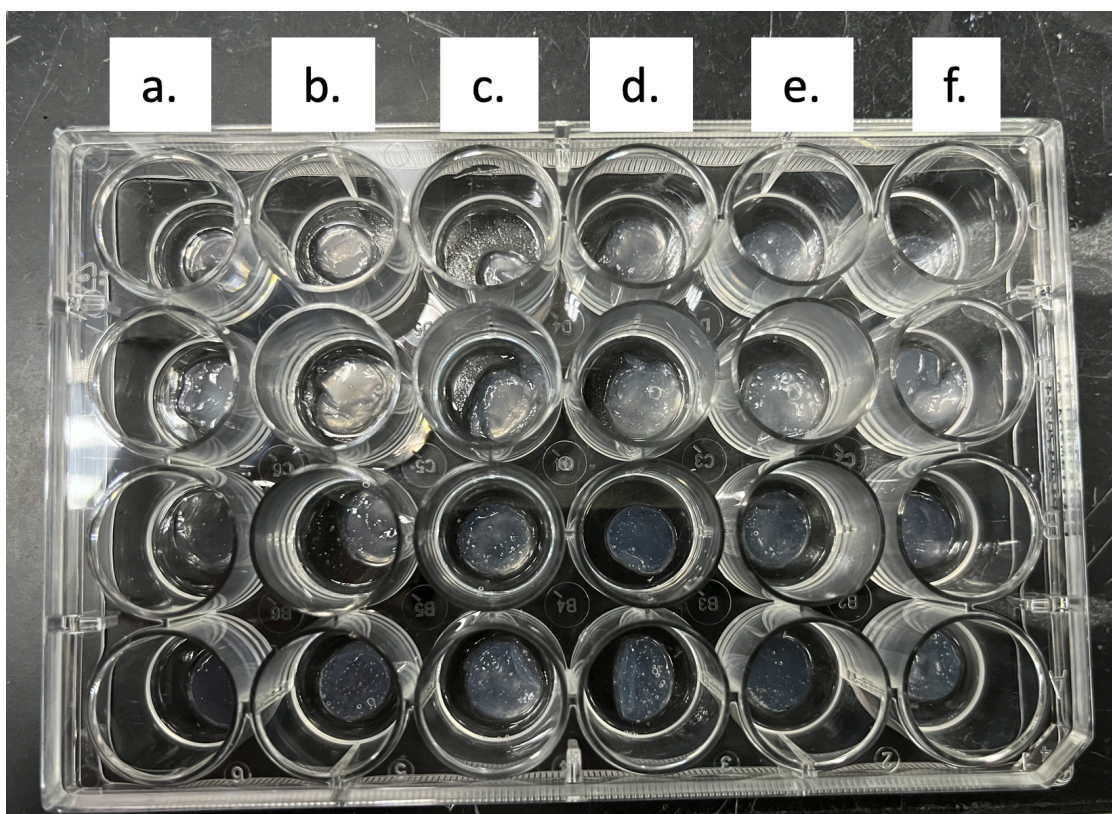
Figure 4.40: Sterilized and PBS washed scaffolds of neat (a) synthesized PNIPAm, (b) commercial PNIPAm, 0.1 mg/ml dip coated

(c) synthesized PNIPAm, (d) commercial PNIPAm, 0.5 mg/ml collagen dip coated (e) synthesized PNIPAm and (f) commercial PNIPAm.

Figure 4.41 shows the cell viability of R3-AFSC on the electrospun synthesized PNIPAm, commercial PNIPAm, synthesized PNIPAm dip coated with 0.1 % (w/w) TFS collagen, commercial PNIPAm dip coated with 0.1 % (w/w) TFS collagen, synthesized PNIPAm dip coated with 0.5 % (w/w) TFS collagen and commercial PNIPAm dip coated with 0.5 % (w/w) TFS collagen. Gelatin coated wells and gelatin coated wells with R3-AFSC were used as negative and positive controls, respectively. Cell viability on both electrospun synthesized and commercial PNIPAm were about 50 %. The similar cell viability on both these scaffolds indicates that the toxic substances during PNIPAm synthesis (e.g., NIPAm and SDS) are not concerns. However, the relatively low cell viability can be attributed to the lack of cell binding sites for cell attachment. Addition of TFS collagen by dip coating electrospun synthesized and commercial PNIPAm in 0.1 % (w/w) collagen resulted in an increase in both their cell viability to approximately 70 %. This can be expected as collagen possesses important RGD groups responsible as binding sites for cells. A further increase in collagen content on both electrospun PNIPAm doped in 0.5 % (w/w) TFS collagen shows further increase in cell viability to approximately 180 %, suggesting that the presence of TFS collagen

improved the proliferation of R3-AFSC. However, it is not indicative whether cell differentiation took place on these studied scaffolds.
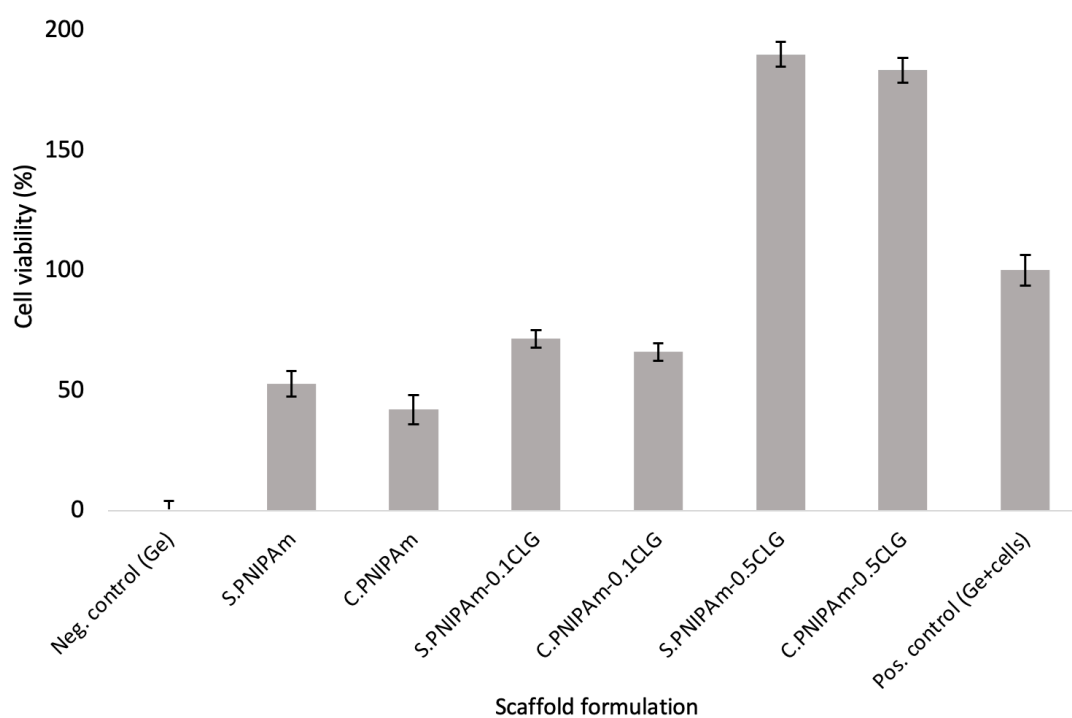
Figure 4.41: Cell viability of R3-AFSC on electrospun synthesized PNIPAm (S.PNIPAm), commercial PNIPAm (C.PNIPAm), synthesized PNIPAm dip coated with 0.1 % TFS collagen (S.PNIPAm-0.1CLG), commercial PNIPAm dip coated with 0.1 % TFS collagen (C.PNIPAm-0.1CLG), synthesized PNIPAm dip coated with 0.5 % TFS collagen (S.PNIPAm-0.5CLG), commercial PNIPAm dip coated with 0.5 % TFS collagen (C.PNIPAm-0.5CLG), gelatin coated negative control (Neg.control (Ge)) and gelatin coated positive control with R3-AFSC (Pos.control (Ge+cells)), from three independent experiments (n=3).

4.5.3 Cell release study

The cell release mechanism of both electrospun synthesized and commercial PNIPAm, along with their collagen doped formulated scaffolds was studied as detailed in section 3.8.5. Figure 4.42 shows the percentage of cell released from electrospun synthesized PNIPAm, commercial PNIPAm, synthesized PNIPAm dip coated with 0.1 % TFS collagen, commercial PNIPAm dip coated with 0.1 % TFS collagen, synthesized PNIPAm dip coated with 0.5 % TFS collagen and commercial PNIPAm dip coated with 0.5 % TFS collagen. It can be observed that both electrospun synthesized and commercial PNIPAm scaffolds released approximately 51 and 52 %, respectively, of cell upon cooling (immersion in room temperature ESM). Electrospun synthesized and commercial PNIPAm dip coated in 0.1 % TFS collagen both show approximately 48 % of cell released, while electrospun synthesized and commercial PNIPAm dip coated in 0.5 % TFS collagen both show approximately 43 % of cell released. As collagen content increases in both electrospun synthesized and commercial PNIPAm scaffolds, a gradual decrease in cell release percentage is observed. This trend can be attributed to the increase in cell binding sites (RGD sequence) on PNIPAm scaffolds, forming enhanced cell to scaffold attachment.
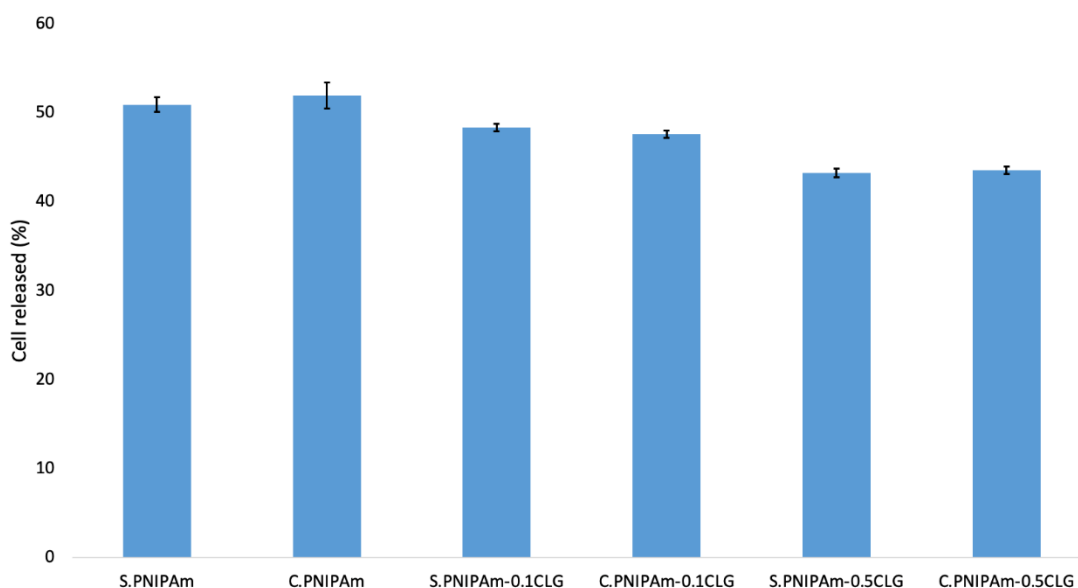
Figure 4.42: Percentage of cell released from electrospun synthesized PNIPAm (S.PNIPAm), commercial PNIPAm (C.PNIPAm), electrospun synthesized PNIPAm doped with 0.1 % TFS collagen (S.PNIPAm-0.1CLG), commercial PNIPAm doped with 0.1 % TFS collagen (C.PNIPAm-0.1CLG), electrospun synthesized PNIPAm doped with 0.5 % TFS collagen (S.PNIPAm-0.5CLG) and commercial PNIPAm doped with 0.5 % TFS collagen (C.PNIPAm-0.5CLG), from three independent experiments (n=3).

4.6 Key challenges and limitations

This subsection presents the key challenges and limitations of the experimental studies. In the synthesis of PNIPAm, there needs to be a dedicated reactor that could offer good control over heat and agitation to ensure its reproducibility. In addition, neat electrospun PNIPAm exhibits poor aqueous stability and dissolves instantly in

aqueous media. Cross-linking was necessary to improve its aqueous stability. However, cross-linking cannot be conducted prior to electrospinning as it inhibits PNIPAm chain mobility which is crucial to forming nanofibers during electrospinning. Hence, cross-linking should be carried out after electrospinning. On the other hand, extraction of collagen was a lengthy and labour-intensive process, with each extraction cycle taking approximate two weeks to complete. The yield was also found to be very low (i.e., 0.5 g of TFS collagen obtained from 50 g of fish scales).

Chapter 5

CONCLUSION AND RECOMMENDATION FOR FUTURE WORK

5.1 Conclusion

PNIPAm of weight average molecular weight of 381 kDa was successfully synthesized via radical polymerization in a jacketed reactor flask equipped with a 90 mm anchor type impeller to provide constant agitation of 100 rpm at 80 °C. The synthesized PNIPAm was highly electrospinnable from the binary solvent THF:DMF (1:1) at a concentration of 15 % (w/w), applied voltage 9 kV, flow rate 0.6 ml/h and working distance of 18 cm. Ambient conditions during electrospinning was recorded with a temperature of ~25 °C and relative humidity of ~50 %. However, neat electrospun PNIPAm exhibits poor aqueous stability and dissolves instantly in water or aqueous media. Cross-linking was employed by the addition of 20 % (w/w) of OPEPOSS to PNIPAm electrospinning solution and cured at 120 °C for 4 hours to yield electrospun PNIPAm with significantly improved aqueous stability. A gradual mass loss profile at cell incubation conditions (i.e., 37 °C and 5 % CO_2 in GMEM) was observed up to 28 days with a total mass loss of 35 %. This enables electrospun PNIPAm to act as an interim cell culture support while cells express their own ECM. The final fiber diameter was measured as 436.35 ± 187.04 nm, which highly mimics the size of collagen

fibrils in the native ECM. The pore size of the electrospun PNIPAm scaffold was measured as 1.24 ± 1.27 μm, and favours the preservation of cell phenotype. It also exhibits a highly porous structure with a measured porosity of 63.6 % allowing for vascularization. On the other hand, collagen type I (determined by SDS-PAGE) was successfully extracted via the dilute acid extraction method from tilapia fish scales, yielding high quality collagen in terms of intact triple-helical structure as indicated by FTIR analysis. The dip coating method was employed to functionalized electrospun PNIPAm scaffolds with TFS collagen, and presents as a simple and straightforward way to immobilize collagen onto PNIPAm nanofibers. Cell culture studies indicate that PNIPAm nanofibers dip coated in 0.5 % (w/w) TFS collagen solution achieved the highest cell viability of 180 %, while the same formulated scaffold is capable of spontaneous cell release of 43 %. Altogether, this work has presented a cost effective method to synthesize PNIPAm that is highly electrospinnable, while an aqueous stable electrospun PNIPAm scaffold was fabricated. Extracting collagen from tilapia fish scales converts the fish waste into a value added product. Finally, collagen functionalized electrospun PNIPAm scaffold presents as a viable alternative to conventional cell culture substrates, while furnishing a spontaneous cell release mechanism.

5.2: Recommendation for future work

This work explored the viability of collagen functionalized PNIPAm electrospun scaffold via dip coating. There exist other functionalization methods such as co-electrospinning (simultaneous electrospinning of separate solutions of collagen and PNIPAm onto the same collector) and blending (electrospinning a single solution of collagen and PNIPAm), which could present their own unique advantages. Functionalization by co-electrospinning would exhibit layered nanofibers of collagen and PNIPAm in the resulting scaffold, if good fiber overlap can be achieved. Functionalization by blending have the advantage of a homogenous distribution of collagen on PNIPAm nanofibers. Additionally, Cell culture studies with R3-AFSC indicate good potential in the use of TFS collagen functionalized PNIPAm scaffold for cell cultivation. However, further studies need to be conducted to understand the cell differentiation potential with the currently formulated scaffold.

References

[1] N. Yamada, T. Okano, H. Sakai, F. Karikusa, Y. Sawasaki, and Y. Sakurai, "Thermo-responsive polymeric surfaces; control of attachment and detachment of cultured cells," *Die Makromol. Chemie, Rapid Commun.*, vol. 11, no. 11, pp. 571–576, Nov. 1990.

[2] C. Waymouth, "To disaggregate or not to disaggregate, injury and cell disaggregation, transient or permanent?," *In Vitro*, vol. 10, no. 1–2, pp. 97–111, Jul. 1974.

[3] B. Alberts, A. Johnson, J. Lewis, M. Raff, K. Roberts, and P. Walter, *Molecular biology of the cell*. Garland Science, 2002.

[4] X. Lang, A. D. Patrick, B. Hammouda, and M. J. A. Hore, "Chain terminal group leads to distinct thermoresponsive behaviors of linear PNIPAM and polymer analogs," *Polymer (Guildf).*, vol. 145, pp. 137–147, Jun. 2018.

[5] R. Contreras-Ca, L. Schellkopf, C. Ferna, I. Pastoriza-Santos, J. Pe, and M. Stamm, "Effect of the cross-linking density on the thermoresponsive behavior of hollow PNIPAM microgels," *Langmuir*, vol. 31, no. 3, pp. 1142–1149, 2014.

[6] R. M. P. da Silva, J. F. Mano, and R. L. Reis, "Smart thermoresponsive coatings and surfaces for tissue engineering: switching cell-material boundaries," *Trends Biotechnol.*, vol. 25, no. 12, pp. 577–583, Dec. 2007.

[7]   P. Bhol, M. Mohanty, and P. S. Mohanty, "Polymer-matrix stabilized metal nanoparticles: Synthesis, characterizations and insight into molecular interactions between metal ions, atoms and polymer moieties," *J. Mol. Liq.*, vol. 325, p. 115135, Mar. 2021.

[8]   J. Litowczenko *et al.*, "Synthesis, characterization and in vitro cytotoxicity studies of poly-N-isopropyl acrylamide gel nanoparticles and films," *Mater. Sci. Eng. C*, vol. 118, p. 111507, Jan. 2021.

[9]   R. Jiang, J. Li, Z. Qiang, L. Wang, T. Wang, and S. Shi, "Synthesis and in situ gelation behavior of thermoresponsive poly(N -isopropylacrylamide)/chitosan microgels," *J. Macromol. Sci. Part B*, vol. 60, no. 2, pp. 136–152, Feb. 2021.

[10]   K. N. Cicotte, J. A. Reed, P. A. H. Nguyen, J. A. De Lora, E. L. Hedberg-Dirk, and H. E. Canavan, "Optimization of electrospun poly(N- isopropyl acrylamide) mats for the rapid reversible adhesion of mammalian cells," *Biointerphases*, vol. 12, no. 2, p. 02C417, 2017.

[11]   J. Wang, A. Sutti, X. Wang, and T. Lin, "Fast responsive and morphologically robust thermo-responsive hydrogel nanofibres from poly(N-isopropylacrylamide) and POSS crosslinker," *Soft Matter*, vol. 7, no. 9, pp. 4364–4369, 2011.

[12]   R. E. Young *et al.*, "Optimizing the alignment of thermoresponsive poly(N-isopropyl acrylamide) electrospun

nanofibers for tissue engineering applications: A factorial design of experiments approach," *PLoS One*, vol. 14, no. 7, p. e0219254, 2019.

[13] M. A. Ghavimi, A. Bani Shahabadi, S. Jarolmasjed, M. Y. Memar, S. Maleki Dizaj, and S. Sharifi, "Nanofibrous asymmetric collagen/curcumin membrane containing aspirin-loaded PLGA nanoparticles for guided bone regeneration," *Sci. Rep.*, vol. 10, no. 1, pp. 1–15, Dec. 2020.

[14] P. Chandika *et al.*, "Electrospun porous bilayer nano-fibrous fish collagen/PCL bio-composite scaffolds with covalently cross-linked chitooligosaccharides for full-thickness wound-healing applications," *Mater. Sci. Eng. C*, vol. 121, p. 111871, Feb. 2021.

[15] P. Muniyandi *et al.*, "ECM mimetic electrospun porous poly (l-lactic acid) (PLLA) scaffolds as potential substrates for cardiac tissue engineering," *Polymers (Basel).*, vol. 12, no. 2, Feb. 2020.

[16] A. Kramschuster and L. S. Turng, "Fabrication of tissue engineering scaffolds," in *Handbook of Biopolymers and Biodegradable Plastics: Properties, Processing and Applications*, 1st ed., S. Ebnesajjad, Ed. Oxford: Elsevier Inc., 2013, pp. 427–446.

[17] F. J. O'Brien, "Biomaterials & scaffolds for tissue engineering," *Mater. Today*, vol. 14, no. 3, pp. 88–95, 2011.

[18] J. P. and F. J., "Composite scaffolds for orthopaedic regenerative medicine," in *Advances in Composite Materials for Medicine and Nanotechnology*, vol. 10, B. Attaf, Ed. London: InTech, 2011, pp. 33–59.

[19] J. G. Najdanović *et al.*, "Effects of bone tissue engineering triad components on vascularization process: comparative gene expression and histological evaluation in an ectopic bone-forming model," *Biotechnol. Biotechnol. Equip.*, vol. 30, no. 6, pp. 1122–1131, 2016.

[20] K. Y. Tshai, S. S. Lim, L. C. Yong, and P. M. Chou, "Enhanced scaffold fabrication techniques for optimal characterization," in *Tissue Engineering Strategies for Organ Regeneration*, 1st ed., N. Sultana, S. Bandyopadhyay-Ghosh, and F. S. Chin, Eds. Florida: CRC Press, 2020, pp. 23–50.

[21] K. Nakayama, "In vitro biofabrication of tissues and organs," in *Biofabrication: Micro- and Nano-fabrication, Printing, Patterning and Assemblies*, G. Forgacs and S. Wei, Eds. Amsterdam: Elsevier Inc., 2013, pp. 1–21.

[22] E. A. Phelps and A. J. Garcia, "Update on therapeutic vascularization strategies," *Regen. Med.*, vol. 4, no. 1, pp. 65–80, 2009.

[23] H. C. H. Ko, B. K. Milthorpe, and C. D. Mcfarland, "Engineering thick tissues-the vascularisation problem," *Eur. Cells Mater.*, vol. 14, pp. 1–19, 2007.

[24] I. V. Yannas, E. Lee, D. P. Orgill, E. M. Skrabut, and G. F. Murphy, "Synthesis and characterization of a model extracellular matrix that induces partial regeneration of adult mammalian skin," *Proc. Natl. Acad. Sci. U. S. A.*, vol. 86, no. 3, pp. 933–937, 1989.

[25] C. M. Murphy, M. G. Haugh, and F. J. O'Brien, "The effect of mean pore size on cell attachment, proliferation and migration in collagen-glycosaminoglycan scaffolds for bone tissue engineering," *Biomaterials*, vol. 31, no. 3, pp. 461–466, 2010.

[26] C. M. Murphy and F. J. O'Brien, "Understanding the effect of mean pore size on cell activity in collagen-glycosaminoglycan scaffolds," *Cell Adh. Migr.*, vol. 4, no. 3, pp. 377–381, 2010.

[27] M. J. Cross, G. J. Roger, and J. Spycher, "Cementless fixation techniques and challenges in joint replacement," in *Joint Replacement Technology*, 2nd ed., P. A. Revell, Ed. Cambridge: Woolhead Publication, 2014, pp. 186–211.

[28] B. B. Mandal and S. C. Kundu, "Cell proliferation and migration in silk fibroin 3D scaffolds," *Biomaterials*, vol. 30, no. 15, pp. 2956–2965, 2009.

[29] U. J. Kim, J. Park, H. Joo Kim, M. Wada, and D. L. Kaplan, "Three-dimensional aqueous-derived biomaterial scaffolds from silk fibroin," *Biomaterials*, vol. 26, no. 15, pp. 2775–2785, 2005.

[30] S. M. Lien, L. Y. Ko, and T. J. Huang, "Effect of pore size on ECM

secretion and cell growth in gelatin scaffold for articular cartilage tissue engineering," *Acta Biomater.*, vol. 5, no. 2, pp. 670–679, 2009.

[31] Q. L. Loh and C. Choong, "Three-dimensional scaffolds for tissue engineering applications: Role of porosity and pore size," *Tissue Eng. - Part B Rev.*, vol. 19, no. 6, pp. 485–502, 2013.

[32] H. Ibrahim, S. N. Esfahani, B. Poorganji, D. Dean, and M. Elahinia, "Resorbable bone fixation alloys, forming, and post-fabrication treatments," *Mater. Sci. Eng. C*, vol. 70, pp. 870–888, Jan. 2017.

[33] B. M. Mandal, "Radical polymerization," in *Fundamentals Of Polymerization*, Singapore, SINGAPORE: World Scientific Publishing Company, 2010, pp. 97–212.

[34] R. J. Young and P. A. Lovell, "Radical polymerization," in *Introduction to Polymers*, 3rd ed., Bosa Roca, UNITED STATES: Taylor & Francis Group, 2011, pp. 61–122.

[35] B. M. E. Van Der Hoff, "Kinetics of Emulsion Polymerization," in *Polymerization and Polycondensation Processes*, N. A.J. Platzer, Ed. Washington, DC: American Chemical Society, 1962, pp. 6–31.

[36] C. S. Chern, "Emulsion polymerization mechanisms and kinetics," *Prog. Polym. Sci.*, vol. 31, no. 5, pp. 443–486, 2006.

[37] G. Odian, "Emulsion Polymerization," in *Principles of Polymerization*, 4th ed., Hoboken, NJ, USA: John Wiley & Sons,

Inc., 2004, pp. 350–371.

[38] H. Kawaguchi, "On going to a new era of microgel exhibiting volume phase transition," *Gels*, vol. 6, no. 3, pp. 1–24, Sep. 2020.

[39] M. Martinez-Moro, J. Jenczyk, J. M. Giussi, S. Jurga, and S. E. Moya, "Kinetics of the thermal response of poly(N-isopropylacrylamide co methacrylic acid) hydrogel microparticles under different environmental stimuli: A time-lapse NMR study," *J. Colloid Interface Sci.*, vol. 580, pp. 439–448, Nov. 2020.

[40] M. Brugnoni, F. Fink, A. Scotti, and W. Richtering, "Synthesis and structure of temperature-sensitive nanocapsules," *Colloid Polym. Sci.*, vol. 298, no. 9, pp. 1179–1185, Sep. 2020.

[41] M. Wei *et al.*, "Stimuli-responsive microgels for controlled deposition of gold nanoparticles on surfaces," *Nanoscale Adv.*, vol. 2, no. 11, pp. 5242–5253, Nov. 2020.

[42] J. Wang, Y. Liu, R. Chen, Z. Zhang, G. Chen, and H. Chen, "Ultralow self-cross-linked poly(N-isopropylacrylamide) microgels prepared by solvent exchange," *Langmuir*, vol. 35, no. 43, pp. 13991–13998, Oct. 2019.

[43] C. Su, J. Liu, Z. Yang, L. Jiang, X. Liu, and W. Shao, "UV-mediated synthesis of carboxymethyl cellulose/poly-N-isopropylacrylamide composite hydrogels with triple stimuli-responsive swelling performances," *Int. J. Biol. Macromol.*, vol.

161, pp. 1140–1148, Oct. 2020.

[44] J. Khan, M. Siddiq, B. Akram, and M. A. Ashraf, "In-situ synthesis of CuO nanoparticles in P(NIPAM-co-AAA) microgel, structural characterization, catalytic and biological applications," *Arab. J. Chem.*, vol. 11, no. 6, pp. 897–909, 2018.

[45] J. Zhang *et al.*, "Preparation and anti-mold properties of nano-ZnO/poly(N-isopropylacrylamide) composite hydrogels," *Molecules*, vol. 25, no. 18, p. 4135, Sep. 2020.

[46] Q. Dong, C. Luo, H. Hu, Q. Zhang, and S. Fan, "Synthesis and photo-controllable thermosensitivity of poly(N-isopropylacrylamide) terminated with dimethylaminochalcone unit," *J. Polym. Res.*, vol. 24, no. 12, pp. 1–8, Nov. 2017.

[47] M. Fedorczyk, A. Krzywicka, P. Cieciórski, J. Romański, and E. Megiel, "A novel strategy for the synthesis of amphiphilic and thermoresponsive Poly(N-isopropylacrylamide)- b-polystyrene block copolymers via ATRP," *Polymers (Basel).*, vol. 11, no. 9, p. 1484, Sep. 2019.

[48] J. Wei *et al.*, "Facile synthesis of thermo-responsive nanogels less than 50 nm in diameter via soap- and heat-free precipitation polymerization," *J. Mater. Sci.*, vol. 53, no. 17, pp. 12056–12064, 2018.

[49] Z. Wei, W. Zhao, Y. Wang, X. Wang, S. Long, and J. Yang, "Novel PNIPAm-based electrospun nanofibres used directly as a

drug carrier for 'on-off' switchable drug release," *Colloids Surfaces B Biointerfaces*, vol. 182, p. 110347, Oct. 2019.

[50] Y. L. Han, H. R. Kim, H. K. Kim, and J. W. Park, "Thermosensitive poly(N-isopropylacrylamide)-grafted magnetic-cored dendrimers for benzene uptake," *Chemosphere*, vol. 307, p. 135988, Nov. 2022.

[51] C. Frantz, K. M. Stewart, and V. M. Weaver, "The extracellular matrix at a glance," *J. Cell Sci.*, vol. 123, no. 24, pp. 4195–4200, 2010.

[52] T. Rozario and D. W. DeSimone, "The extracellular matrix in development and morphogenesis: A dynamic view," *Dev. Biol.*, vol. 341, no. 1, pp. 126–140, 2010.

[53] J. Myllyharju and K. I. Kivirikko, "Collagens, modifying enzymes and their mutations in humans, flies and worms," *Trends Genet.*, vol. 20, no. 1, pp. 33–43, 2004.

[54] L. D. Muiznieks and F. W. Keeley, "Molecular assembly and mechanical properties of the extracellular matrix: A fibrous protein perspective," *Biochim. Biophys. Acta - Mol. Basis Dis.*, vol. 1832, no. 7, pp. 866–875, 2013.

[55] B. Brodsky and A. V Persikov, "Molecular structure of the collagen triple helix," in *Fibrous Proteins: Coiled-Coils, Collagen and Elastomers*, vol. 70, Academic Press, 2005, pp. 301–339.

[56] T. Koide, "Designed triple-helical peptides as tools for collagen biochemistry and matrix engineering," *Philos. Trans. R. Soc. B*

Biol. Sci., vol. 362, no. 1484, pp. 1281–1291, 2007.

[57] B. Jordi, M. Eaton, B. Brodsky, and H. M. Berman, "Crystal and molecular structure of a collagen-like peptide at 1.9 A resolution," *Science.*, vol. 266, no. 5182, pp. 75–81, 1994.

[58] M. D. Shoulders and R. T. Raines, "Collagen structure and stability," *Annu. Rev. Biochem.*, vol. 78, no. 1, pp. 929–958, 2009.

[59] S. Gorgieva and V. Kokol, "Collagen- vs. gelatine-based biomaterials and their biocompatibility: review and perspectives," *Biomater. Appl. Nanomedicine*, vol. 2, pp. 17–52, 2011.

[60] R. Parenteau-Bareil, R. Gauvin, and F. Berthod, "Collagen-based biomaterials for tissue engineering applications," *Materials (Basel).*, vol. 3, no. 3, pp. 1863–1887, 2010.

[61] M. Yamauchi, Y. Taga, S. Hattori, M. Shiiba, and M. Terajima, "Analysis of collagen and elastin cross-links," in *Methods in Extracellular Matrix Biology*, vol. 143, R. P. B. T.-M. in C. B. Mecham, Ed. Academic Press, 2018, pp. 115–132.

[62] A. Sorushanova *et al.*, "The collagen suprafamily: From biosynthesis to advanced biomaterial development," *Adv. Mater.*, vol. 31, no. 1, p. 1801651, Jan. 2019.

[63] H. Lodish, A. Berk, S. L. Zipursky, P. Matsudaira, D. Baltimore, and J. Darnell, "Collagen: The fibrous proteins of the matrix," in *Molecular Cell Biology*, 4th ed., New York: W. H. Freeman, 2000.

[64] S. Bancelin *et al.*, "Determination of collagen fibril size via absolute measurements of second-harmonic generation signals," *Nat. Commun.*, vol. 5, no. 1, pp. 1–8, 2014.

[65] B. P. Chan and K. W. Leong, "Scaffolding in tissue engineering: general approaches and tissue-specific considerations," *Eur. Spine J.*, vol. 17, no. Suppl 4, pp. 467–479, 2008.

[66] P.- Berillis, "Marine collagen: Extraction and applications," in *Research Trends in Biochemistry, Molecular Biology and Microbiology*, S. Madhukar, Ed. SM Group, 2015, pp. 1–13.

[67] W. Pustlauk, B. Paul, S. Brueggemeier, M. Gelinsky, and A. Bernhardt, "Modulation of chondrogenic differentiation of human mesenchymal stem cells in jellyfish collagen scaffolds by cell density and culture medium," *J. Tissue Eng. Regen. Med.*, vol. 11, no. 6, pp. 1710–1722, Jun. 2017.

[68] X. Cheng, Z. Shao, C. Li, L. Yu, M. A. Raja, and C. Liu, "Isolation, characterization and evaluation of collagen from jellyfish Rhopilema esculentum Kishinouye for use in hemostatic applications," *PLoS One*, vol. 12, no. 1, p. e0169731, Jan. 2017.

[69] F. F. Felician *et al.*, "The wound healing potential of collagen peptides derived from the jellyfish Rhopilema esculentum," *Chinese J. Traumatol.*, vol. 22, no. 1, pp. 12–20, Feb. 2019.

[70] Z. Rastian *et al.*, "Type I collagen from jellyfish Catostylus mosaicus for biomaterial applications," *ACS Biomater. Sci. Eng.*, vol. 4, no. 6, pp. 2115–2125, Jun. 2018.

[71] S. Addad, J.-Y. Exposito, C. Faye, S. Ricard-Blum, and C. Lethias, "Isolation, characterization and biological evaluation of jellyfish collagen for use in biomedical applications," *Mar. Drugs 2011, Vol. 9, Pages 967-983*, vol. 9, no. 6, pp. 967–983, Jun. 2011.

[72] K. L. Goh and D. F. Holmes, "Collagenous extracellular matrix biomaterials for tissue engineering: Lessons from the common sea urchin tissue," *Int. J. Mol. Sci. 2017, Vol. 18, Page 901*, vol. 18, no. 5, pp. 901–948, Apr. 2017.

[73] C. Ferrario *et al.*, "From food waste to innovative biomaterial: Sea urchin-derived collagen for applications in skin regenerative medicine," *Mar. Drugs 2020, Vol. 18, Page 414*, vol. 18, no. 8, p. 414, Aug. 2020.

[74] L. Delphi, H. Sepehri, E. Motevaseli, and M. R. Khorramizadeh, "Collagen extracted from persian gulf squid exhibits anti-cytotoxic properties on apple pectic treated cells: Assessment in an in vitro bioassay model," *Iran. J. Public Health*, vol. 45, no. 8, pp. 1054–1063, Aug. 2016.

[75] L. M. Blowes *et al.*, "Body wall structure in the starfish Asterias rubens," *J. Anat.*, vol. 231, no. 3, pp. 325–341, Sep. 2017.

[76] M. Dai, X. Liu, N. Wang, and J. Sun, "Squid type II collagen as a novel biomaterial: Isolation, characterization, immunogenicity and relieving effect on degenerative osteoarthritis via inhibiting STAT1 signaling in pro-inflammatory macrophages," *Mater. Sci.*

Eng. C, vol. 89, no. 8, pp. 283–294, Aug. 2018.

[77] S. Chen *et al.*, "Compositional and structural characteristics of pepsin-soluble type I collagen from the scales of red drum fish, Sciaenops ocellatus," *Food Hydrocoll.*, vol. 123, p. 107111, Feb. 2022.

[78] M. J. Fatemi *et al.*, "Investigating the impact of collagen-chitosan derived from Scomberomorus Guttatus and shrimp skin on second-degree burn in rats model," *Regen. Ther.*, vol. 18, pp. 12–20, Dec. 2021.

[79] B. Sanz *et al.*, "Light cross-linkable marine collagen for coaxial printing of a 3D model of neuromuscular junction formation," *Biomedicines*, vol. 9, no. 1, pp. 1–19, Dec. 2020.

[80] G. Selvakumar, I. Kuttalam, S. Mukundan, and S. Lonchin, "Valorization of toxic discarded fish skin for biomedical application," *J. Clean. Prod.*, vol. 323, p. 129147, Nov. 2021.

[81] M. I. Shaik, J. Y. Chong, and N. M. Sarbon, "Effect of ultrasound-assisted extraction on the extractability and physicochemical properties of acid and pepsin soluble collagen derived from Sharpnose stingray (Dasyatis zugei) skin," *Biocatal. Agric. Biotechnol.*, vol. 38, p. 102218, Nov. 2021.

[82] M. J. Seixas, E. Martins, R. L. Reis, and T. H. Silva, "Extraction and characterization of collagen from elasmobranch byproducts for potential biomaterial use," *Mar. Drugs 2020, Vol. 18, Page 617*, vol. 18, no. 12, p. 617, Dec. 2020.

[83] A. W. Sulaiman and N. M. Sarbon, "Characterization of acid soluble collagen (ASC) and pepsin soluble collagen (PSC) extracted from shortfin scad (decapterus macrosoma) waste," *Food Res.*, vol. 4, no. 6, pp. 2272–2280, Dec. 2020.

[84] M. Blanco, J. A. Vázquez, R. I. Pérez-Martín, and C. G. Sotelo, "Collagen extraction optimization from the skin of the small-spotted catshark (S. canicula) by response surface methodology," *Mar. Drugs*, vol. 17, no. 1, p. 40, Jan. 2019.

[85] C. G. Sotelo, M. B. Comesaña, P. R. Ariza, and R. I. Pérez-Martín, "Characterization of collagen from different discarded fish species of the west coast of the Iberian peninsula," *http://dx.doi.org/10.1080/10498850.2013.865283*, vol. 25, no. 3, pp. 388–399, Apr. 2016.

[86] R. Ahmed, A. T. Getachew, Y. J. Cho, and B. S. Chun, "Application of bacterial collagenolytic proteases for the extraction of type I collagen from the skin of bigeye tuna (Thunnus obesus)," *LWT*, vol. 89, pp. 44–51, Mar. 2018.

[87] J. Kuwahara, "Extraction of type I collagen from Tilapia scales using acetic acid and ultrafine bubbles," *Process. 2021, Vol. 9, Page 288*, vol. 9, no. 2, p. 288, Feb. 2021.

[88] Z. I. Elbialy *et al.*, "Collagen extract obtained from Nile tilapia (Oreochromis niloticus L.) skin accelerates wound healing in rat model via up regulating VEGF, bFGF, and α-SMA genes expression," *BMC Vet. Res.*, vol. 16, no. 1, p. 352, Sep. 2020.

[89] J. X. Law, L. L. Liau, A. Saim, Y. Yang, and R. Idrus, "Electrospun collagen nanofibers and their applications in skin tissue engineering," *Tissue Eng. Regen. Med.*, vol. 14, no. 6, pp. 699–718, 2017.

[90] J. Xue, T. Wu, Y. Dai, and Y. Xia, "Electrospinning and electrospun nanofibers: Methods, materials, and applications," *Chem. Rev.*, vol. 119, no. 8, pp. 5298–5415, 2019.

[91] S. Talwar, A. S. Krishnan, J. P. Hinestroza, B. Pourdeyhimi, and S. A. Khan, "Electrospun nanofibers with associative polymer-surfactant systems," *Macromolecules*, vol. 43, no. 18, pp. 7650–7656, Sep. 2010.

[92] J. Hu, X. Wang, B. Ding, J. Lin, J. Yu, and G. Sun, "One-step electro-spinning/netting technique for controllably preparing polyurethane nano-fiber/net," *Macromol. Rapid Commun.*, vol. 32, no. 21, pp. 1729–1734, Nov. 2011.

[93] A. Haider, S. Haider, and I. K. Kang, "A comprehensive review summarizing the effect of electrospinning parameters and potential applications of nanofibers in biomedical and biotechnology," *Arab. J. Chem.*, vol. 11, no. 8, pp. 1165–1188, Dec. 2018.

[94] C. J. Angammana and S. H. Jayaram, "Analysis of the effects of solution conductivity on electrospinning process and fiber morphology," *IEEE Trans. Ind. Appl.*, vol. 47, no. 3, pp. 1109–1117, May 2011.

[95] D. Rodoplu and M. Mutlu, "Effects of electrospinning setup and process parameters on nanofiber morphology intended for the modification of quartz crystal microbalance surfaces," *J. Eng. Fiber. Fabr.*, vol. 7, no. 2, pp. 118–123, Jun. 2012.

[96] V. Beachley and X. Wen, "Effect of electrospinning parameters on the nanofiber diameter and length," *Mater. Sci. Eng. C*, vol. 29, no. 3, pp. 663–668, Apr. 2009.

[97] F. Liu, R. Guo, M. Shen, S. Wang, and X. Shi, "Effect of processing variables on the morphology of electrospun poly[(lactic acid)-co-(glycolic acid)] nanofibers," *Macromol. Mater. Eng.*, vol. 294, no. 10, pp. 666–672, Oct. 2009.

[98] Y. Liu, L. Dong, J. Fan, R. Wang, and J.-Y. Yu, "Effect of applied voltage on diameter and morphology of ultrafine fibers in bubble electrospinning," *J. Appl. Polym. Sci.*, vol. 120, no. 1, pp. 592–598, Apr. 2011.

[99] M. Demir, I. Yilgor, E. Yilgor, B. E.- Polymer, and undefined 2002, "Electrospinning of polyurethane fibers," *Elsevier*, vol. 43, no. 11, pp. 3303–3309, 2002.

[100] X. Wang, B. Ding, J. Yu, and J. Yang, "Large-scale fabrication of two-dimensional spider-web-like gelatin nano-nets via electro-netting," *Colloids Surfaces B Biointerfaces*, vol. 86, no. 2, pp. 345–352, Sep. 2011.

[101] G. Z. Yang, H. P. Li, J. H. Yang, J. Wan, and D. G. Yu, "Influence of working temperature on the formation of electrospun polymer

nanofibers," *Nanoscale Res. Lett.*, vol. 12, no. 1, p. 55, Dec. 2017.

[102] J. M. Ameer, P. R. Anil Kumar, and N. Kasoju, "Strategies to tune electrospun scaffold porosity for effective cell response in tissue engineering," *J. Funct. Biomater.*, vol. 10, no. 3, Sep. 2019.

[103] J. Liu, L. Argenta, M. Morykwas, and W. D. Wagner, "Properties of single electrospun poly (diol citrate)-collagen-proteoglycan nanofibers for arterial repair and in applications requiring viscoelasticity," *J. Biomater. Appl.*, vol. 28, no. 5, pp. 729–738, 2014.

[104] A. Fiorani *et al.*, "Comparative performance of collagen nanofibers electrospun from different solvents and stabilized by different crosslinkers," *J. Mater. Sci. Mater. Med.*, vol. 25, no. 10, pp. 2313–2321, 2014.

[105] F. L. Zhou, R. H. Gong, and I. Porat, "Needle and needleless electrospinning for nanofibers," *J. Appl. Polym. Sci.*, vol. 115, no. 5, pp. 2591–2598, Mar. 2010.

[106] J. A. Matthews, G. E. Wnek, D. G. Simpson, and G. L. Bowlin, "Electrospinning of collagen nanofibers," *Biomacromolecules*, vol. 3, no. 2, pp. 232–238, 2002.

[107] D. I. Zeugolis *et al.*, "Electro-spinning of pure collagen nano-fibres - Just an expensive way to make gelatin?," *Biomaterials*, vol. 29, no. 15, pp. 2293–2305, 2008.

[108] B. Dong, O. Arnoult, M. E. Smith, and G. E. Wnek, "Electrospinning of collagen nanofiber scaffolds from benign solvents," *Macromol. Rapid Commun.*, vol. 30, no. 7, pp. 539–542, 2009.

[109] A. Elamparithi, A. M. Punnoose, and S. Kuruvilla, "Electrospun type 1 collagen matrices preserving native ultrastructure using benign binary solvent for cardiac tissue engineering," *Artif. Cells, Nanomedicine Biotechnol.*, vol. 44, no. 5, pp. 1318–1325, 2016.

[110] C. P. Barnes, C. W. Pemble IV, D. D. Brand, D. G. Simpson, and G. L. Bowlin, "Cross-linking electrospun type II collagen tissue engineering scaffolds with carbodiimide in ethanol," *Tissue Eng.*, vol. 13, no. 7, pp. 1593–1605, 2007.

[111] J. A. Matthews, G. E. Wnek, D. G. Simpson, and G. L. Bowlin, "Electrospinning of collagen nanofibers," *Biomacromolecules*, vol. 3, no. 2, pp. 232–238, Mar. 2002.

[112] J. A. Matthews, E. D. Boland, G. E. Wnek, D. G. Simpson, and G. L. Bowlin, "Electrospinning of collagen type II: A feasibility study," *J. Bioact. Compat. Polym.*, vol. 18, no. 2, pp. 125–134, 2003.

[113] K. J. Shields, M. J. Beckman, G. L. Bowlin, and J. S. Wayne, "Mechanical properties and cellular proliferation of electrospun collagen type II," in *Tissue Engineering*, 2004, vol. 10, no. 9–10, pp. 1510–1517.

[114] S. Zhong, W. E. Teo, X. Zhu, R. W. Beuerman, S. Ramakrishna, and L. Y. L. Yung, "An aligned nanofibrous collagen scaffold by electrospinning and its effects on in vitro fibroblast culture," *J. Biomed. Mater. Res. - Part A*, vol. 79, no. 3, pp. 456–463, 2006.

[115] K. S. Rho *et al.*, "Electrospinning of collagen nanofibers: Effects on the behavior of normal human keratinocytes and early-stage wound healing," *Biomaterials*, vol. 27, no. 8, pp. 1452–1461, 2006.

[116] V. Thomas, D. R. Dean, M. V. Jose, B. Mathew, S. Chowdhury, and Y. K. Vohra, "Nanostructured biocomposite scaffolds based on collagen coelectrospun with nanohydroxyapatite," *Biomacromolecules*, vol. 8, no. 2, pp. 631–637, 2007.

[117] D. Newton, R. Mahajan, C. Ayres, J. R. Bowman, G. L. Bowlin, and D. G. Simpson, "Regulation of material properties in electrospun scaffolds: Role of cross-linking and fiber tertiary structure," *Acta Biomater.*, vol. 5, no. 1, pp. 518–529, Jan. 2009.

[118] D. Phu, L. S. Wray, R. V. Warren, R. C. Haskell, and E. J. Orwin, "Effect of substrate composition and alignment on corneal cell phenotype," *Tissue Eng. - Part A*, vol. 17, no. 5–6, pp. 799–807, 2011.

[119] J.-H. Song, H.-E. Kim, and H.-W. Kim, "Electrospun fibrous web of collagen-apatite precipitated nanocomposite for bone regeneration," *J. Mater. Sci. Mater. Med.*, vol. 19, no. 8, pp.

2925–2932, 2008.

[120] Y.-R. V. Shih, C.-N. Chen, S.-W. Tsai, Y. J. Wang, and O. K. Lee, "Growth of mesenchymal stem cells on electrospun type I collagen nanofibers," *Stem Cells*, vol. 24, no. 11, pp. 2391–2397, 2006.

[121] H. M. Powell, D. M. Supp, and S. T. Boyce, "Influence of electrospun collagen on wound contraction of engineered skin substitutes," *Biomaterials*, vol. 29, no. 7, pp. 834–843, 2008.

[122] S. Torres-Giner, J. V. Gimeno-Alcañiz, M. J. Ocio, and J. M. Lagaron, "Comparative performance of electrospun collagen nanofibers cross-linked by means of different methods," *ACS Appl. Mater. Interfaces*, vol. 1, no. 1, pp. 218–223, 2009.

[123] A. Timnak *et al.*, "Fabrication of nano-structured electrospun collagen scaffold intended for nerve tissue engineering," *J. Mater. Sci. Mater. Med.*, vol. 22, no. 6, pp. 1555–1567, 2011.

[124] M. Mekhail, K. K. H. Wong, D. T. Padavan, Y. Wu, D. B. O'Gorman, and W. Wan, "Genipin-cross-linked electrospun collagen fibers," *J. Biomater. Sci. Polym. Ed.*, vol. 22, no. 17, pp. 2241–2259, 2011.

[125] M. Li, M. J. Mondrinos, M. R. Gandhi, F. K. Ko, A. S. Weiss, and P. I. Lelkes, "Electrospun protein fibers as matrices for tissue engineering," *Biomaterials*, vol. 26, no. 30, pp. 5999–6008, 2005.

[126] T. Liu, W. K. Teng, B. P. Chan, and S. Y. Chew, "Photochemical

crosslinked electrospun collagen nanofibers: Synthesis, characterization and neural stem cell interactions," *J. Biomed. Mater. Res. - Part A*, vol. 95A, no. 1, pp. 276–282, 2010.

[127] Q. Jiang, N. Reddy, S. Zhang, N. Roscioli, and Y. Yang, "Water-stable electrospun collagen fibers from a non-toxic solvent and crosslinking system," *J. Biomed. Mater. Res. - Part A*, vol. 101 A, no. 5, pp. 1237–1247, 2013.

[128] L. S. Sefcik *et al.*, "Collagen nanofibres are a biomimetic substrate for the serum-free osteogenic differentiation of human adipose stem cells," *J. Tissue Eng. Regen. Med.*, vol. 2, no. 4, pp. 210–220, 2008.

[129] J. W. Drexler and H. M. Powell, "Dehydrothermal crosslinking of electrospun collagen," *Tissue Eng. - Part C Methods*, vol. 17, no. 1, pp. 9–17, 2010.

[130] G. C. Ebersole, H. Paranjape, P. M. Anderson, and H. M. Powell, "Influence of hydration on fiber geometry in electrospun scaffolds," *Acta Biomater.*, vol. 8, no. 12, pp. 4342–4348, 2012.

[131] J. J. Willard *et al.*, "Plant-derived human collagen scaffolds for skin tissue engineering," *Tissue Eng. - Part A*, vol. 19, no. 13–14, pp. 1507–1518, 2013.

[132] D. Dems *et al.*, "Native collagen: Electrospinning of pure, cross-linker-free, self-supported membrane," *ACS Appl. Bio Mater.*, vol. 3, no. 5, pp. 2948–2957, May 2020.

[133] L. Meng, O. Arnoult, M. Smith, and G. E. Wnek,

"Electrospinning of in situ crosslinked collagen nanofibers," *J. Mater. Chem.*, vol. 22, no. 37, pp. 19412–19417, 2012.

[134] M. Kazanci, S. K. Haciosmanoglu, and G. Kamel, "Synchrotron Fourier transform infrared microspectroscopy (sFTIRM) analysis of unfolding behavior of electrospun collagen nanofibers," *Spectrochim. Acta Part A Mol. Biomol. Spectrosc.*, vol. 251, p. 119420, Apr. 2021.

[135] A. Hooshmand-Ardakani, T. Talaei-Khozani, M. Sadat-Shojai, S. Bahmanpour, and N. Zarei-Fard, "In vitro characterization of multilamellar fibers with uniaxially oriented electrospun type I collagen scaffolds," *Adv. Mater. Sci. Eng.*, vol. 2020, p. 4084317, 2020.

[136] B. N. Blackstone, M. M. Malara, M. E. Baumann, K. L. McFarland, D. M. Supp, and H. M. Powell, "Fractional CO2 laser micropatterning of cell-seeded electrospun collagen scaffolds enables rete ridge formation in 3D engineered skin," *Acta Biomater.*, vol. 102, pp. 287–297, Jan. 2020.

[137] C. Bi *et al.*, "Effect of extraction methods on the preparation of electrospun/electrosprayed microstructures of tilapia skin collagen," *J. Biosci. Bioeng.*, vol. 128, no. 2, pp. 234–240, Aug. 2019.

[138] F. A. Alexander, L. Johnson, K. Williams, and K. Packer, "A parameter study for 3D-printing organized nanofibrous collagen scaffolds using direct-write electrospinning," *Materials (Basel).*,

vol. 12, no. 24, p. 4131, Dec. 2019.

[139] D. A. Castilla-Casadiego *et al.*, "Engineering of a stable collagen nanofibrous scaffold with tunable fiber diameter, alignment, and mechanical properties," *Macromol. Mater. Eng.*, vol. 301, no. 9, pp. 1064–1075, Sep. 2016.

[140] Y. Zhou, H. Yao, J. Wang, D. Wang, Q. Liu, and Z. Li, "Greener synthesis of electrospun collagen/ hydroxyapatite composite fibers with an excellent microstructure for bone tissue engineering," *Int. J. Nanomedicine*, vol. 10, pp. 3203–3215, Apr. 2015.

[141] H. J. Lai *et al.*, "Tailored design of electrospun composite nanofibers with staged release of multiple angiogenic growth factors for chronic wound healing," *Acta Biomater.*, vol. 10, no. 10, pp. 4156–4166, 2014.

[142] H. Y. Lin, Y. J. Kuo, S. H. Chang, and T. S. Ni, "Characterization of electrospun nanofiber matrices made of collagen blends as potential skin substitutes," *Biomed. Mater.*, vol. 8, no. 2, p. 025009, 2013.

[143] A. Orendain, J. Carrasco, E. T. Enikov, and G. Peyman, "Evaluation of electro-spun tubular scaffolds to create an anastomosis using the cam assay," in *ASME International Mechanical Engineering Congress and Exposition, Proceedings (IMECE)*, 2013, vol. 3 B.

[144] J. Bürck *et al.*, "Resemblance of electrospun collagen

nanofibers to their native structure," *Langmuir*, vol. 29, no. 5, pp. 1562–1572, 2013.

[145] K. Hofman, N. Tucker, J. Stanger, M. Staiger, S. Marshall, and B. Hall, "Effects of the molecular format of collagen on characteristics of electrospun fibres," *J. Mater. Sci.*, vol. 47, no. 3, pp. 1148–1155, 2012.

[146] J. Lin, C. Li, Y. Zhao, J. Hu, and L. M. Zhang, "Co-electrospun nanofibrous membranes of collagen and zein for wound healing," *ACS Appl. Mater. Interfaces*, vol. 4, no. 2, pp. 1050–1057, 2012.

[147] M. Iafisco, I. Foltran, S. Sabbatini, G. Tosi, and N. Roveri, "Electrospun nanostructured fibers of collagen-biomimetic apatite on titanium alloy," *Bioinorg. Chem. Appl.*, vol. 2012, 2012.

[148] V. Y. Chakrapani, A. Gnanamani, V. R. Giridev, M. Madhusoothanan, and G. Sekaran, "Electrospinning of type I collagen and PCL nanofibers using acetic acid," *J. Appl. Polym. Sci.*, vol. 125, no. 4, pp. 3221–3227, 2012.

[149] I. Foltran, E. Foresti, B. Parma, P. Sabatino, and N. Roveri, "Novel biologically inspired collagen nanofibers reconstituted by electrospinning method," in *Macromolecular Symposia*, 2008, vol. 269, no. 1, pp. 111–118.

[150] B. Singh, N. Shukla, J. Kim, K. Kim, and M. H. Park, "Stimuli-responsive nanofibers containing gold nanorods for on-demand

drug delivery platforms," *Pharmaceutics*, vol. 13, no. 8, p. 1319, Aug. 2021.

[151] H. N. E. Yong, K. Y. Tshai, and S. S. Lim, "Aqueous stability of cross-linked thermal responsive tissue engineering scaffold produced by electrospinning technique," *Key Eng. Mater.*, vol. 897, pp. 39–44, Aug. 2021.

[152] T. Y. Chen, C. M. Su, C. K. Huang, J. H. Hsieh, and T. R. Ger, "Study of poly (N-isopropyl acrylamide) electrospinning magnetic fiber as a cell attach/detach substrate," *AIP Adv.*, vol. 9, no. 3, Mar. 2019.

[153] N. Thakur, A. S. Ranganath, K. Agarwal, and A. Baji, "Electrospun bead-on-string hierarchical fibers for fog harvesting application," *Macromol. Mater. Eng.*, vol. 302, no. 7, Jul. 2017.

[154] C. L. Zhang *et al.*, "Highly stimuli-responsive Au nanorods/poly(N-isopropylacrylamide) (PNIPAM) composite hydrogel for smart switch," *ACS Appl. Mater. Interfaces*, vol. 9, no. 29, pp. 24857–24863, Jul. 2017.

[155] E. Schoolaert *et al.*, "Waterborne electrospinning of poly(N-isopropylacrylamide) by control of environmental parameters," *ACS Appl. Mater. Interfaces*, vol. 9, no. 28, pp. 24100–24110, Jul. 2017.

[156] Y. Lv *et al.*, "Core-sheath nanofibers as drug delivery system for thermoresponsive controlled release," *J. Pharm. Sci.*, vol.

106, no. 5, pp. 1258–1265, May 2017.

[157] C. Wang, T. Hashimoto, and Y. Wang, "Extension rate and bending instability of electrospinning jets: The role of the electric field," *Macromolecules*, vol. 54, no. 15, pp. 7193–7209, Aug. 2021.

[158] Y. Wang and C. Wang, "Extension rate and bending behavior of electrospinning jet: The role of solution conductivity," *Polymer (Guildf).*, vol. 222, Apr. 2021.

[159] J. Ahmed, R. K. Matharu, T. Shams, U. E. Illangakoon, and M. Edirisinghe, "A comparison of electric-field-driven and pressure-driven fiber generation methods for drug delivery," *Macromol. Mater. Eng.*, vol. 303, no. 5, May 2018.

[160] C. Wang, Y. Wang, and T. Hashimoto, "Impact of entanglement density on solution electrospinning: A phenomenological model for fiber diameter," *Macromolecules*, vol. 49, no. 20, pp. 7985–7996, Oct. 2016.

[161] H. Okuzaki, K. Kobayashi, and H. Yan, "Non-woven fabric of poly(N-isopropylacrylamide) nanofibers fabricated by electrospinning," *Synth. Met.*, vol. 159, pp. 2273–2276, 2009.

[162] X. Yang, Y. Li, W. He, Q. Huang, R. Zhang, and Q. Feng, "Hydroxyapatite/collagen coating on PLGA electrospun fibers for osteogenic differentiation of bone marrow mesenchymal stem cells," *J. Biomed. Mater. Res. - Part A*, vol. 106, no. 11, pp. 2863–2870, Nov. 2018.

[163] S. Tanha *et al.*, "G-CSF loaded nanofiber/nanoparticle composite coated with collagen promotes wound healing in vivo," *J. Biomed. Mater. Res. - Part A*, vol. 105, no. 10, pp. 2830–2842, Oct. 2017.

[164] T. Bian, K. Zhao, Q. Meng, Y. Tang, H. Jiao, and J. Luo, "The construction and performance of multi-level hierarchical hydroxyapatite (HA)/collagen composite implant based on biomimetic bone Haversian motif," *Mater. Des.*, vol. 162, pp. 60–69, Jan. 2019.

[165] G. Janani, M. M. Pillai, R. Selvakumar, A. Bhattacharyya, and C. Sabarinath, "An in vitro 3D model using collagen coated gelatin nanofibers for studying breast cancer metastasis," *Biofabrication*, vol. 9, no. 1, p. 015016, Mar. 2017.

[166] M. Bacakova *et al.*, "Protein nanocoatings on synthetic polymeric nanofibrous membranes designed as carriers for skin cells," *Int. J. Nanomedicine*, vol. 12, pp. 1143–1160, 2017.

[167] G. Wu, X. Ma, Y. Wang, L. Fan, Y. Wang, and H. Deng, "Glucosamine/collagen assembled biomimetic nanofibrous mats via LBL deposition for cartilage engineering," *Appl. Surf. Sci.*, vol. 540, p. 148335, Feb. 2021.

[168] Y. Qian, X. Zhou, F. Zhang, T. G. H. Diekwisch, X. Luan, and J. Yang, "Triple PLGA/PCL Scaffold Modification including Silver Impregnation, Collagen Coating, and Electrospinning Significantly Improve Biocompatibility, Antimicrobial, and

Osteogenic Properties for Orofacial Tissue Regeneration," *ACS Appl. Mater. Interfaces*, vol. 11, no. 41, pp. 37381–37396, Oct. 2019.

[169] K. Jansen *et al.*, "Fabrication of kidney proximal tubule grafts using biofunctionalized electrospun polymer scaffolds," *Macromol. Biosci.*, vol. 19, no. 2, p. 1800412, Feb. 2019.

[170] G. Ramanathan, T. Muthukumar, and U. Tirichurapalli Sivagnanam, "In vivo efficiency of the collagen coated nanofibrous scaffold and their effect on growth factors and pro-inflammatory cytokines in wound healing," *Eur. J. Pharmacol.*, vol. 814, pp. 45–55, Nov. 2017.

[171] N. K. Zahari, R. B. H. Idrus, and S. R. Chowdhury, "Laminin-coated poly(Methyl methacrylate) (PMMA) nanofiber scaffold facilitates the enrichment of skeletal muscle myoblast population," *Int. J. Mol. Sci.*, vol. 18, no. 11, p. 2242, Oct. 2017.

[172] M. Hajikhani, Z. Emam-Djomeh, and G. Askari, "Fabrication and characterization of mucoadhesive bioplastic patch via coaxial polylactic acid (PLA) based electrospun nanofibers with antimicrobial and wound healing application," *Int. J. Biol. Macromol.*, vol. 172, pp. 143–153, Mar. 2021.

[173] X. Zhou *et al.*, "Ca ions chelation, collagen I incorporation and 3D bionic PLGA/PCL electrospun architecture to enhance osteogenic differentiation," *Mater. Des.*, vol. 198, p. 109300, Jan. 2021.

[174] H. Yuan *et al.*, "Collagen and chondroitin sulfate functionalized bioinspired fibers for tendon tissue engineering application," *Int. J. Biol. Macromol.*, vol. 170, pp. 248–260, Feb. 2021.

[175] M. Zarei, A. Samimi, M. Khorram, M. M. Abdi, and S. I. Golestaneh, "Fabrication and characterization of conductive polypyrrole/chitosan/collagen electrospun nanofiber scaffold for tissue engineering application," *Int. J. Biol. Macromol.*, vol. 168, pp. 175–186, Jan. 2021.

[176] L. Ma *et al.*, "Berberine-releasing electrospun scaffold induces osteogenic differentiation of DPSCs and accelerates bone repair," *Sci. Rep.*, vol. 11, no. 1, p. 1027, Dec. 2021.

[177] R. Wang, P. Thayer, A. Goldstein, and W. D. Wagner, "Interaction of material stiffness and negative pressure to enhance differentiation of bone marrow-derived stem cells and osteoblast proliferation," *J. Tissue Eng. Regen. Med.*, vol. 14, no. 2, pp. 295–305, Feb. 2020.

[178] S. Cesur *et al.*, "Production and characterization of elastomeric cardiac tissue-like patches for Myocardial Tissue Engineering," *Polym. Test.*, vol. 90, p. 106613, Oct. 2020.

[179] S. Cong, Y. Sun, J. Lin, S. Liu, and J. Chen, "A synthetic graft with multilayered co-electrospinning nanoscaffolds for bridging massive rotator cuff tear in a rat model," *Am. J. Sports Med.*, vol. 48, no. 8, pp. 1826–1836, Jul. 2020.

[180] S. Guo *et al.*, "Enhanced effects of electrospun collagen-

chitosan nanofiber membranes on guided bone regeneration," *J. Biomater. Sci. Polym. Ed.*, vol. 31, no. 2, pp. 155–168, Jan. 2020.

[181] Q. Hu, C. Wu, and H. Zhang, "Preparation and optimization of a biomimetic triple-layered vascular scaffold based on coaxial electrospinning," *Appl. Biochem. Biotechnol.*, vol. 190, no. 3, pp. 1106–1123, Mar. 2020.

[182] D. Miele *et al.*, "Collagen/PCL nanofibers electrospun in green solvent by DOE assisted process. An insight into collagen contribution," *Materials (Basel).*, vol. 13, no. 21, pp. 1–24, Nov. 2020.

[183] Z. Sartawi, C. Waeber, E. Schipani, and K. B. Ryan, "Development of electrospun polymer scaffolds for the localized and controlled delivery of siponimod for the management of critical bone defects," *Int. J. Pharm.*, vol. 590, p. 119956, Nov. 2020.

[184] K. F. Schüttler *et al.*, "Direct incorporation of mesenchymal stem cells into a Nanofiber scaffold – in vitro and in vivo analysis," *Sci. Rep.*, vol. 10, no. 1, p. 9557, Dec. 2020.

[185] H. Zhao *et al.*, "Electrospun icariin-loaded core-shell collagen, polycaprolactone, hydroxyapatite composite scaffolds for the repair of rabbit tibia bone defects," *Int. J. Nanomedicine*, vol. 15, pp. 3039–3056, 2020.

[186] H. A. Rather, J. F. Varghese, B. dhimmar, U. C. S. Yadav, and

R. Vasita, "Polycaprolactone-collagen nanofibers loaded with dexamethasone and simvastatin as an osteoinductive and immunocompatible scaffold for bone regeneration applications," *Biomater. Biosyst.*, vol. 8, p. 100064, Dec. 2022.

[187] K. Qin *et al.*, "Hyaluronan promotes the regeneration of vascular smooth muscle with potent contractile function in rapidly biodegradable vascular grafts," *Biomaterials*, vol. 257, p. 120226, Oct. 2020.

[188] E. Türker, Ü. H. Yildiz, and A. Arslan Yildiz, "Biomimetic hybrid scaffold consisting of co-electrospun collagen and PLLCL for 3D cell culture," *Int. J. Biol. Macromol.*, vol. 139, pp. 1054–1062, Oct. 2019.

[189] T. Wu *et al.*, "A multi-layered vascular scaffold with symmetrical structure by bi-directional gradient electrospinning," *Colloids Surfaces B Biointerfaces*, vol. 133, pp. 179–188, Sep. 2015.

[190] Z. Arabpour *et al.*, "Design and characterization of biodegradable multi layered electrospun nanofibers for corneal tissue engineering applications," *J. Biomed. Mater. Res. - Part A*, vol. 107, no. 10, pp. 2340–2349, 2019.

[191] H. K. Park, W. Joo, B. K. Gu, M. Y. Ha, S. J. You, and H. J. Chun, "Collagen/poly(D,L-lactic-co-glycolic acid) composite fibrous scaffold prepared by independent nozzle control multi-electrospinning apparatus for dura repair," *J. Ind. Eng. Chem.*,

vol. 66, pp. 430–437, Oct. 2018.

[192] D. Radakovic *et al.*, "A multilayered electrospun graft as vascular access for hemodialysis," *PLoS One*, vol. 12, no. 10, p. e0185916, Oct. 2017.

[193] K. Ghosal, A. Manakhov, L. Zajíčková, and S. Thomas, "Structural and surface compatibility study of modified electrospun poly(ε-caprolactone) (PCL) composites for skin tissue engineering," *AAPS PharmSciTech*, vol. 18, no. 1, pp. 72–81, 2017.

[194] F. Gonçalves *et al.*, "Hybrid Membranes of PLLA/Collagen for Bone Tissue Engineering: A Comparative Study of = Scaffold Production Techniques for Optimal Mechanical Properties and Osteoinduction Ability," *Materials (Basel).*, vol. 8, no. 2, pp. 408–423, 2015.

[195] Z. H. Farooqi, H. U. Khan, S. M. Shah, and M. Siddiq, "Stability of poly(N-isopropylacrylamide-co-acrylic acid) polymer microgels under various conditions of temperature, pH and salt concentration," *Arab. J. Chem.*, vol. 10, no. 3, pp. 329–335, Mar. 2017.

[196] F. Zhang, A. Wang, Z. Li, S. He, and L. Shao, "Preparation and characterisation of collagen from freshwater fish scales," *Food Nutr. Sci.*, vol. 02, no. 08, pp. 818–823, 2011.

[197] N. Ribeiro, S. R. Sousa, C. A. Van Blitterswijk, L. Moroni, and F. J. Monteiro, "A biocomposite of collagen nanofibers and

nanohydroxyapatite for bone regeneration," *Biofabrication*, vol. 6, no. 3, p. 035015, 2014.

[198] S. Sbeih, P. S. Mohanty, M. R. Morrow, and A. Yethiraj, "Structural parameters of soft PNIPAM microgel particles as a function of crosslink density," *J. Colloid Interface Sci.*, vol. 552, pp. 781–793, Sep. 2019.

[199] R. S. Hebbar, A. M. Isloor, and A. F. Ismail, "Contact Angle Measurements," in *Membrane Characterization*, Elsevier Inc., 2017, pp. 219–255.

[200] B. Sun, Y. Lin, and P. Wu, "Structure analysis of poly(N-isopropylacrylamide) using near- infrared spectroscopy and generalized two-dimensional correlation infrared spectroscopy," *Appl. Spectrosc.*, vol. 61, no. 7, pp. 765–771, 2007.

[201] M. Kurečič, M. Sfiligoj-Smole, and K. Stana-Kleinschek, "UV polymerization of poly (N-isopropylacrylamide) hydrogel," *Mater. Tehnol.*, vol. 46, no. 1, pp. 87–91, 2011.

[202] S. R. Shunmukham, V. L. Hallenbeck, and R. L. Guile, "Emulsion polymerization of styrene. II. Effect of agitation," *J. Polym. Sci.*, vol. 6, no. 6, pp. 691–698, 2003.

[203] C. P. Evans, P. M. Hay, L. Marker, R. W. Murray, and O. J. Sweeting, "Mechanism of Emulsion Polymerization of Vinylidene Chloride. III. Effects of Stirring Rate on Kinetics," *J. Appl. Polym. Sci.*, vol. 5, no. 13, pp. 39–47, Jan. 1961.

[204] H. B. Yamak, "Emulsion Polymerization: Effects of

Polymerization Variables on the Properties of Vinyl Acetate Based Emulsion Polymers," in *Polymer Science*, F. Ylmaz, Ed. InTech, 2013, pp. 40–41.

[205] S. Omi, Y. Shiraishi, H. Sato, and H. Kubota, "'The Effect of Agitation on the Rate of Emulsion Polymerization of Styrene,'" *J. Chem. Eng. Japan*, vol. 2, no. 1, pp. 64–70, 1969.

[206] I. A. Maxwell, B. R. Morrison, D. H. Napper, and R. G. Gilbert, "Entry of Free Radicals into Latex Particles in Emulsion Polymerization," *Macromolecules*, vol. 24, no. 7, pp. 1629–1640, Apr. 1991.

[207] Malvern Instruments, "Molecular weight measurements with the zetasizer nano system," in *Malvern Instruments*, 2011, pp. 1–6.

[208] N. Raval, R. Maheshwari, D. Kalyane, S. R. Youngren-Ortiz, M. B. Chougule, and R. K. Tekade, "Importance of physicochemical characterization of nanoparticles in pharmaceutical product development," in *Basic Fundamentals of Drug Delivery*, Elsevier, 2018, pp. 369–400.

[209] C. S. Chern, "Emulsion Polymerization Mechanisms and Kinetics," *Prog. Polym. Sci.*, vol. 31, no. 5, pp. 443–486, 2006.

[210] K. Tauer, H. Hernandez, S. Kozempel, O. Lazareva, and P. Nazaran, "Towards a Consistent Mechanism of Emulsion Polymerization—New Experimental Details," *Colloid Polym. Sci.*, vol. 286, no. 5, pp. 499–515, May 2008.

[211] H. G. Schild, "Poly(N-isopropylacrylamide): Experiment, Theory and Application," *Prog. Polym. Sci.*, vol. 17, no. 2, pp. 163–249, 1992.

[212] C. A. Ribeiro, M. V. S. Martins, A. H. Bressiani, J. C. Bressiani, M. E. Leyva, and A. A. A. de Queiroz, "Electrochemical Preparation and Characterization of PNIPAM-HAp Scaffolds for Bone Tissue Engineering," *Mater. Sci. Eng. C Mater. Biol. Appl.*, vol. 81, pp. 156–166, 2017.

[213] R. Bottom, "Thermogravimetric Analysis," in *Principles and Applications of Thermal Analysis*, P. Gabbott, Ed. Blackwell Publishing Ltd., 2008, p. 90.

[214] A. K. Tucker and M. J. Stevens, "Study of the polymer length dependence of the single chain transition temperature in syndiotactic poly(n -isopropylacrylamide) oligomers in water," *Macromolecules*, vol. 45, no. 16, pp. 6697–6703, 2012.

[215] P. F. Luckham and M. A. Ukeje, "Effect of Particle Size Distribution on the Rheology of Dispersed Systems," 1999.

[216] Z. Bazrafshan and G. K. Stylios, "A novel approach to enhance the spinnability of collagen fibers by graft polymerization," *Mater. Sci. Eng. C*, vol. 94, pp. 108–116, Jan. 2019.

[217] N. Amariei, L. R. Manea, A. P. Bertea, A. Bertea, and A. Popa, "The influence of polymer solution on the properties of electrospun 3D nanostructures," in *IOP Conference Series: Materials Science and Engineering*, 2017, p. 012092.

[218] A. M. De Guzzi Plepis, G. Goissis, and D. K. Das-Gupta, "Dielectric and pyroelectric characterization of anionic and native collagen," *Polym. Eng. Sci.*, vol. 36, no. 24, pp. 2932–2938, Dec. 1996.

[219] F. Pati, B. Adhikari, and S. Dhara, "Isolation and characterization of fish scale collagen of higher thermal stability," *Bioresour. Technol.*, vol. 101, no. 10, pp. 3737–3742, 2010.

[220] R. M. T. Fernandes, R. G. Couto Neto, C. W. A. Paschoal, J. H. Rohling, and C. W. B. Bezerra, "Collagen films from swim bladders: Preparation method and properties," *Colloids Surfaces B Biointerfaces*, vol. 62, no. 1, pp. 17–21, Mar. 2008.

[221] M. Safandowska and K. Pietrucha, "Effect of fish collagen modification on its thermal and rheological properties," *Int. J. Biol. Macromol.*, vol. 53, pp. 32–37, Feb. 2013.

[222] W. Liu, Z. Tian, C. Li, and G. Li, "Thermal denaturation of fish collagen in solution: A calorimetric and kinetic analysis," *Thermochim. Acta*, vol. 581, pp. 32–40, Apr. 2014.

[223] D. Liu, L. Liang, J. M. Regenstein, and P. Zhou, "Extraction and characterisation of pepsin-solubilised collagen from fins, scales, skins, bones and swim bladders of bighead carp (Hypophthalmichthys nobilis)," *Food Chem.*, vol. 133, no. 4, pp. 1441–1448, Aug. 2012.

[224] F. Xing *et al.*, "Regulation and directing stem cell fate by tissue

engineering functional microenvironments: Scaffold physical and chemical cues," *Stem Cells Int.*, 2019.

[225] E. Kaivosoja, G. Barreto, K. Levón, S. Virtanen, M. Ainola, and Y. T. Konttinen, "Chemical and physical properties of regenerative medicine materials controlling stem cell fate," *Ann. Med.*, vol. 44, no. 7, pp. 635–650, 2012.

[226] "EP0409 - Glycidyl POSS Cage Mixture - Hybrid." [Online]. Available: https://hybridplastics.com/product/ep0409-glycidyl-poss-cage-mixture/. [Accessed: 21-Apr-2022].

[227] B. Valamehr *et al.*, "Hydrophobic surfaces for enhanced differentiation of embryonic stem cell-derived embryoid bodies," *Proc. Natl. Acad. Sci. U. S. A.*, vol. 105, no. 38, pp. 14459–14464, Sep. 2008.

[228] P. Tengvall, I. Lundström, and B. Liedberg, "Protein adsorption studies on model organic surfaces: an ellipsometric and infrared spectroscopic approach," *Biomaterials*, vol. 19, no. 4–5, pp. 407–422, Mar. 1998.

[229] A. Gessner, R. Waicz, A. Lieske, B. R. Paulke, K. Mäder, and R. H. Müller, "Nanoparticles with decreasing surface hydrophobicities: influence on plasma protein adsorption," *Int. J. Pharm.*, vol. 196, no. 2, pp. 245–249, Mar. 2000.